MODEL PREDICTIVE TORQUE CONTROL OF AN INDUCTION MOTOR ENHANCED WITH AN INTER-TURN SHORT CIRCUIT FAULT DETECTION FEATURE

A THESIS SUBMITTED TO
THE GRADUATE SCHOOL OF NATURAL AND APPLIED SCIENCES
OF
MIDDLE EAST TECHNICAL UNIVERSITY

BY

İLKER ŞAHİN

IN PARTIAL FULFILLMENT OF THE REQUIREMENTS
FOR
THE DEGREE OF DOCTOR OF PHILOSOPHY
IN
ELECTRICAL AND ELECTRONIC ENGINEERING

SEPTEMBER 2021

Approval of the thesis:

MODEL PREDICTIVE TORQUE CONTROL OF AN INDUCTION MOTOR ENHANCED WITH AN INTER-TURN SHORT CIRCUIT FAULT DETECTION FEATURE

submitted by **İLKER ŞAHİN** in partial fulfillment of the requirements for the degree of **Doctor of Philosophy** i**n Electrical and Electronic Engineering, Middle East Technical University** by,

Prof. Dr. Halil Kalıpçılar
Dean, Graduate School of **Natural and Applied Sciences.** _____

Prof. Dr. İlkay Ulusoy
Head of the Department, **Electrical and Electronic Eng.** _____

Assoc. Prof. Dr. Ozan Keysan
Supervisor, **Electrical and Electronic Eng., METU.** _____

Prof. Dr. H. Bülent Ertan
Co-Supervisor, **Mechatronics Eng., Atılım Uni.** _____

Examining Committee Members:

Assoc. Prof. Dr. Emre Özkan
Electrical and Electronic Engineering, METU. _____

Assoc. Prof. Dr. Ozan Keysan
Electrical and Electronic Engineering, METU. _____

Prof. Dr. M. Timur Aydemir
Electrical and Electronic Engineering, Kadir Has Uni. _____

Assoc. Prof. Dr. Salih Barış Öztürk
Electrical Engineering, ITU. _____

Assist. Prof. Dr. Taner Göktaş
Electrical and Electronic Engineering, Dokuz Eylul Uni. _____

Date: 09.09.2021

I hereby declare that all information in this document has been obtained and presented in accordance with academic rules and ethical conduct. I also declare that, as required by these rules and conduct, I have fully cited and referenced all material and results that are not original to this work.

Name Last name : İlker Şahin

Signature :

ABSTRACT

MODEL PREDICTIVE TORQUE CONTROL OF AN INDUCTION MOTOR ENHANCED WITH AN INTER-TURN SHORT CIRCUIT FAULT DETECTION FEATURE

Şahin, İlker
Doctor of Philosophy, Electrical and Electronic Engineering
Supervisor : Assoc. Prof. Dr. Ozan Keysan
Co-Supervisor: Prof. Dr. Bülent Ertan

September 2021, 174 pages

Model predictive control (MPC) is a popular research topic in modern power electronics and it has been applied to a large variety of power converters and electric drives. The reason behind this interest in MPC is the advantages that it offers: intuitive and flexible algorithm, fast dynamic response, ease of handling converter nonlinearities, and system constraints, to name a few. In this thesis, MPC is applied to the torque control of an induction motor (IM). Involving both the theoretical foundation, computer simulations and experimental implementation, MPC of IM has been thoroughly documented. Detailed laboratory results suggest a good motor drive performance. Further issues regarding MPC, such as weighting factor tuning, computation time, and the dynamically varied weighting factor, are also examined.

A novel algorithm that runs as an add-on to the predictive controller is developed to detect and locate inter-turn short circuit (ITSC) faults for the IM. ITSC faults are a severe fault type that needs quick identification or else it leads to the complete malfunctioning of the machine. It is observed that an effective controller inherently

tries to compensate for the fault's corrupting influence, hence covers the fault signatures. Therefore, it is vital to address any fault detection technique in conjunction with the main controller, for a closed-loop controlled system. The basic principle utilized for fault detection is to observe the controller's outputs for any unexpected unbalance. The effectiveness of the proposed fault detection algorithm is verified with laborious experimental data. The fault and the drive system's interaction is examined with various aspects, such as the fault's effect on the cost function, current prediction error, and high-frequency impedance of the machine. Additionally, a new simulation model for the IM with ITSC fault is developed, the effectiveness of which is also verified through experimental results.

Keywords: Model Predictive Control, Fault Detection, Inter-Turn Short Circuit, Motor Drive, Induction Motor.

ÖZ

ASENKRON MOTORLARIN SARGI ARASI KISA DEVRE ARIZASI TESPİT ÖZELLİĞİ İLE ZENGİNLEŞTİRİLMİŞ MODEL ÖNGÖRÜLÜ MOMENT DENETİMİ

Şahin, İlker
Doktora, Elektrik ve Elektronik Mühendisliği
Tez Yöneticisi: Assoc. Prof. Dr. Ozan Keysan
Ortak Tez Yöneticisi: Prof. Dr. Bülent Ertan

Eylül 2021, 174 sayfa

Modern güç elektroniği araştırma alanları içerisinde, model öngörülü denetim (MÖD) yöntemi önemli bir yer edinmiş ve çok sayıda güç dönüştürücüsü ve elektrikli motor sürücü uygulamalarında kullanılmıştır. Bu ilginin arkasında yatan sebepler MÖD yönteminin sunduğu esnek ve anlaşılır denetimci yapısı, üstün dinamik başarımı, dönüştürücü doğrusal olmamalığının ve sistem kısıtlarının kolayca yönetilebilmesi gibi getirilerdir. Bu tezde, MÖD yöntemi bir asenkron makinanın moment denetimine uygulanmıştır. MÖD yöntemine ilişkin, teorik temelleri, bilgisayar benzetim çalışmalarını ve deneysel uygulamayı içerecek şekilde kapsamlı bir inceleme gerçekleştirilmiştir. Elde edilen detaylı laboratuvar verileri, iyi bir motor sürücü başarımı elde edildiğini göstermektedir. MÖD yöntemine ilişkin ağırlık katsayısı ayarlama, işlem yükü, ve ağırlık katsayısının dinamik değiştirilmesi gibi konular da incelenmiştir.

MÖD yöntemine ilave bir eklenti olarak çalışan, sargı arası kısa devre (SAKD) arızalarını saptayan ve yerini tayin eden yeni bir algoritma geliştirilmiştir. SAKD arızları kısa sürede saptanması gereken, aksi takdirde makinenin tamamen

bozulmasına yol açacak ciddi bir arıza tipidir. Etkin bir kontrolcünün, oluşan arızanın sisteme olan bozucu etkilerini telafi etmeye çalıştığı, dolayısıyla arızaya ilişkin ipuçlarının kapatıldığı gözlemlenmiştir. Bu yüzden, kapalı devre denetimi sağlanan sistemler için önerilen arıza tespit algoritmalarının ana denetçi ile birlikte değerlendirilmesi elzemdir. Arıza tespiti için benimsenen temel prensip, denetimci çıktılarında herhangi bir beklenmeyen dengesizliğin saptanmasıdır. Geliştirilen yöntemin arıza tespiti konusundaki yetkinliği detaylı laboratuvar çalışmaları ile gösterilmiştir. Arıza ve sistem arasındaki, maliyet fonksiyonuna olan etki, akım tahmin hatasına olan etki, ve makinenin yüksek frekans empedansına olan etki gibi konular da incelenmiştir. Ek olarak, SAKD arızası olan bir asenkron makinenin bilgisayar benzetiminin yapılabilmesini sağlayacak yeni bir benzetim model geliştirilip, etkinliği deneysel olarak gösterilmiştir.

Anahtar Kelimeler: Model Öngörülü Kontrol, Arıza Tespit, Sargı Arası Kısa Devre, Motor Sürücü, Asenkron Makine.

Dedicated to his imperial majesty Teoman Şahin

ACKNOWLEDGMENTS

The author wishes to express his deepest gratitude to his supervisor Dr. Ozan Keysan and co-supervisor Dr. Bülent Ertan for their guidance, advice, criticism, encouragements and insight throughout the research.

The author would like to thank his defense committee members: Dr. Timur Aydemir, Dr. Emre Özkan, Dr. Salih Barış Öztürk, Dr. Taner Göktaş, and Dr. Emine Bostancı Özkan.

The author would like to express his deepest gratitude to his first teacher Mustafa Oral. This work is the result of the foundations he laid.

The friendship and collaborations of my brilliant colleagues in METU PowerLab are gratefully acknowledged. The author would also like to thank his colleagues and executives in Aselsan, for their support and friendship.

The author would like to express his deepest appreciation and love to his dear parents and his grandparents for their love, encouragement and support throughout his life.

The author would have not managed to complete the research without the endless love, support, and patience of his beloved wife Dilara Dirican Şahin. This humble work is dedicated to her and to our beloved son Teoman.

TABLE OF CONTENTS

LIST OF TABLES

TABLES

LIST OF FIGURES

FIGURES

LIST OF ABBREVIATIONS

AC: Alternating Current

ADC: Analog to Digital Converter

CCS: Code Composer Studio

CCS-MPC: Continuous Control-Set Model Predictive Control

CPE: Current Prediction Error

CPU: Central Processor Unit

DAC: Digital to Analog Converter

DC: Direct Current

DSP: Digital Signal Processor

DTC: Direct Torque Control

EMC: Electromagnetic Compatibility

EMF: Electromotive Force

EMI: Electromagnetic Interference

FCS-MPC: Finite Control-Set Model Predictive Control

FEA: Finite Element Analysis

FFT: Fast Fourier Transform

FIS: Fault Indicating Score

FOC: Field Oriented Control

GaN: Gallium Nitride

IM: Induction Machine

IPMSM: Internal Permanent Magnet Synchronous Machine

ITSC: Inter-Turn Short Circuit

MPC: Model Predictive Control

MV: Medium Voltage

PCC: Predictive Current Control

PID: Proportional-Integral-Derivative

PMSM: Permanent Magnet Synchronous Machine

PPC: Predictive Power Control

PSC: Predictive Speed Control

PTC: Predictive Torque Control

pu: per-unit

PWM: Pulse Width Modulation

rpm: revolutions per minute

SiC: Silicon Carbide

THD: Total Harmonic Distortion

VBR: Voltage Behind Reactance

VSD: Variable Speed Drive

VSI: Voltage Source Inverter

LIST OF SYMBOLS

V	Voltage
I	Current
Ψ	Electromagnetic Flux Linkage
R	Resistance
L_m	Magnetizing Inductance
L_l	Leakage Inductance
T	Torque
J	Inertia
ω	Speed
σ	Leakage Factor
τ	Time Constant
k_r	Rotor Coupling Factor
μ	Fault Ratio
p	Pole-Pair
g	Cost
λ	Weighting Factor

Subscripts:

s	Stator

r Rotor

e Electrical

m Mechanical

f Fault

Superscript:

p Predicted

CHAPTER 1

INTRODUCTION

1.1 Background and Motivation

The electric motor is the main workhorse of our modern society. It is estimated that nearly half of the total electricity production is consumed by electric motors in industrialized countries [1]. While some of the motors can be fed directly from the grid, variable speed drives (VSD) are utilized when effective and efficient motion control is needed. Replacing line-fed motors with VSD controlled ones is still a strong trend [2]. Furthermore, the electric vehicle is booming, and existing traction applications, such as ships, railways, etc., are being electrified more and more. Therefore, the value and importance of VSDs are deemed to increase.

The control algorithms invented for effective torque and speed control lie at the heart of VSDs. The most popular motor drive strategy is field-oriented control (FOC), sometimes referred to as "vector control". The indirect and direct types of FOC were invented by Hasse and Blaschke, respectively, in the early 70s [3]. Along with the increasing availability of cheap and potent microcontrollers in the 80s, FOC revolutionized motor control. In the early era of power electronics, AC motors were often considered as "fixed-speed" motors whereas variable speed applications would often require DC motors, albeit with their drawbacks. With FOC, torque and speed control of AC motors were simplified to the level of DC motors'. As an alternative motor drive strategy with its advantages and disadvantages, direct torque control (DTC) was invented in the 80s, independently by Takahashi [4], and Depenbrock [5]. Both the FOC and DTC are commercial methods (notably more for FOC) that are widely used for adjustable speed drives [6]. A family tree of modern motor drive

techniques is depicted in Fig. 1.1, which is adapted from [7] and [8]. It should be noted that there is not a formal classification procedure that decisively rules the type of any given motor drive algorithm. Furthermore, there are many novel control algorithms that are hybrid versions of different control approaches. Nonetheless, the family tree depicted in Fig. 1.1 provides an overview of sufficient detail on the existing methods of motor control. Although both the electric motors and the motor drive systems (hardware and control) design are very mature disciplines within power electronics, the research for new machine types and control algorithms to overcome complex tasks even in harsh environments with ever stringent performance figures, as effectively and efficiently as possible, still continues [9]–[11].

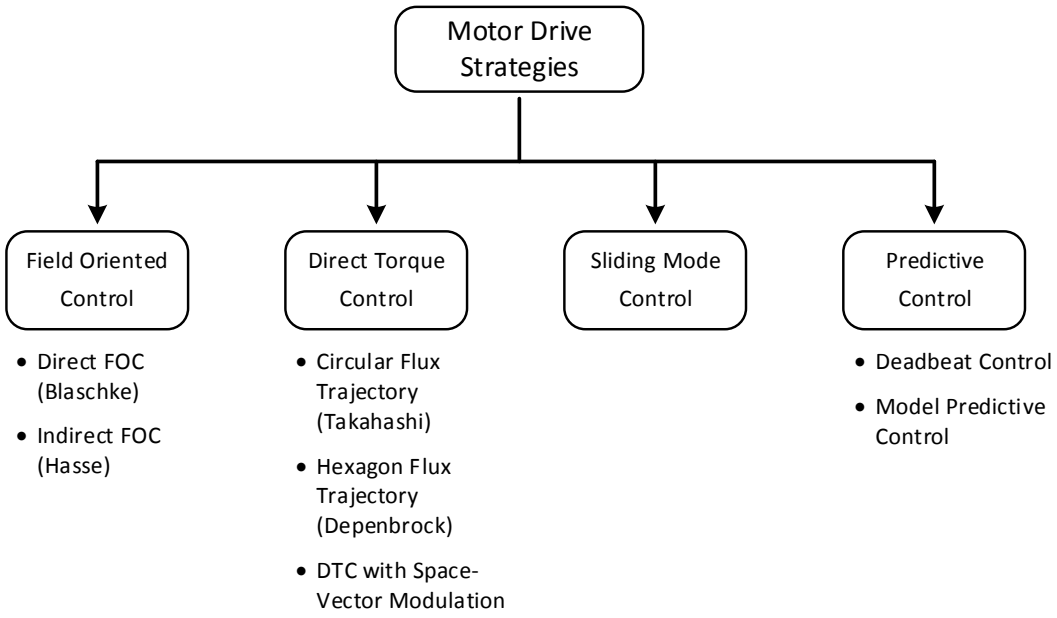

Figure 1.1. An overview of the existing motor drive techniques.

An interesting example among the modern research topics on motor drive strategies is the model predictive control (MPC). MPC has attracted significant interest from the research community especially in the last decade. Although MPC dates much earlier as a general control approach, its popularity in power electronics is relatively new. MPC has several advantages when applied to power converters and motor

drives: it is intrinsically fast and flexible, good at handling the discrete nature of power converters and system constraints and it has an intuitive flowchart that is easy to be programmed. Mathematical models for power converters and electric motors on any required detail level are widely available, therefore the model requirement of MPC is not a problem. Furthermore, a fundamental drawback of MPC, that is the increased computational burden, has been less of an issue with the microcontroller units utilized for power electronics applications providing ever more performance. Consequently, MPC has been a hot spot in modern power electronics and researchers have been evaluating MPC in many different forms for a various converter and motor types and applications.

Fault diagnosis and condition monitoring of power electronics converters and electrical machines is another fundamental field of research. Identifying any fault at the initial stage is very critical. Effective counter-measures can be taken, the fault can be stopped from evolving into a more severe state if not being completely neutralized and the downtime of the process and the repair costs of the machine or converter under consideration can be reduced. Therefore, the research on fault diagnosis and condition monitoring has always preserved its popularity and significance.

This study aims to be among the first attempts that consider fault detection along with MPC, hence unifying these two major lines of research. As the type of electric motor to be driven via MPC, the induction motor (IM) is chosen for this study, because IM is the most commonly utilized motor in industrial applications. The finite control set model predictive control (FCS-MPC) approach has been implemented for the predictive torque control of IM. Using the flexibility provided by FCS-MPC, a new fault detection algorithm for the inter-turn short circuit (ITSC) fault, which is the most common electrical fault in motors, is developed and implemented. The proposed fault detection algorithm is intuitive, non-invasive, and works as a simple extension on the standard FCS-MPC routine without imposing any significant computational burden. The performance of the proposed algorithm is verified by

detailed laboratory experiments. Contributions made through this study are listed in the following.

1.2 List of Publications Produced from the Thesis

The publications made within the scope of this dissertation are listed in Appendix A.

A prediction vector set reduction algorithm is proposed in [12] to reduce the computational burden of the MPC. The laboratory setup utilized for this study and the MPC implementation is described in [13]. An experimental tuning procedure and dynamically modified weighting factor are introduced in [14]. A simulation model for the induction machine (IM) with an inter-turn short circuit (ITSC) fault is developed in [15]. Finally, a novel algorithm that detects and locates the ITSC faults in MPC-driven IMs is proposed in [16].

1.3 The Thesis Structure

This thesis is structured in five chapters. Chapter 2 provides a review and examination of sufficient depth upon FCS-MPC. Both the theoretical background and the practical details regarding the laboratory implementation are documented. Then, the fault phenomenon in electrical machines is reviewed in Chapter 3, and the IM with an ITSC fault is modeled. Thereafter, these two major fields of research, namely; MPC and fault diagnosis are unified in Chapter 4, where a novel MPC-based fault detection scheme is presented. Finally, the thesis is concluded with Chapter 5.

Chapter 2 is the enlarged and enriched version of [12], [13], and [14]. Chapter 3 is largely based on [15] and [16]. Chapter 4 is mainly derived from [16], with several extra discussions and experimental results.

CHAPTER 2

MODEL PREDICTIVE TORQUE CONTROL OF INDUCTION MOTORS: THEORY, SIMULATION, AND IMPLEMENTATION

2.1 Introduction

This chapter is organized as follows: an overview of Model Predictive Control (MPC) with a focus on its application in power electronics is provided first. Secondly, considering the utilization of MPC as an induction machine (IM) drive, the theory of operation is explained in detail and the equations that describe the control action are provided. Then, the MPC-driven IM is simulated and results are presented. Finally, the described control approach is implemented on a laboratory setup and the experimental outcomes are documented.

2.2 Model Predictive Control: An Overview

Model predictive control (MPC) can be traced back to 1960s [17], [18]. Its main application areas have been the oil and chemical industries. With the availability of microprocessors that can solve multi-variable optimization problems, interest in MPC among the research community surged in the 1980s [17], [18]. However, the application of MPC in the power electronics area is relatively new. This is due to the fact that, compared with the process industries, the time constants of electronic systems are orders of magnitude smaller. Today, sampling and control frequencies of tens to hundreds of microseconds are typical in the control of power converters. Considering also that MPC is a more computational heavy method compared to the industry-standard PID approach, its application in power electronics requires modern, powerful microprocessors. Therefore, MPC for power electronics became

popular around the 2000s, and studies reported have been growing ever since. According to [19], the number of new publications regarding the utilization of MPC for power electronics has been roughly doubling every three years.

MPC offers many advantages when applied in power electronics. Its intuitive structure is suitable for the control of multiple variables of different nature (e.g. suppose the control of torque, flux, and current) without the requirement of nested control loops. It offers a superior dynamic response because the predictive approach can act before a significant deviation from the reference occurs and the error is accumulated, in contrast to the PI-based controllers. Its discrete structure is suitable for handling converter nonlinearities and system constraints. All of these merits explain the interest MPC has drawn from the research community and the potential it has as a new and promising method for the control of power converters and drives. As of today, MPC has been applied to almost all types of power electronics and electric drive applications [20], [21]. Considering the merits of MPC, its shift from sole academic research to industrial applications is in progress. A technological readiness assessment for MPC can be seen in [22].

For the overviews on MPC and a thorough examination of its numerous application examples, the interested reader is referred to the comprehensive review papers [20], [21], [23]–[28]. For structured learning of MPC, recently published books [8], [29]–[32], and some selected Ph.D. dissertations [33]–[36] are advised.

Although there are no strict criteria for a control strategy to be classified under MPC or not, the key feature of MPC strategies is the prediction of the controlled variables made by the utilization of the controlled system's mathematical model. Having obtained the predictions for all of the possible actions that the system can take in the feature, the best control action is decided through an optimization routine. Another key feature related to MPC is the "receding horizon policy". An MPC algorithm with a prediction horizon of "N" predicts the control variables for N time steps ahead and applies the best vector, as depicted in Fig. 2.1. The chess player calculating N moves ahead is a famous analogy for this. Regarding power electronics applications, long

prediction horizons ($N \geq 2$) are mostly reported for MV applications where the switching frequency is kept significantly low ($< 1\ kHz$) to avoid switching losses. Long horizons offer significant performance benefits compared with one step ahead prediction at the expense of an increased computational cost [19]. For low voltage applications where typical switching frequencies are in multiple kHz values, short prediction horizon ($N = 1$) applications are dominating.

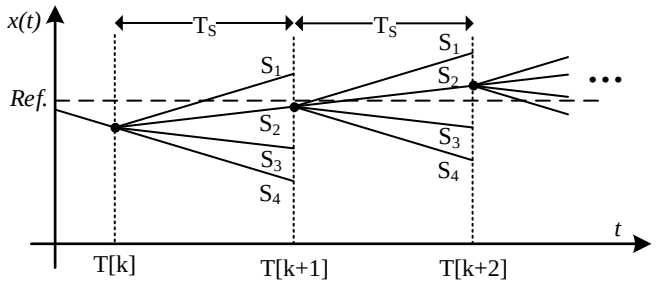

Figure 2.1. The "receding horizon policy" of MPC.

2.2.1 A Classification of MPC Methods

A classification of MPC methods as applied in power electronics, definitions of which are adapted from [21], is depicted in Fig. 2.2. The main distinction is based on the type of the optimization problem: Continuous Control Set MPC (CCS-MPC) outputs a continuous control signal, which is then realized by a PWM modulator stage. Finite Control Set MPC (FCS-MPC) however, computes an integer optimization problem and the best outcome is directly applied without any modulation. Within the CCS-MPC category, GPC is for linear and unconstrained optimization problems where EMPC is for nonlinear and constrained cases. For the FCS-MPC category, OSS-MPC considers also the instants that the switches change state, which is not employed in OSV-MPC. CCS-MPC approach is more suited for long prediction horizon applications whereas most of the FCS-MPC studies generally utilize a short prediction horizon.

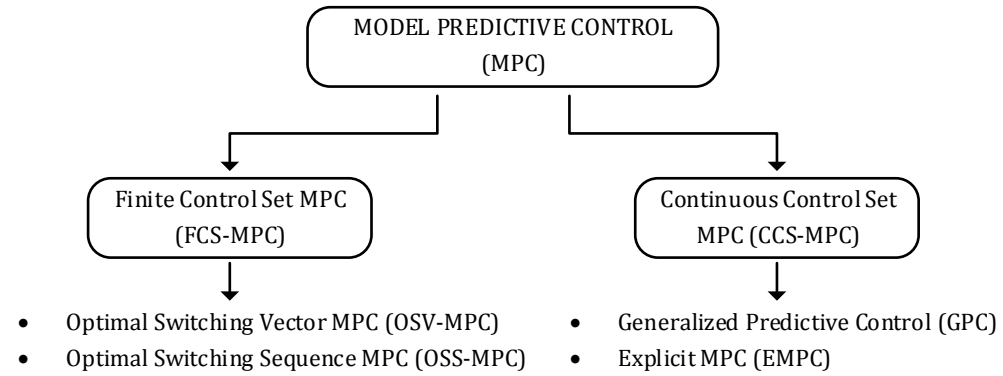

Figure 2.2. A classification of MPC as utilized in power electronics, adapted from [21].

There are two further classifications commonly reported for FCS-MPC applications in the literature, based on the distinction between the controlled variables. These are predictive torque control (PTC) and predictive current control (PCC). In PTC, the control variables are torque and flux whereas in PCC control variables are the stator currents. For more details and other types (such as predictive speed control (PSC), and predictive power control (PPC)), the interested reader is referred to [32]. In this thesis, the PTC of an induction motor (IM) will be considered.

2.2.2 Comparison with the Existing Control Techniques

The merits of MPC were previously stated as a superior dynamic response, intuitive structure that is easy to be programmed, suitability to handle converter nonlinearities and system constraints. Its two main disadvantages, on the other hand, can be stated as an increased computational burden and variable switching frequency. Due to the online optimization routine of MPC, the number of calculations is significantly higher than that of a standard motor drive method such as FOC. For the control of a 2L-VSI with a short prediction horizon, the increased computational burden is not a significant problem considering the processor capabilities of today. However, considering certain applications such as multilevel inverters (where the total number of admissible switching configurations are significantly higher compared to the 2L-

VSI) or long prediction horizon (where the total number of control actions that should be evaluated grows exponentially), the increased computational cost can be a limiting factor. The second drawback is the variable switching frequency that arises from the lack of modulator utilization. This is an undesirable feature considering practical implementations from the EMI-EMC point of view. Filtering is more convenient for a pre-determined fixed frequency. As expected, some studies address these two shortcomings. Methods for computational burden reduction are proposed in [12], [37], and variations of MPC that offer fixed switching frequency are reported in [38]–[40].

Reference [41] provides an experimental comparison between FOC, DTC, and MPC (both PTC and PCC) and acknowledges the previously stated advantages and disadvantages for MPC. Similarly, in [42], a comparison between FOC and MPC is provided, which verifies that MPC can perform similarly to FOC, possibly even better in dynamic performance. The advantages and disadvantages of predictive control schemes with respect to PWM-based control methods are examined in [43]. Compared with the DTC method, on a commercial MV-level motor drive, MPC was found to provide switching frequency reduction up to 50%, while equally respecting the torque and current boundaries [44], [45].

In order to provide a broad comparison between the mainstream control methods, i.e., FOC, DTC, and MPC, Table 2.1 is created, which is adapted from the similar comparison figures depicted in [32], [35], [41], [42]. It is important to note that Table 2.1 is intended just to give a general sense: all control methods include various hybrid versions or can be supported by additional algorithms to overcome certain disadvantages, therefore it is not convenient to categorically classify a control method best or worst. With the term MPC, the FCS-MPC utilized in PTC fashion is implied.

Table 2.1 A Broad Comparison Between FOC, DTC, and MPC.

Index	*FOC*	*DTC*	*MPC*
Coordinate Transformation	Yes	No	No
PWM Stage	Yes	No	No
Constraint Inclusion	Difficult	Difficult	Easy
Conceptual Complexity	High	Medium	Low
Parameter Sensitivity	High	Low	High
Computation Time	Low	Low	High
Torque Ripple	Low	High	Moderate
Dynamic Response	Slow	Fast	Fast
Switching Frequency	Constant	Variable	Variable

2.3 Predictive Torque Control of an Induction Motor: Theory

In this study, FCS-MPC (OSV-MPC, to be precise) is used for the speed control of an IM which is driven via a two-level voltage source inverter (2L-VSI). The applied control strategy can be classified as PTC, i.e., torque and stator flux will be the control parameters. A short prediction horizon is selected (N=1). An overview of the existing examples of MPC applications as IM drives is reported in [46].

For FCS-MPC, it is more convenient to choose the stationary reference frame approach rather than the synchronously rotating reference frame, which is more convenient for FOC modeling. Therefore, for the formulas here on, complex vector notation from a stationary reference frame is adopted. That is, all vector quantities are defined on the complex plane with a real and an imaginary part, denoted by α and β respectively, as in (2.1).

$$f_{\alpha\beta} = f_\alpha + jf_\beta \tag{2.1}$$

The transition from three-phase $a-b-c$ quantities to the complex vector representation is done via the Clarke transform, defined by (2.2), considering the transformation of phase currents from i_{abc} to $i_{\alpha\beta}$ as an example.

$$\begin{bmatrix} i_\alpha \\ i_\beta \end{bmatrix} = \frac{2}{3}\begin{bmatrix} 1 & -1/2 & -1/2 \\ 0 & 1/\sqrt{3} & -1/\sqrt{3} \end{bmatrix}\begin{bmatrix} i_a \\ i_b \\ i_c \end{bmatrix} \tag{2.2}$$

Although typically not utilized in MPC of IM, transformation to a rotating reference frame (dq) is widely applied in FOC therefore it is given in (2.3) for the sake of completeness.

$$\begin{bmatrix} i_d \\ i_q \end{bmatrix} = \begin{bmatrix} \cos(\theta) & \sin(\theta) \\ -\sin(\theta) & \cos(\theta) \end{bmatrix}\begin{bmatrix} i_\alpha \\ i_\beta \end{bmatrix} \tag{2.3}$$

Three-phase quantities passed through the Clarke transform, appear as rotating vectors on the complex plane as depicted in Fig. 2.3. Although the Clarke transform definition is provided on $i_{abc} \longrightarrow i_{\alpha\beta}$ example, other electrical variables such as stator voltage (V_s), stator and rotor fluxes (Ψ_s and Ψ_r) are also Clarke transformed complex variables.

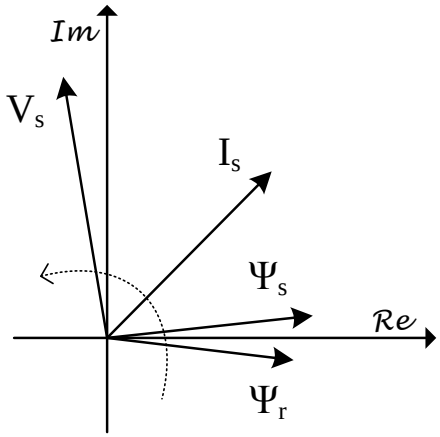

Figure 2.3. Rotating vectors on the complex plane.

As its name implies, MPC relies upon the mathematical modeling of the systems. The more accurate the model is, the higher the control performance will be.

Therefore, mathematical models of the controlled machine (IM) and the driver (2L-VSI) are to be introduced first.

2.3.1 Modeling the Induction Machine and the Inverter

2.3.1.1 The Induction Machine Model

An IM's model can be completely defined through its state-space equations, as expressed in (2.4)-(2.9). For the dynamic representation of IM, the fundamental sources, which the following equations are adapted from, are [47]–[51].

$$V_s = R_s I_s + \frac{d\Psi_s}{dt} \tag{2.4}$$

$$V_r = R_r I_r + \frac{d\Psi_r}{dt} - jw_e\Psi_r \tag{2.5}$$

$$\Psi_s = L_s I_s + L_m I_r \tag{2.6}$$

$$\Psi_r = L_m I_s + L_r I_r \tag{2.7}$$

$$\mathrm{T}_e = \frac{3}{2} p\mathcal{J}m(\Psi_s^*.I_s) \tag{2.8}$$

$$J\frac{d\omega_m}{dt} = \mathrm{T}_e - \mathrm{T}_{load} \tag{2.9}$$

In the state-space equations of (2.4)-(2.9), V, I, and Ψ stand for voltage, current, and flux, respectively. Subscripts s and r are used to indicate stator and rotor variables. T_e and T_l represent electromagnetic and load torques, w_e is the rotor angular frequency, ω_m is the mechanical speed, p is the number of pole-pairs. Rotor angular frequency is p times the mechanical speed (2.10).

$$w_e = p\,.w_m \tag{2.10}$$

Although the state-space equations are sufficient for the description of IM behavior, the visual representation of these equations in the form of an equivalent circuit is more insightful and it is depicted in Fig. 2.4.

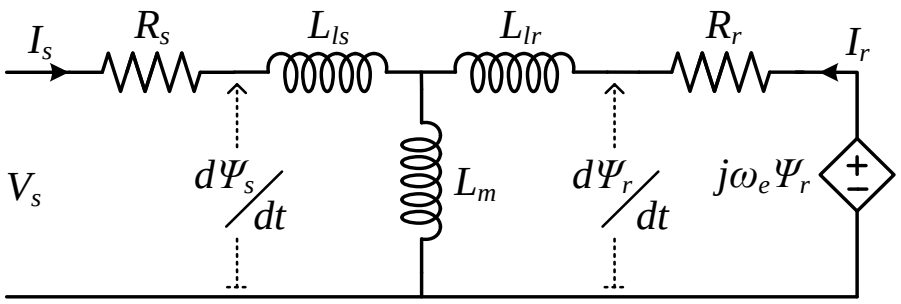

Figure 2.4. The equivalent circuit of an IM.

2.3.1.2 The Two-Level Voltage Source Inverter Model

Two-level voltage source inverters (2L-VSI) are the standard choice for DC-AC conversion for low voltage applications. A simplified structure of a 2L-VSI with idealized switches is shown in Fig. 2.5.

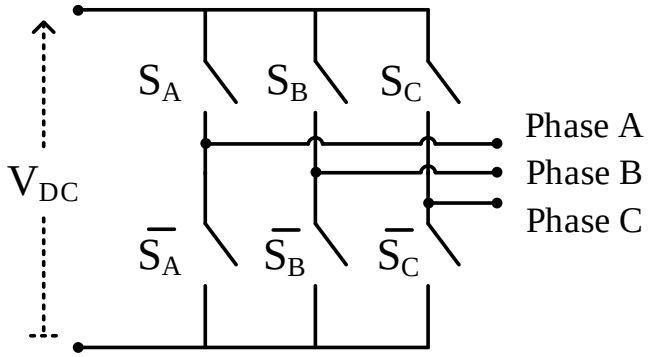

Figure 2.5. The 2L-VSI configuration, depicted with ideal switches.

Considering that the high and low side switches in a phase arm are triggered complementarily to avoid the shoot-through of the DC bus, the total number of admissible switching states that the 2L-VSI can generate becomes $2^3 = 8$. Two of these total eight switching states, $\{S_a,S_b,S_c\} = \{0,0,0\}$ and $\{S_a,S_b,S_c\} = \{1,1,1\}$ are

the zero vectors that effectively short-circuit the output, providing zero voltage. A list of 2L-VSI vectors, along with their corresponding switching states and output voltage values, is provided in Table 2.2.

Table 2.2 Voltage Vectors of a 2L-VSI.

V_i	$S = \{S_a S_b S_c\}$	$V_s = V_\alpha + jV_\beta$
V_0	000	0
V_1	100	$^2/_3\, V_{DC}$
V_2	110	$\left(^1/_3 + j\, ^1/_{\sqrt{3}}\right) V_{DC}$
V_3	010	$\left(^{-1}/_3 + j\, ^1/_{\sqrt{3}}\right) V_{DC}$
V_4	011	$^{-2}/_3\, V_{DC}$
V_5	001	$\left(^{-1}/_3 - j\, ^1/_{\sqrt{3}}\right) V_{DC}$
V_6	101	$\left(^1/_3 - j\, ^1/_{\sqrt{3}}\right) V_{DC}$
V_7	111	0

2L-VSI voltage vectors are depicted on the complex plane in Fig. 2.6.

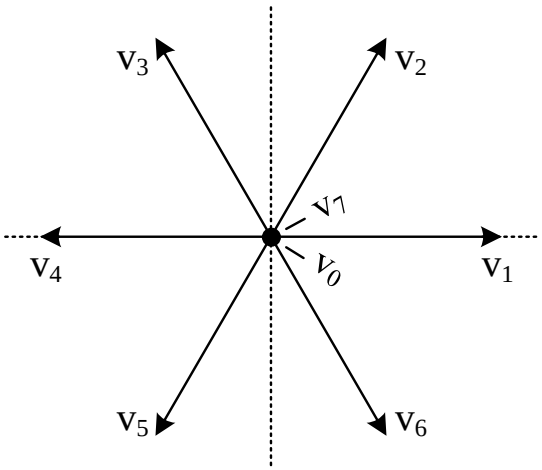

Figure 2.6. The voltage vectors of 2L-VSI, depicted on the complex plane.

2.3.2 Finite Control-Set Model Predictive Torque Control of an Induction Machine

The control action of FCS-MPC can be simply divided into three parts: estimation, prediction, and optimization. First, the instantaneous values of machine fluxes are estimated. Then, the impact of each admissible vector is obtained by the predictions. Finally, the optimum vector is found that serves the best in terms of control objectives. In the following, these three main parts of the FCS-MPC strategy are explained.

In motor control, machine fluxes nearly always need to be estimated as sensors for them are seldom used. Rather, we have current measurements available through the current sensors and know the stator voltage since it is applied by the inverter under control. Therefore, by the proper rearrangement of terms in the state-space equations of (2.4)-(2.9), one can obtain the formulas for stator (2.11) and rotor (2.12) flux estimations. Equation (2.13), which is derived from (2.6) and (2.7), defines the relation between stator and rotor fluxes.

$$\frac{d\Psi_s}{dt} = V_s - R_s I_s \tag{2.11}$$

$$\frac{d\Psi_r}{dt} = R_r \frac{L_m}{L_r} I_s - \left(\frac{R_r}{L_r} - jw_e\right)\Psi_r \tag{2.12}$$

$$\Psi_s = \frac{L_m}{L_r}\Psi_r + \sigma L_s I_s \tag{2.13}$$

where $\sigma = 1 - L_m^2/L_s L_r$ is defined as the leakage factor.

Equations (2.11) and (2.12) are commonly referred to as the "*voltage model*" and "*current model*" respectively. The voltage model is sensitive to stator resistance and problematic near zero speeds. Being a pure integrator, it has DC offset and integrator drift risks. The current model is sensitive to rotor parameters and slip. Since the accurate estimation of machine fluxes is crucial for all types of motor control types, several studies that implement higher performance flux estimators have been reported in the literature [52]–[59]. Further analysis on the subject will not be provided here as it is beyond the scope of this study. For FCS-MPC, it is convenient to use the current model for estimations and to use the voltage model for predictions.

Considering the digital implementation, the discretized versions of (2.12) and (2.13) can be obtained with the Euler approximation as shown in (2.14) and (2.15). The sampling period (or equivalently, the control period) is denoted by Δt.

$$\Psi_r(k) = \Psi_r(k-1) + \Delta t.\left(R_r \frac{L_m}{L_r} I_s(k) - \left(\frac{R_r}{L_r} - jw_e(k)\right)\Psi_r(k-1)\right) \tag{2.14}$$

$$\Psi_s(k) = \frac{L_m}{L_r}\Psi_r(k) + \sigma L_s I_s(k) \tag{2.15}$$

Having estimated the values of $\Psi_s(k)$ and $\Psi_r(k)$, the next step in the FCS-MPC routine is to predict the values of stator flux (2.16), current (2.17), and torque (2.18) at the next control cycle, under the influence of a particular voltage vector $V_i(k)$. The superscript *p* is used to indicate the predicted variables.

$$\Psi_s^p(k+1) = \Psi_s(k) + \Delta t.V_i(k) - \Delta t R_s I_s(k) \tag{2.16}$$

$$I_s^p(k+1) = \left(1 - \frac{\Delta t}{\tau_\sigma}\right) I_s(k) + \frac{\Delta t}{\Delta t + \tau_\sigma} \frac{1}{R_\sigma} \left(\left(\frac{k_r}{\tau_r} - k_r j \omega_e(k) \right) \Psi_r(k) + V_i(k) \right) \tag{2.17}$$

$$T_e^p(k+1) = 1.5p\Im\mathfrak{m}\left\{\Psi_s^{p*}(k+1) I_s^p(k+1)\right\} \tag{2.18}$$

where, $k_r = L_m/L_r$ is the rotor coupling factor, $R_\sigma = R_s + k_r^2 R_r$ is the stator referred equivalent resistance, $\tau_\sigma = \sigma L_s/R_\sigma$ is the stator transient time constant and $\tau_r = \sigma L_r/R_r$ is the rotor time constant.

After the predictions for a voltage vector are obtained, the outcomes in terms of stator flux magnitude and torque can be evaluated with a cost function. This action (prediction and cost function evaluation) is repeated for each admissible voltage vector. Although different forms for the cost function can be proposed, the conventionally used type is given in (2.19). A weighting factor λ is included to adjust the relative importance of torque and flux terms hence to tune the cost function. In this study, for both simulation and the experimental implementation, the λ value has been chosen experimentally, by a trial and error approach. Regarding the cost function design and how to tune the weighting factor λ, more details are provided in Chapter 2.6.

$$g = \left|T_e^{ref}(k) - T_e^p(k+1)\right| + \lambda \left| |\Psi_s|^{ref} - \left|\Psi_s^p(k+1)\right| \right| \tag{2.19}$$

It is also good practice to include a penalty factor in the cost function such that an infinite cost is assigned to a voltage vector if the current prediction of (2.17) foresees an overcurrent under the influence of that particular vector. This approach has been utilized in the experimental implementation. It provides current limiting via software and it is useful as a security figure especially during the early phases of the experimental studies.

Cost function design is a feature of MPC that gives it flexibility. Although only flux and torque parameters are included in the cost function for the typical motor drive implementation, additional cost criteria can also be inserted in the cost function such as common-mode voltage, capacitor voltage balance (for a multi-level inverter), and switching transition (to suppress the switching losses). In this way, the designer can track multiple control objectives within a single cost function.

Selection of the l_1 norm is popular in the literature, as is the case in (2.19). However, for the applications that penalize the control effort, l_2 norm is advised for better closed-loop stability [19].

The voltage vector, for which the cost function of (2.19) yields the minimum value, is selected as the optimum and applied at the next switching instant. The whole control routine of the FCS-MPC is depicted in Fig. 2.7.

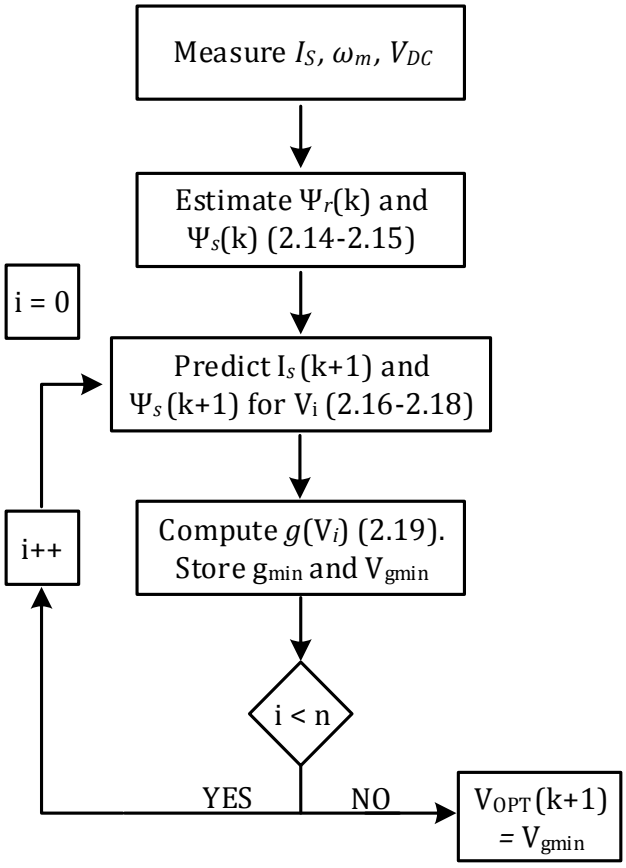

Figure 2.7. A simplified flowchart for the FCS-MPC, as utilized for the torque control of an IM drive.

It is also common practice to include the two-step ahead prediction approach for the compensation of computation time delay [60]. However, this is not employed here since the control frequency in the experimental implementation is set to a reasonably high value (40 kHz) and the computation time for the MPC routine is satisfactorily low (10.6 μs).

2.4 Predictive Torque Control of an Induction Motor: Simulation

Computer simulations regarding the control of an IM via FCS-MPC are carried out in MATLAB/Simulink environment. Simulations were intended as a preparatory step before the experimental implementation phase. The top-level on the simulation screen is depicted in Fig. 2.8.

The general approach for the simulation phase was to model the system and the predictive controller as close as possible to the physical implementation. Parameters of the actual IM that is used in the experimental implementation are set for the IM model in the simulation. The 2L-VSI model with near-ideal switches is used since the focus is on control performance rather than the efficiency of the inverter. The control action is taken under the subsystem named "*MPC*". The MPC block is modeled as a triggered subsystem, such that it is evaluated once a pre-determined control period. By doing so, the resemblance to the actual DSP implementation, on which the control action takes place on each interrupts triggered periodically, is maintained. Simulation step size is set to 1 μs, for satisfactory numerical accuracy.

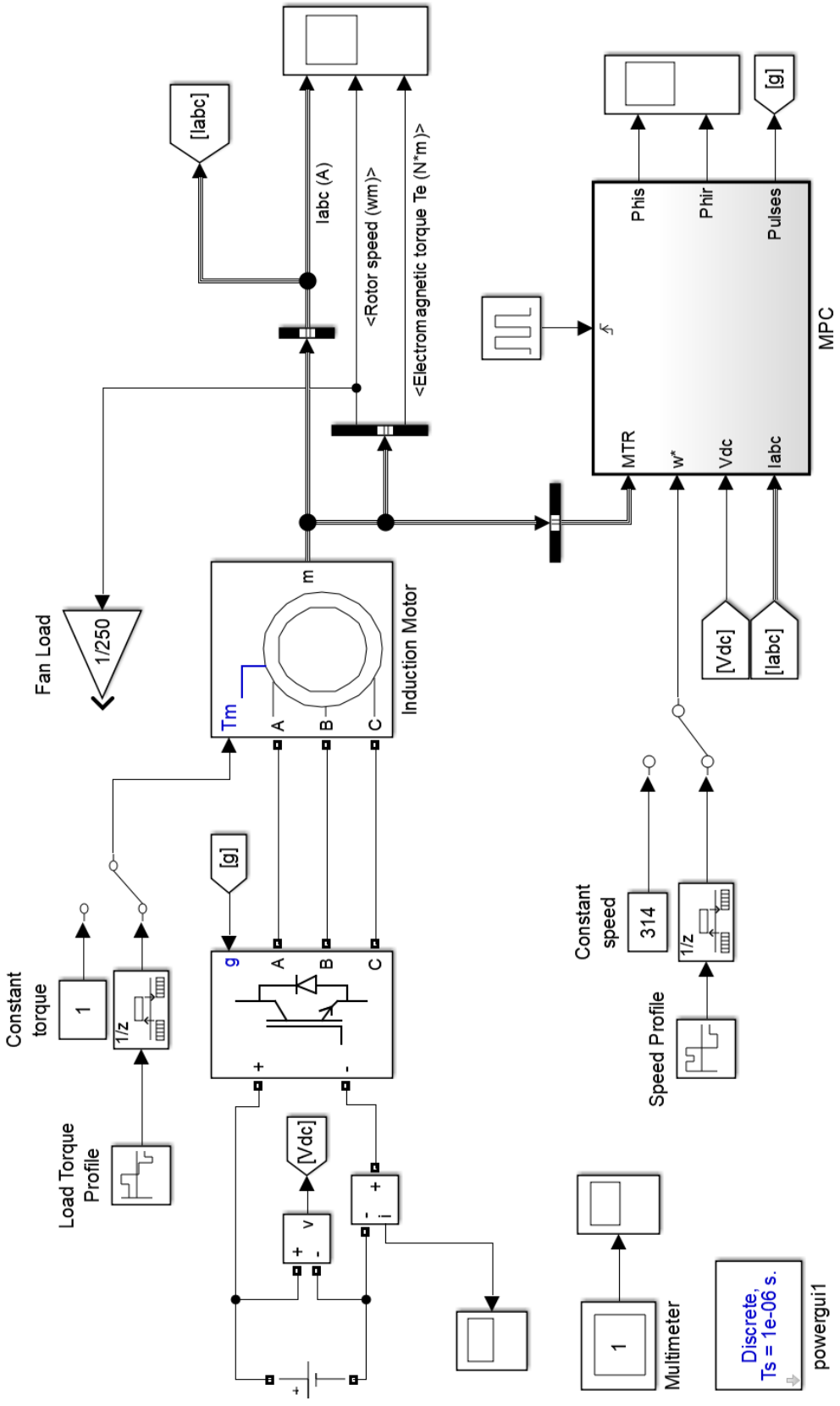

Figure 2.8. The top-level view of the simulation

The internal structure of the MPC block in the main simulation screen is shown in Fig. 2.9. Detailed descriptions of the blocks that are used to simulate MPC will not be provided here since they are merely the implementations of the formulas explained above. In the MPC block, estimations are absent since the flux values are taken from the IM model, for simplicity. Prediction and cost function evaluation is done for each admissible vector, as described above. Therefore, these are modeled with a for loop, inside view of which is provided in Fig. 2.10.

To evaluate the simulated system's performance as a motor drive, a drive scenario is created, which contains motoring actions such as starting from stand-still, sudden speed change, and speed reversal commands. Phase currents, shaft speed, and electromagnetic torque values for this motor drive scenario are plotted against time in Fig. 2.11. Simulation results show satisfactory performance as a motor drive. Because the focus is on the experimental results, further details on simulations will not be presented. The interested reader is referred to [61], where the simulation files have been made available as open-source.

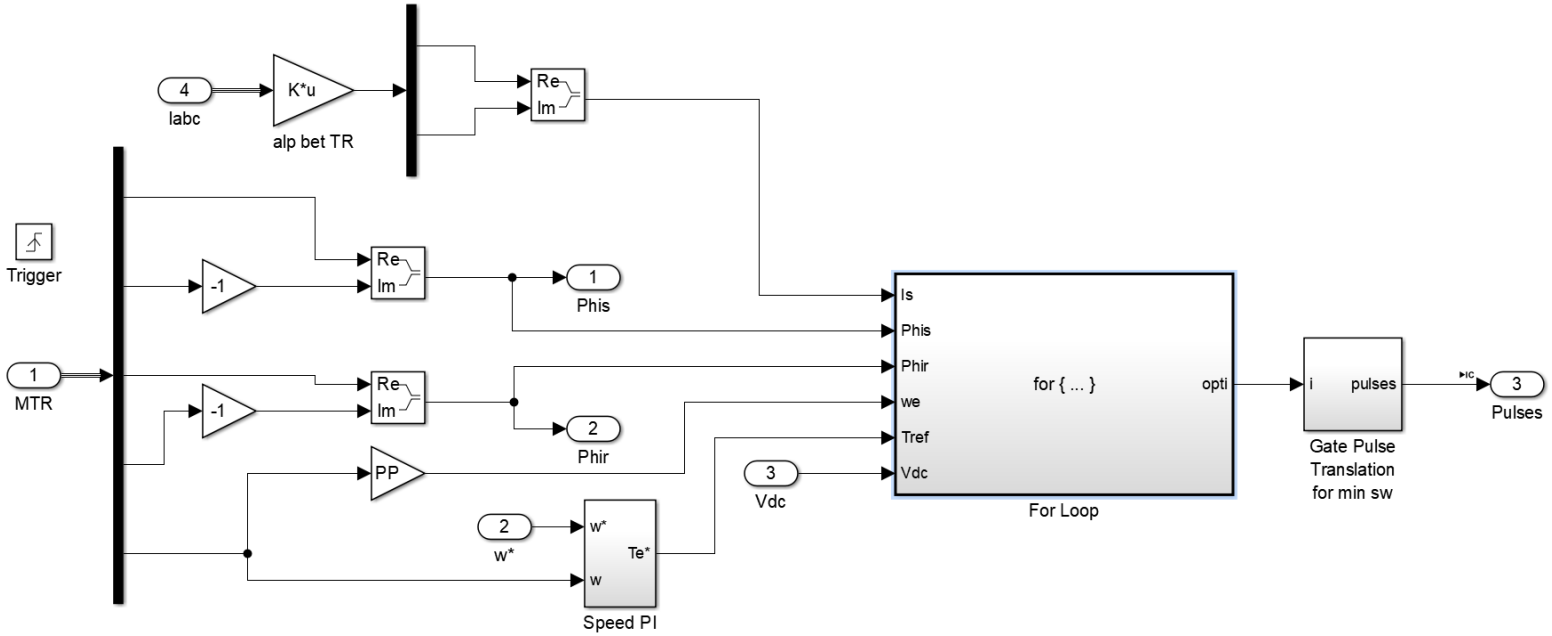

Figure 2.9. Inside view of the MPC block.

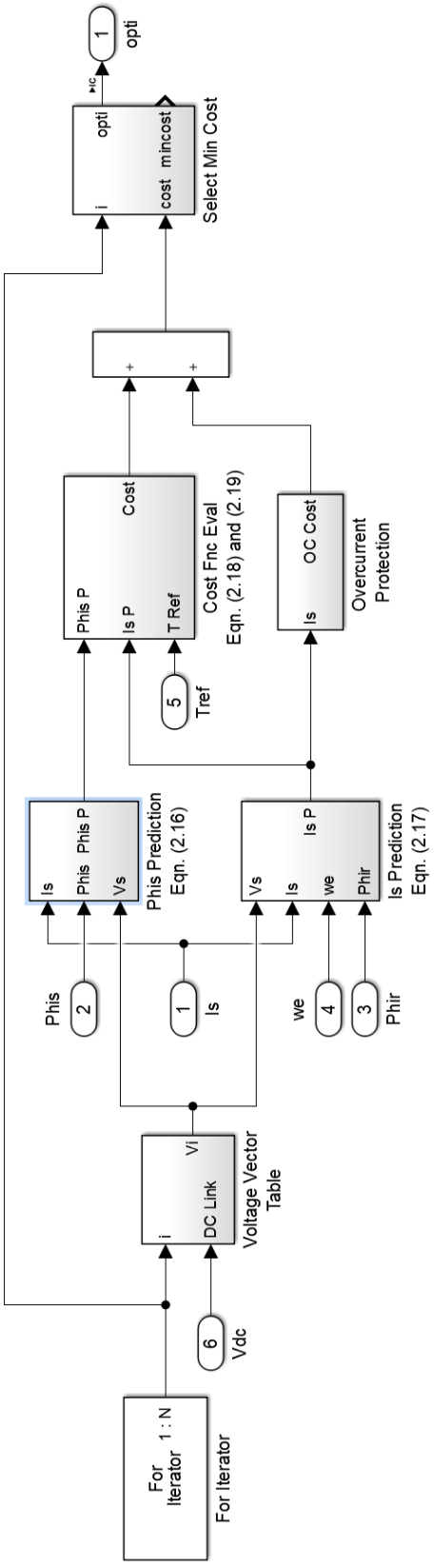

Figure 2.10. Inside view of the for-loop in which the main control action takes place.

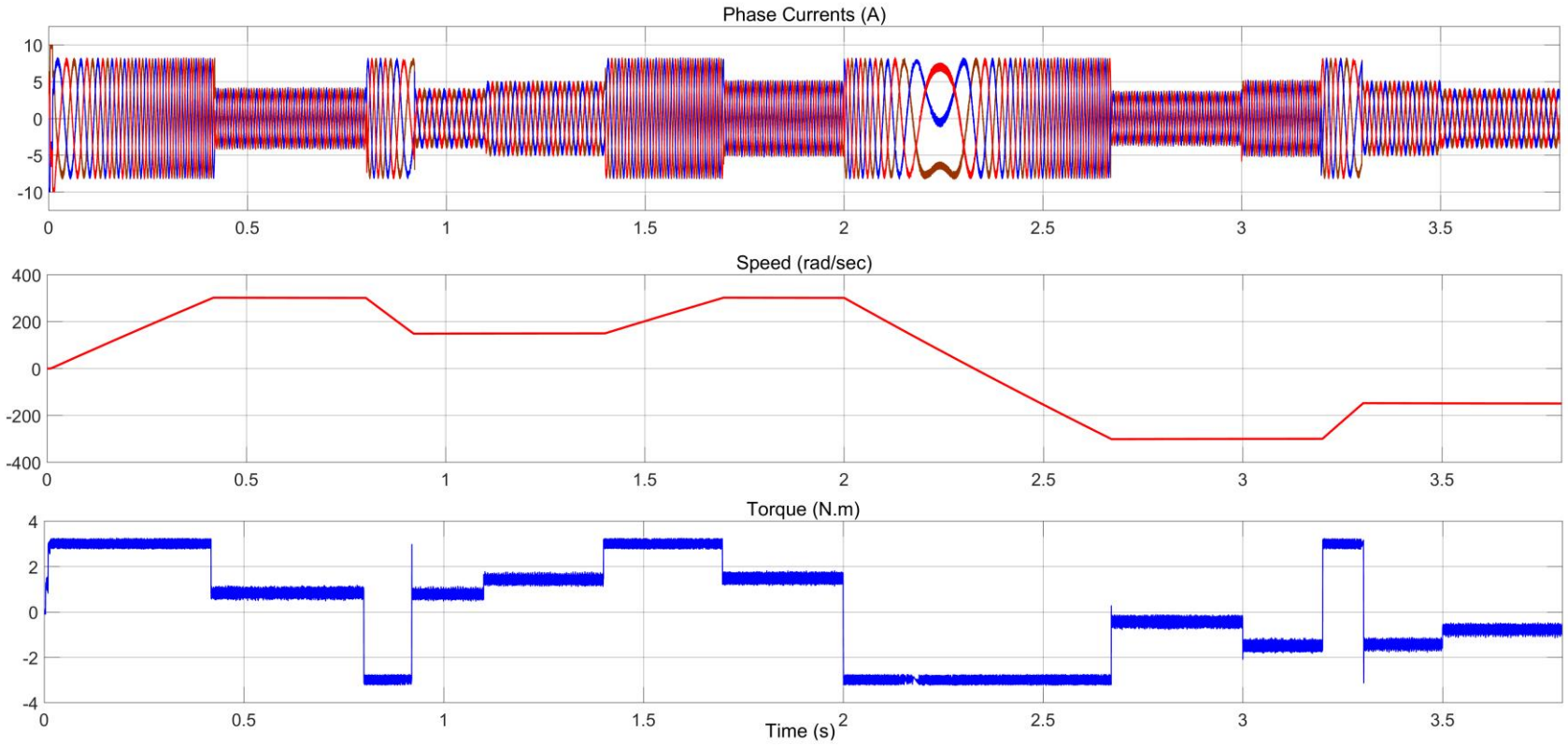

Figure 2.11. Phase currents, shaft speed, and electromagnetic torque for the motor drive scenario involving various operational conditions.

2.5 Predictive Torque Control of an Induction Motor: Experimental Implementation

In this chapter, a short survey on the experimental implementations regarding MPC research is presented first. Then the laboratory setup that is built for the realization of the predictive torque-controlled IM drive will be described. Finally, the experimental results depicting both steady-state and dynamic performance figures for the implemented motor drive are provided.

2.5.1 A Short Survey on Experimental MPC Implementations

Several examples of experimental MPC implementations are listed in Table 2.3. In this survey, only the applications of MPC as motor drives (as commonly addressed as: predictive torque control, PTC) are considered. The main motivation for this survey is to observe control platforms chosen by researchers worldwide who are experimenting with MPC. The increased computational burden was previously mentioned as a major issue with MPC. Therefore, special emphasis is put on control frequency (i.e. how often the predictive control routine is run in one second) of the reported implementations in Table 2.3.

It can be concluded from the survey depicted in Table 2.3 that, two main platforms for implementing experimental PTC hardware are dSPACE solutions and DSPs, which are mostly from Texas Instruments, (TI). Although dSPACE platforms provide MATLAB integration and eliminate the need for coding to a very large extend, in this study the motor drive development platform with the product code TMDXIDDK379D by TI, is chosen as the control platform.

Another conclusion that can be drawn from Table 2.3 is that the control frequencies in the range of 10 to 25 kHz are typical. In this study, control frequencies up to 50 kHz are implemented and the documented results are for 40 kHz, due to the powerful microprocessor chosen for the application.

Table 2.3 A Survey on the Control Platforms of Choice, for PTC Implementation

Reference	Control Platform	Control Frequency (kHz)
[62]–[64]	TMS320F28335	10
[65]	dSPACE DS1104	25
[37]	dSPACE DS1104	20
[66]	dSPACE 1004	20
[67]	TMS320F2812	25
[68]	PC Based, Custom-Made Platform of [69]	12
[70]	PC Based, Custom-Made Platform of [69]	16
[71]	PC Based, Custom-Made Platform of [69]	24

2.5.2 The Laboratory Setup

The functional overview of the laboratory setup is depicted in Fig. 2.12. An isolated DC voltage of adjustable magnitude is obtained by the rectification of floating AC voltages, obtained through isolation transformers. The motor drive development unit "TMDXIDDK379D" contains both the 2L-VSI and the microcontroller on which the MPC is programmed. The IM is coupled to a PMSM with a torque sensor in between them. Thus, the PMSM is run in generator mode and acts as a mechanical load for the IM. By changing the three-phase resistive load value that is connected to the PMSM, one can adjust the load torque level. For speed measurement, the encoder

integrated into the PMSM is used. Receiving the speed information not directly from the IM shaft but indirectly over the PMSM represents a measurement deficiency considering the rubber couplings and the torque sensor in between the machines. Nonetheless, satisfactory dynamic performance is achieved as will be documented in Section 2.5.4.2.

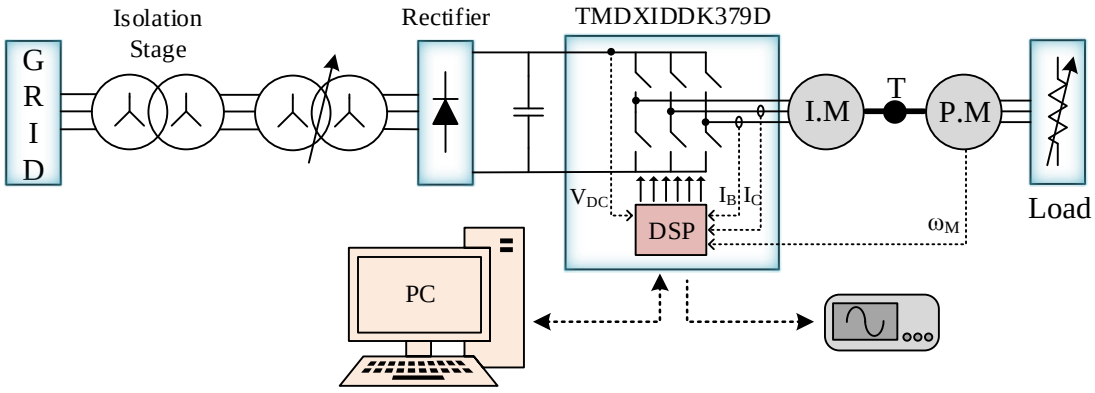

Figure 2.12. The functional overview of the laboratory setup.

An overview of the experimental setup, with the instruments marked with numbers for identification, can be seen in Fig. 2.13. Descriptions of the numbered items on Fig. 2.13 are listed in Table 2.4.

Table 2.4 The Items of the Experimental Setup

Number in Fig. 2.13	Item	Description
1	3Φ supply	380 V, 50 Hz
2	Adjustable Autotransformer	0-430 V, 13.5 kVA
3	Isolation Transformers	3 x 500 VA Single Phase 1:1
4	3Φ Diode Rectifier	–
5	PMSM	Anaheim Auto. – EMJ-04APB22
6	Torque Sensor	Magtrol – TM308
7	Induction Motor	*See Table 2.5*
8	Waveform Analyzer	Hioki – 3193-10
9	Adjustable Resistive Load	40~200Ω per phase
10	Oscilloscope	Tektronix – TPS2024
11	Switch	–
12	Multimeter	Fluke 115
13	Motor Drive Development Kit	TI – TMDXIDDK379D
14	PC	–
15	Torque Sensor Interface	Magtrol Model 3410

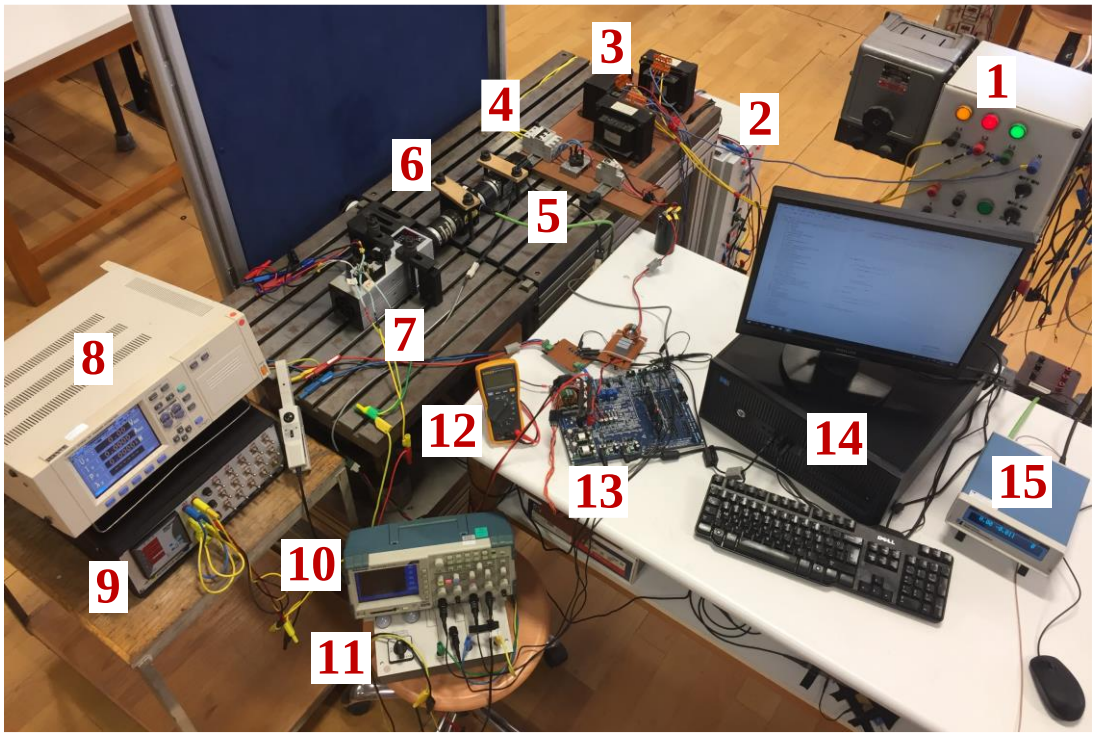

Figure 2.13. An overview of the experimental setup.

2.5.2.1 Motor Drive Development Kit: TMDXIDDK379D

In the experimental setup, a special emphasis should be put on TMDXIDDK379D. It is a motor drive development platform, produced by Texas Instruments (TI) [72]. It includes the modern TMS320F28379D microprocessor, which is a dual-core, floating-point DSP, with a 200 MHz clock frequency [73], [74]. The motor drive development platform TMDXIDDK379D, houses a 2L-VSI with all of the additional hardware required for a typical motor drive, such as current and speed measurement circuits. Further details on the hardware structure of the product, in addition to some critical safety instructions, can be found in [75]. A photo of TMDXIDDK379D is provided in Fig. 2.14. Although it was originally intended as a development platform regarding the FOC of PMSM [76], the FCS-MPC of IM has been established by proper modification of the existing libraries and sample codes. During the

experiments, control parameters can be observed and adjusted on the fly, over the computer interface. Moreover, the DAC modules of TMDXIDDK379D are also utilized to observe control variables in real-time.

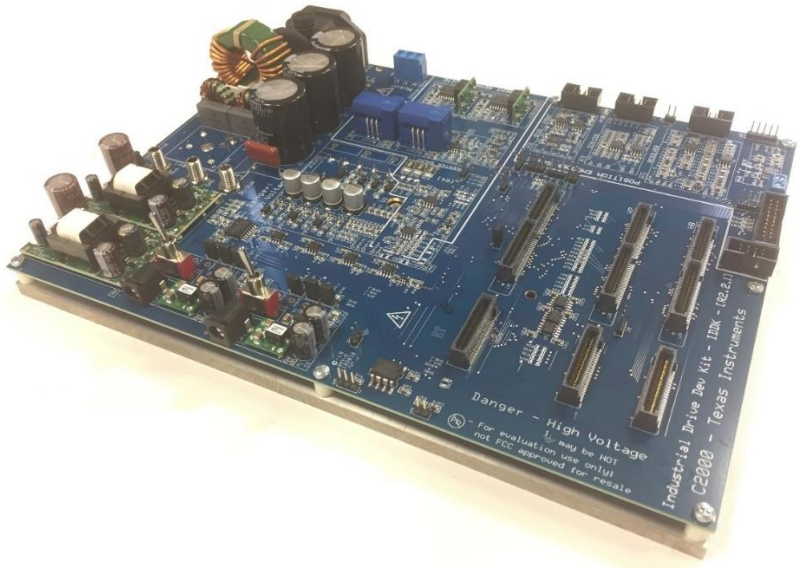

Figure 2.14. TMDXIDDK379D, the motor drive development platform produced by Texas Instruments [72], [75].

2.5.2.2 The Induction Motor

During the experimental studies conducted for this thesis, a series of induction motors have been installed to the laboratory motor drive setup. Only the last motor will be presented here, which is a custom-modified motor with extra connections are made available on one of its phases. These extra connections are utilized for the creation of inter-turn short circuit faults to test and develop fault detection algorithms. This feature will be described in detail in the following chapters. A photo of the test motor is provided in Fig. 2.15.

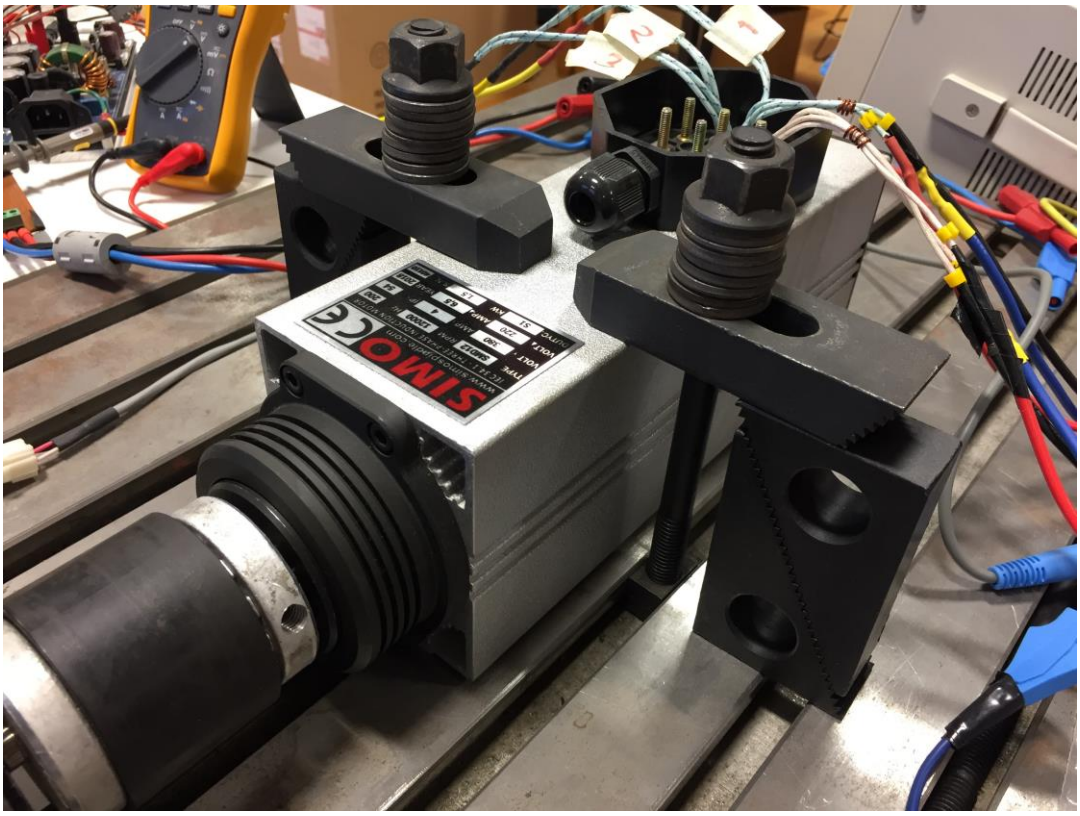

Figure 2.15. A photo of the IM used in the experiments.

The IM used in the experimental setup was originally designed as a 200 Hz spindle motor. Its nameplate reads: 380 V, 4 A, and 1500 W. Due to the limitations imposed by the experimental setup (manually adjusted mechanical couplings do not seem to handle speed values beyond 5000 rpm and the maximum DC bus level of the development kit is 400V), the nameplate data could not be tested. More importantly, the IM has no datasheet or any associated technical document. Therefore, 1.2 N.m. torque at 3000 rpm (roughly 50 Hz operation) is assumed as the base value for the implementation. The motor's electrical parameters are found via no-load and locked-rotor tests and related measurements, as described in [77]. Additionally, the fine-tuning for the elements of the equivalent circuit is done via experimental analysis based on the cost function and current prediction error minimization. The motor parameters along with the re-defined base values are summarized in Table 2.5.

Table 2.5 Induction Machine Parameters

Name	Symbol	Value
Apparent Power	S	640 VA
Stator voltage	V_{ab}	128 V
Stator current	I	2.9 A
Base frequency	f	50 Hz
Torque	T_L	1.2 N.m
Number of poles	p	2
Number of turns in one phase	N_s	104
Stator resistance	R_s	2.3 Ω
Rotor resistance	R_r	3.1 Ω
Magnetizing inductance	L_m	98 mH
Stator leakage inductance	L_{ls}	4 mH
Rotor leakage inductance	L_{lr}	2 mH
Stator flux magnitude reference	$\lvert\Psi_s\rvert^{ref}$	0.3 Wb

The IM was initially driven with a stator flux magnitude reference of $|\Psi_s|^{ref} = 0.4\,Wb$, which corresponds to an increased flux operation with $V_{ab} \cong 150V$, as documented in [16]. It is also worthwhile to note that the magnetizing inductance drops down to $L_m = 90\,mH$ due to the magnetic saturation for this increased flux operation. Later on, $|\Psi_s|^{ref}$ is set to 0.3 Wb since the machine yields better efficiency and power factor for this level of flux. Therefore, the laboratory results presented in this chapter are obtained for $|\Psi_s|^{ref} = 0.3\,Wb$ setting. For the fault detection studies which will be presented in the following chapters, the results for both the increased and decreased flux cases are presented for the sake of completeness and in order to utilize the magnetization level as a parameter in the fault detection performance.

2.5.3 Software Aspects of the FCS-MPC Implementation

Coding the FCS-MPC to the microprocessor constitutes the largest share of the workload of the experimental implementation. However, this workload has been significantly lessened with the availability of sample codes and macros provided by TI. Although the application reports that shed light on the practical implementations of MPC-based motor drives have not been reported yet, TI offers a large collection of sample codes and motor drive libraries that include macros for commonly used operations, generally considering FOC. These complementary materials are compiled under user interfaces such as controlSUITE [78] and its successor C2000WARE [79] and they are made available as freeware on the TI webpage.

A simplified scheme depicting the main units of the FCS-MPC code is shown in Fig. 2.16. The parts, for which the corresponding code has been inherited from the readily available sources, are drawn in green color, to show the degree of simplification.

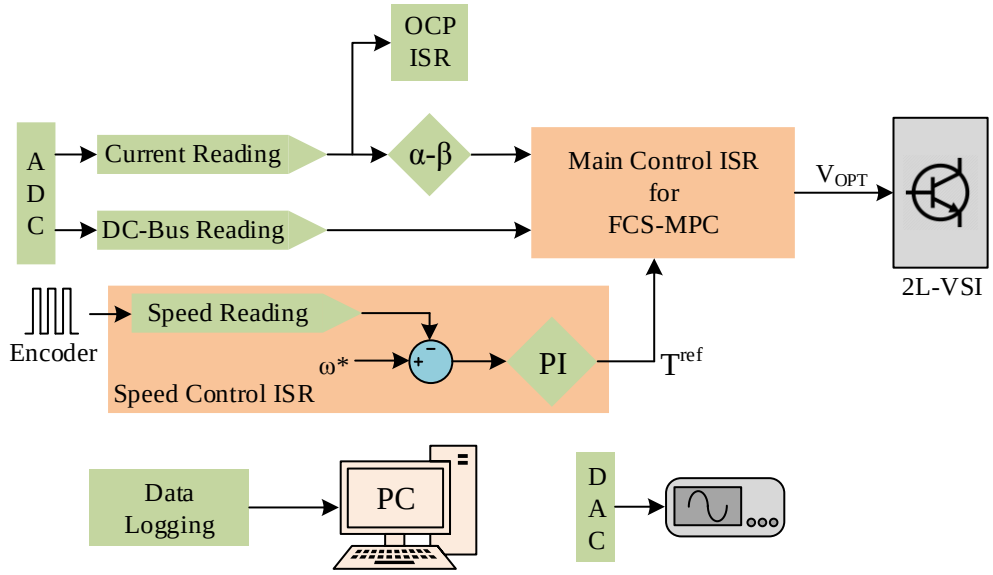

Figure 2.16. Main blocks of the FCS-MPC based IM drive code.

The main body of a typical DSP code is simply idle, continuously running "while loop". The control action is implemented with interrupts, commonly referred to as interrupt service routines (ISRs), that arise with a pre-determined frequency and execute the tasks that they are programmed to. In the sample code for the FOC of a PMSM inherited from [76], the main control ISR, along with several other auxiliary ISRs or sequential tasks of varying frequencies (for secondary tasks such as over-current protection (OCP), data-logging, speed loop, etc.) are provided. By the proper modification of these, the code for predictive torque control of an IM has been implemented. Frequency values ranging from 20 to 50 kHz have been implemented for the main control loop. As expected, enabling the control action in smaller time steps yields lower current ripple values. The experimental results provided in the following are obtained for a sampling frequency (or equivalently, control frequency) of 40 kHz.

The main control ISR block in Fig. 2.16 is simply the code that executes the flowchart depicted in Fig. 2.7 and described by the equations (2.4)-(2.19). For the practical implementation, several equations are re-visited as in (2.20)-(2.26).

Complex vectors are evaluated by their real and imaginary components separately. Although the estimation (2.14),(2.15), and prediction (2.16),(2.17) equations are provided in their discrete forms, further simplification of these equations is beneficial for discrete implementation and coding. Revisited forms of (2.14)-(2.17) are given in (2.20)-(2.26) with the definitions of new terms listed below the equations. Note that $v_{s\alpha}$ and $v_{s\beta}$ stand for the normalized output voltage vectors of the 2L-VSI in $\alpha\beta$ domain. L_{lkg} is defined as $L_{lkg} = \sigma L_s$.

$$\Psi_{r\alpha}(k) = C_1\Psi_{r\alpha}(k-1) - V_1\Psi_{r\beta}(k-1) + C_2 i_{s\alpha}(k) \quad (2.20)$$

$$\Psi_{r\beta}(k) = C_1\Psi_{r\beta}(k-1) + V_1\Psi_{r\alpha}(k-1) + C_2 i_{s\beta}(k) \quad (2.21)$$

$$\Psi_{s\alpha}(k) = k_r\Psi_{r\alpha}(k) + L_{lkg} i_{s\alpha}(k) \quad (2.22)$$

$$\Psi_{s\beta}(k) = k_r\Psi_{r\beta}(k) + L_{lkg} i_{s\beta}(k) \quad (2.23)$$

$$\Psi_{s\alpha}(k+1) = \Psi_{s\alpha}(k) + V_2 v_{s\alpha}(k) - C_3 \mathrm{i}_{s\alpha}(k) \quad (2.24)$$

$$\Psi_{s\beta}(k+1) = \Psi_{s\beta}(k) + V_2 v_{s\beta}(k) - C_3 i_{s\beta}(k) \quad (2.25)$$

$$i_{s\alpha}(k+1) = C_4 i_{s\alpha}(k) + V_3 v_{s\alpha}(k) + C_6\Psi_{r\alpha}(k) + V_4\Psi_{r\beta}(k) \quad (2.25)$$

$$i_{s\beta}(k+1) = C_4 i_{s\beta}(k) + V_3 v_{s\beta}(k) + C_6\Psi_{r\beta}(k) - V_4\Psi_{r\alpha}(k) \quad (2.26)$$

where;

$$C_1 \triangleq 1 - \frac{\Delta t R_r}{L_r} \qquad C_2 \triangleq \Delta t R_r \frac{L_m}{L_r} \qquad C_3 \triangleq \Delta t R_s \qquad C_4 \triangleq 1 - \frac{\Delta t}{\tau_\sigma}$$

$$C_5 \triangleq \frac{\Delta t}{\Delta t + \tau_\sigma}\frac{1}{R_\sigma} \qquad C_6 \triangleq C_5 \frac{k_r}{\tau_r}$$

$$V_1 \triangleq \Delta t w_e(k) \qquad V_2 \triangleq \Delta t V_{DC}(k) \qquad V_3 \triangleq C_5 V_{DC}(k) \qquad V_4 \triangleq C_5 k_r w_e(k)$$

For the new terms utilized in (2.20)-(2.26) and described above, it is important to note that C_1-C_6 represents fixed gains whereas V_1-V_4 represents variable gains. Therefore, the FCS-MPC code can pre-calculate C_1-C_6 at the beginning and store the values thus eliminate the need for computing them at each control cycle, reducing computation time. On the other hand, V_1-V_4 are related to time-varying parameters

such as speed and DC bus voltage therefore their current values should be re-visited at each control cycle.

Regarding the PWM units, a deadtime interval of 2 μs is adapted in the sample code and this setting is kept for the laboratory implementation. A deadtime compensation algorithm is proposed in [80] for predictive controlled inverters. Since the deadtime interval set for the implementation was found satisfactorily small, no compensation algorithm is implemented.

An over-current penalty is set at 9 A by assigning an infinite cost for the cost function of (2.19), as described in Chapter 2.3.2. An additional over-current protection routine (as illustrated with "OCP" in Fig. 2.16) is set at 10.5 A, which neutralizes all PWM units once the pre-determined current threshold is sensed.

The source codes for the implemented MPC drive system, under various projects with several C files that correspond to the experiments of different nature, are provided as open-source in [61]. The novel fault detection algorithm, which will be described in Chapter 4, can also be found in the same repository.

2.5.4 Experimental Results

In this section, experimental results obtained from the predictive torque control implementation will be documented. The results are investigated under two categories: steady-state performance and dynamic performance. Throughout the experiments, the DC link voltage was 350 V.

2.5.4.1 Steady-State Performance Figures

The implemented motor drive was operated under several shaft speed and load torque conditions. Mechanical readings are obtained via the (Magtrol) torque sensor and the electrical readings are obtained via the (Hioki) waveform analyzer. The operating conditions are enumerated thorough (a) to (k) and the corresponding readings are

tabulated in Table 2.6. Note that, due to the fan-load characteristics of the PMSM and the resistive load bank configuration, maximum load torque is speed-dependent. Therefore, nominal torque cannot be loaded for low-speed regions. Nonetheless, operating conditions for Table 2.5 correspond to different speed references with load torque on and off. The three-phase motor currents are recorded for each of the operating conditions (a) to (k) and depicted in Fig. 2.17 and Fig.2.18. The stator phase current waveforms depicted in Fig. 2.17 and Fig. 2.18 are obtained with the "acquire" mode of the oscilloscope TPS2024 is set to the average display mode of 4 samples.

Table 2.6 Steady-state performance figures of the motor drive, under several different operating conditions

Case	Magtrol Torque-Meter		Hioki Waveform Analyzer		
	Speed (rpm)	Torque (N.m)	V_{l-n} (V)	I (A)	$P_{3\Phi}$ (W)
(a)	4500	1.2	108.2	2.83	636
(b)	4500	0.3	100.0	2.00	132
(c)	3750	1.3	94.8	2.95	591
(d)	3750	0.3	86.2	2.05	114
(e)	3000	1.35	78.9	2.98	502
(f)	3000	0.3	70.9	2.10	99
(g)	2250	1.3	62.8	2.90	382
(h)	2250	0.3	54.7	2.13	82
(i)	1500	1.1	44.2	2.71	242
(j)	1500	0.3	37.8	2.16	63
(k)	300	0.1	9.6	2.16	35

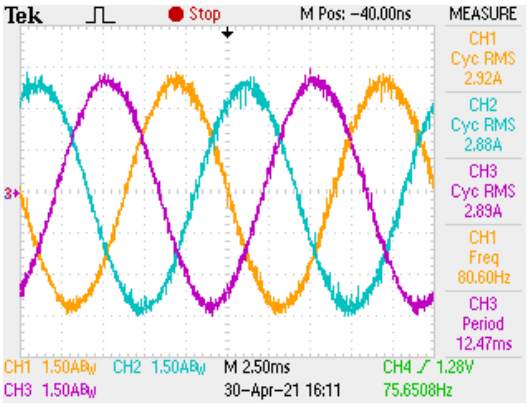

a) $w = 4500\ rpm, T_e = 1.2\ N.m$

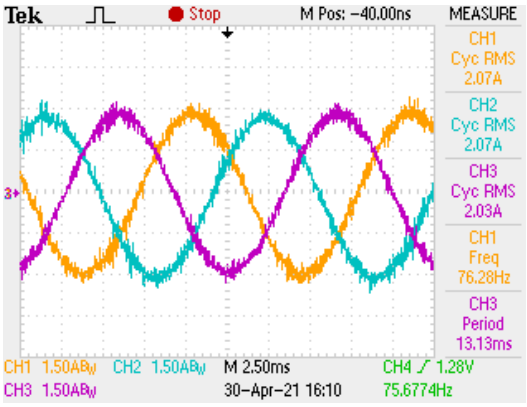

b) $w = 4500\ rpm, T_e = 0.3\ N.m$

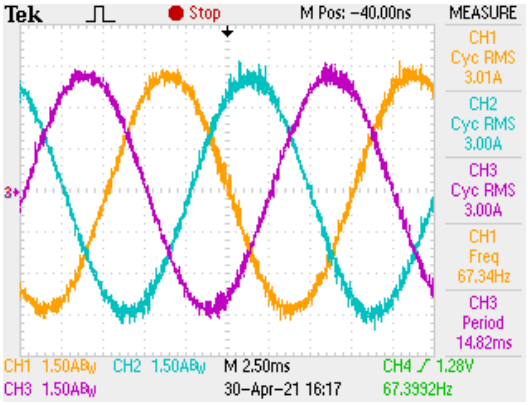

c) $w = 3750\ rpm, T_e = 1.3\ N.m$

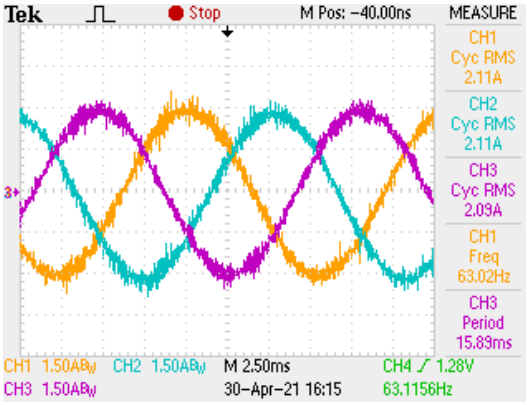

d) $w = 3750\ rpm, T_e = 0.3\ N.m$

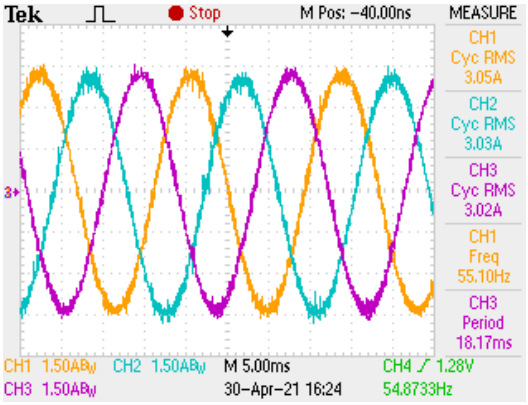

e) $w = 3000\ rpm, T_e = 1.35\ N.m$

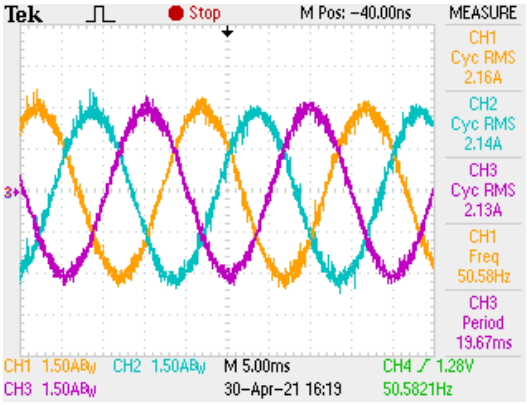

f) $w = 3000\ rpm, T_e = 0.3\ N.m$

Figure 2.17. Stator current waveforms for the operating conditions defined in Table 2.6.

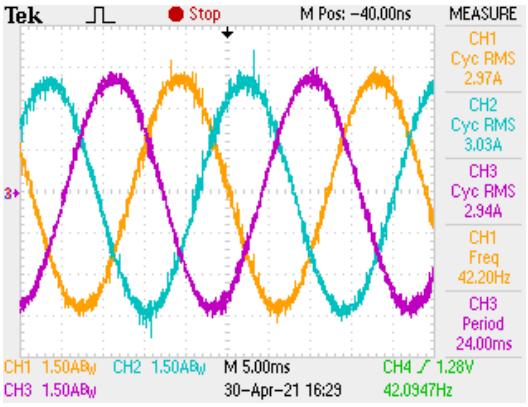

g) $w = 2250\ rpm, T_e = 1.3\ N.m$

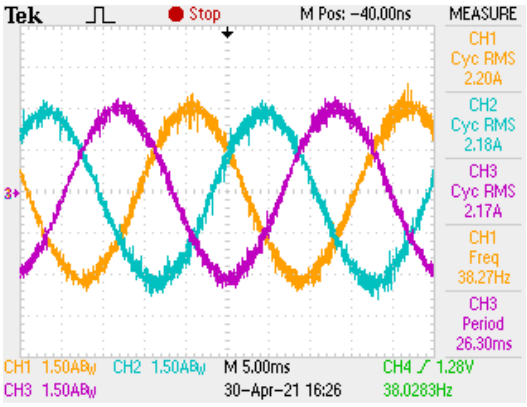

h) $w = 2250\ rpm, T_e = 0.3\ N.m$

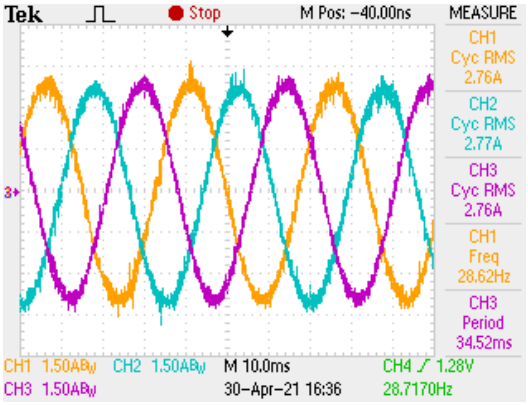

i) $w = 1500\ rpm, T_e = 1.1\ N.m$

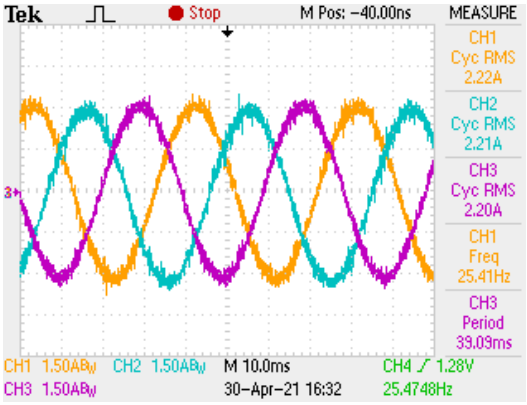

j) $w = 1500\ rpm, T_e = 0.3\ N.m$

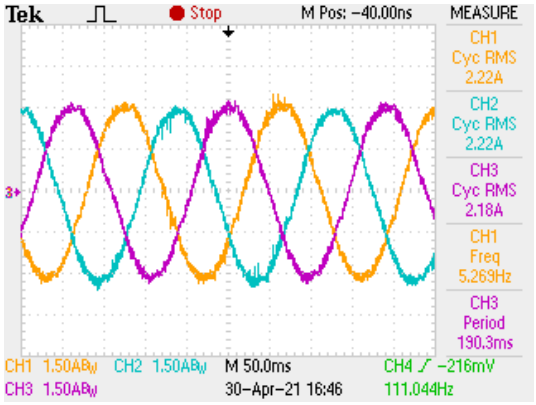

k) $w = 300\ rpm, T_e = 0.1\ N.m$

Figure 2.18. Stator current waveforms for the operating conditions defined in Table 2.6, continued.

Observation of the inverter output voltage is helpful during the control code development and testing phase. Therefore, a low pass filter circuit, the circuit diagram of which is depicted in Fig. 2.19 is implemented and added in parallel to the inverter output. In Fig. 2.19, R_1=270 kΩ, R_2=10 kΩ and C=100 nF.

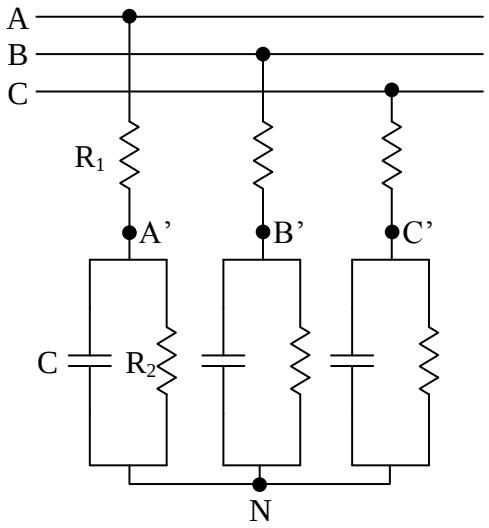

Figure 2.19. The low-pass filter, utilized at the inverter's output.

The low-pass filtered output voltage waveforms for two different operating conditions $\omega = 3000\, rpm, T_e = 1.35\, N.m$ and $\omega = 1500\, rpm, T_e = 0.9\, N.m$ are depicted in Fig. 2.20 (a) and (b) respectively.

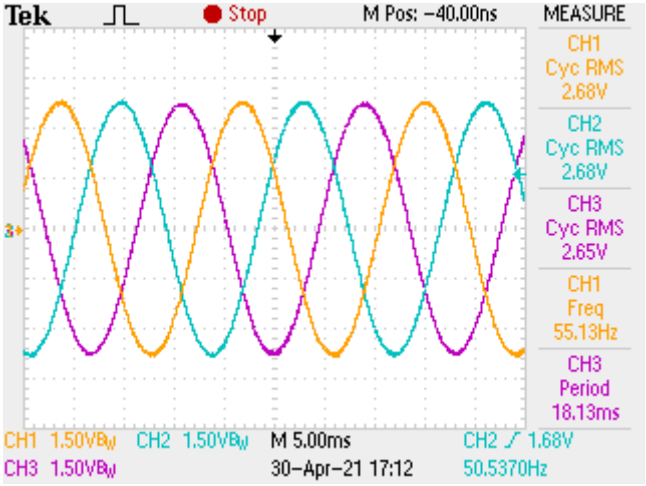

a) $\omega = 3000\ rpm, T_e = 1.35\ N.m$

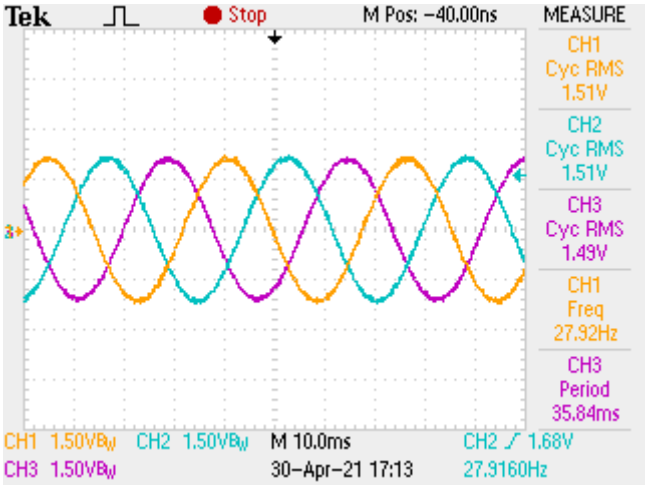

b) $\omega = 1500\ rpm, T_e = 0.9\ N.m$

Figure 2.20. The low-pass filtered output voltages for $\omega = 3000\ rpm, T_e = 1.35\ N.m$ (a), and $\omega = 1500\ rpm, T_e = 0.9\ N.m$ (b).

Similarly, the DAC pins of the TMDXIDDK379D motor drive development board are frequently utilized during code development and testing studies. Control quantities can be fed into the DAC pins which are then translated into voltages and can be observed via an oscilloscope. In Fig.2.21 (a), and (b), the Ψ_s waveform is shown both in time with α and β components and in XY-view, respectively. The DAC approach to illustrate the control parameters will be further revisited in the fault diagnosis studies that are presented in Chapter 4.

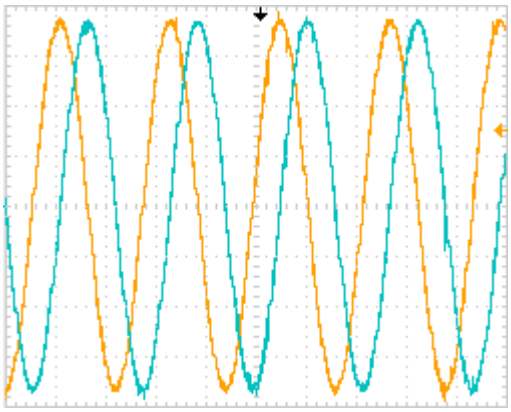

a)

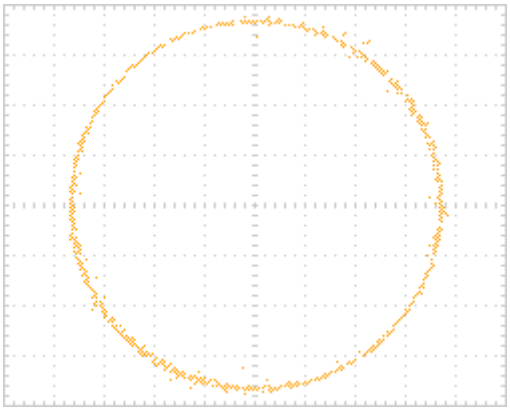

b)

Figure 2.21. The Ψ_s estimation, $\Psi_{s\alpha}$ and $\Psi_{s\beta}$ versus time (a), and the flux pattern in XY-view (b).

2.5.4.2 Dynamic Performance Figures

To observe the implemented controller's performance as a motor drive, several tests regarding the dynamic operation have been conducted. The first dynamic operation to be presented is the instantaneous speed reversal operation, which corresponds to a speed transition of $\pm 4500\ rpm$ under rated load torque. The drive's response can be evaluated from Fig. 2.22, on which the speed reference and the measured speed are depicted with (a) and without (b) phase current waveform. The speed reference and the speed measurement waveforms are observed over the DAC pins of the drive, thorough proper scaling. The corresponding values are marked on the graph. It can

be observed from Fig. 2.22 that, the speed reversal of $\pm 4500\ rpm$ is achieved under 0.5 seconds, without any risk of losing control.

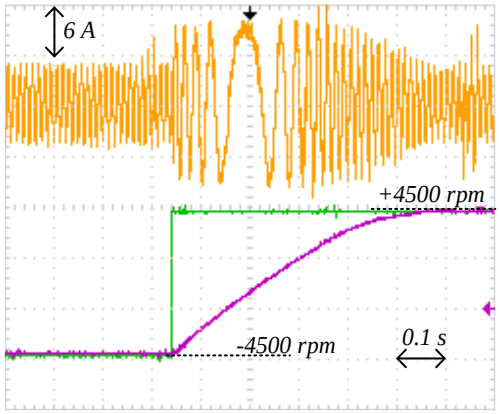

a)

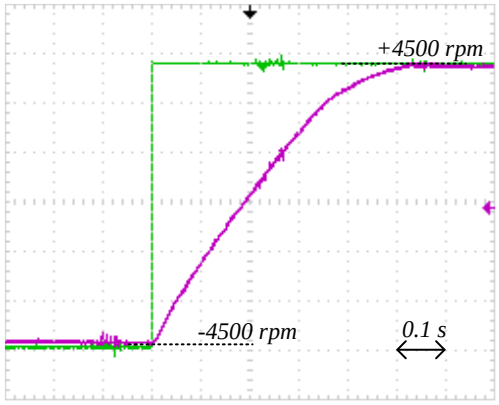

b)

Figure 2.22. Phase current (orange), speed reference (green), and measured speed (purple) waveforms during sudden speed reversal operation from -4500 to +4500 rpm.

Secondly, the ability of the implemented controller to track the speed reference is tested by providing a continuously changing speed reference rather than a fixed value. This operation is depicted in Fig. 2.23 with (a) and without (b) phase current waveform. It can be concluded from Fig. 2.23 that the controller can successfully track a time-varying speed reference. During this operation, the PMSM and the resistive load pair is arranged such that $\zeta_e = 1.35\ N.m$ for $\omega = 4500\ rpm$.

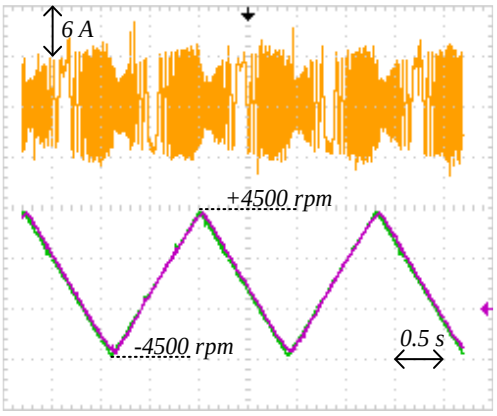

a)

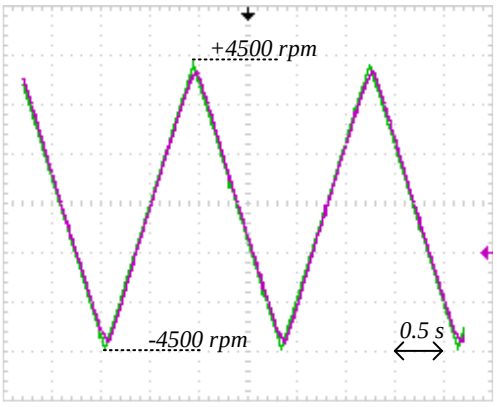

b)

Figure 2.23. Phase current (orange), speed reference (green), and measured speed (purple) waveforms for operation under a time-varying speed reference.

Similar to the dynamic test above, the controller is commanded with abruptly changing speed references of 500 rpm and 4500 rpm. Drive's response to these abrupt changes in speed reference can be seen on Fig. 2.24, with (a) and without (b) phase current waveform. During this operation, the PMSM and the resistive load pair is arranged such that $\zeta_e = 1.35\ N.m$ for $\omega = 4500\ rpm$.

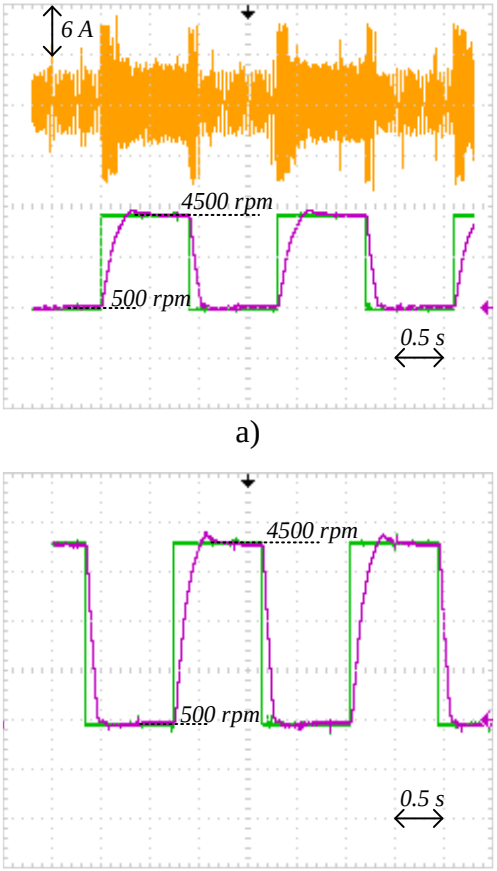

Figure 2.24. Phase current (orange), speed reference (green), and measured speed (purple) waveforms for operation under abruptly changing speed references.

Implemented motor drive's response against abrupt changes in load torque is tested by applying sudden loading/load removal while the motor is operating at its rated speed of 3000 rpm. Corresponding waveforms are shown in Fig. 2.25 (a), for loading and (b), for load removal cases. It can be observed that the drive's torque response is satisfactorily fast. Mainly due to the very low inertia of the system, rotational speed slightly changes with the torque loading/removal. The change in speed is less than 6%, and it is soon corrected by the speed control loop.

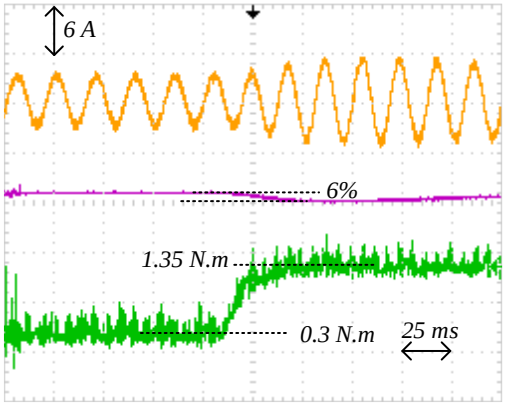

a)

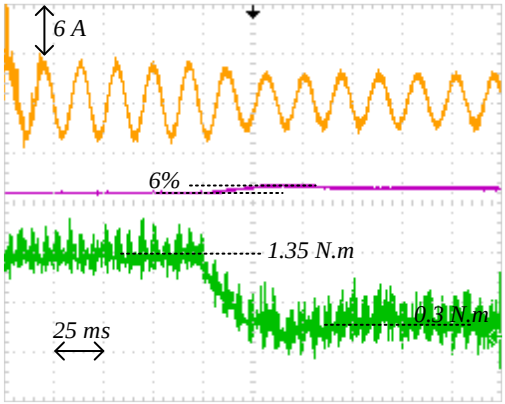

b)

Figure 2.25. Phase current (orange), torque (green), and measured speed (purple) waveforms for sudden loading (a), and load removal (b) cases.

Finally, waveforms regarding the motor start operation which depicts the change from stand-still to rated speed are presented in Fig. 2.26.

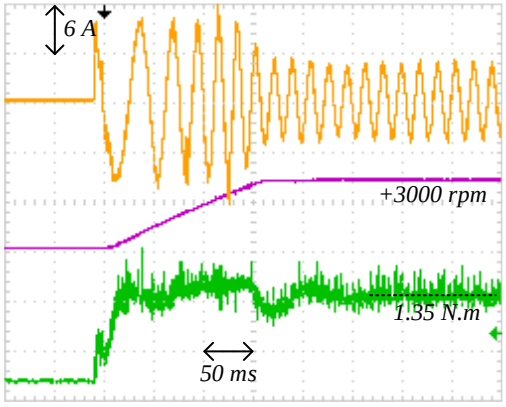

Figure 2.26. Phase current (orange), torque (green), and measured speed (purple) waveforms for sudden start operation.

Although the main purpose for the laboratory implementation was a general application of FCS-MPC as a motor drive and no special attention was given to the optimization and fine-tuning of the drive characteristics, the presented test results, for both steady-state and dynamic cases, display a motor drive operation with satisfactory performance. The implemented controller can establish a speed reversal command from -4500 rpm to 4500 rpm in about half a second and also it can track time-varying speed references that change considerably fast, like a servo-drive. It is worthwhile to note that most waveforms regarding the dynamic response were obtained via single sequence operation of the oscilloscope that is triggered with a pre-defined threshold to catch the time-varying signal. Hence, no averaging or filtering is active for the waveforms. Therefore, noise-related spikes can be observed on the waveforms, which should be disregarded.

2.6 Further Issues Regarding FCS-MPC Implementation

In this chapter, a selection of topics such as execution time of the control routine and the weighting factor determination process will be discussed. Additionally, a novel algorithm that adjusts the weighting factor λ during the motoring operation, in order to achieve a better dynamic response, is presented.

2.6.1 Execution Time for the Control Cycle

As previously mentioned, the increased computational burden of the FCS-MPC is a well-recognized drawback. There are several studies reported in the literature to address this shortcoming [12], [37], [81]–[84]. A fundamental proposition to reduce the computational load is to consider the voltage vectors which are different by only one switching state compared to the last one considered, as shown in [83]. In [37], the prediction vector set is reduced by inheriting the vector grouping approach of DTC. For a PMSM drive, the vector selection effort is minimized by addressing the voltage vector that is found by a deadbeat solution approach in [84]. For an MV drive with a long prediction horizon, the possible switching sequences are reduced with a branch and bound algorithm in [82]. Based on the stator current vector and the operation mode that is expected from the drive, a prediction vector set reduction method is proposed in [12].

The code execution time for the main control loop is measured by setting a DAC pin high at the beginning, and clearing it at the end of the control loop, as shown in Fig. 2.27. Thanks to the powerful microprocessor [74], the execution time is merely 10.6 μs. This allows the implementation of a rather high control frequency of 40 kHz, which can also be observed from Fig.2.27.

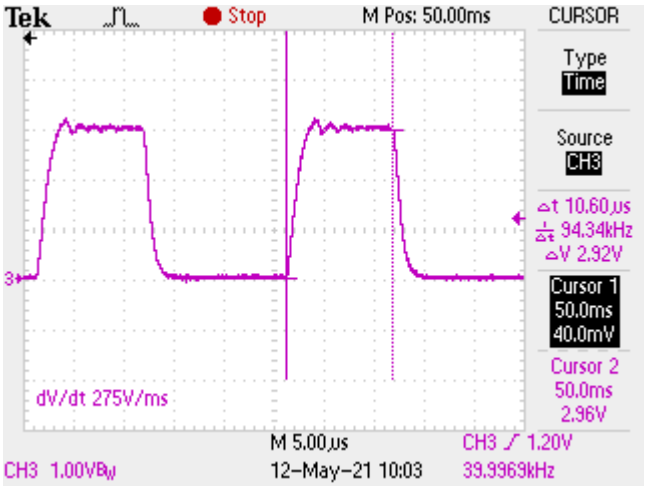

Figure 2.27. The execution time for the main control loop, measured as 10.6 µs.

Studies regarding computational cost reduction often consider applications with long prediction horizons and/or applications that involve multi-level converters for which the prediction vector set would be much larger. Since the implementation presented in this thesis is a low-voltage, low-power drive based on a 2L-VSI, switching frequencies of several kHz ranges are quite normal. Therefore, long-horizon MPC was not found promising for the laboratory setup hence was not implemented. Consequently, no further attempts are made for the reduction of the computational burden, which is already very low as shown in Fig. 2.27.

2.6.2 Weighting Factor Tuning

Without the utilization of classical PID blocks in the control action, the selection of the weighting factor becomes the fundamental tool to tune the response of the FCS-MPC type controllers. A first attempt to provide general empirical design guidelines is presented in [85]. An algebraic approach to tune for the weighting factor design is suggested in [86]. Valuable discussions on weighting factor design, along with other practical design issues such as control horizon, sampling interval, and control effort penalization are presented in [19]. The use of artificial neural networks (ANN) is proposed for weighting factor design in [87].

The cost function design becomes more important and challenging for the applications where the switching vector transitions are penalized to limit the switching frequency and a long horizon approach is adopted. In the experimental implementation of this thesis, a low-voltage fed 2L-VSI is utilized with a rather high sampling frequency of 40 kHz for a short horizon, without any switching penalization. Therefore, a simple tuning process is adopted: the weighting factor λ is adjusted by observing THD values of motor phase currents. In AC motor drives, it is very desirable to synthesize near-pure AC current waveforms as any distortion or harmonic content in the current waveforms directly translate into the torque ripple, hence deteriorate the motor drive performance. Furthermore, it is experimentally quite convenient to observe and evaluate the current waveform quality through the THD figures. Consequently, the weighting factor λ is varied, the THD value of phase current is observed via the waveform analyzer, while the motor is run at its rated speed of 3000 rpm. The resulting graph is depicted in Fig. 2.28 where the THD value is plotted against λ on a logarithmic scale. For the calculation of the THD value, a low pass filter is set at 5 kHz by the waveform analyzer.

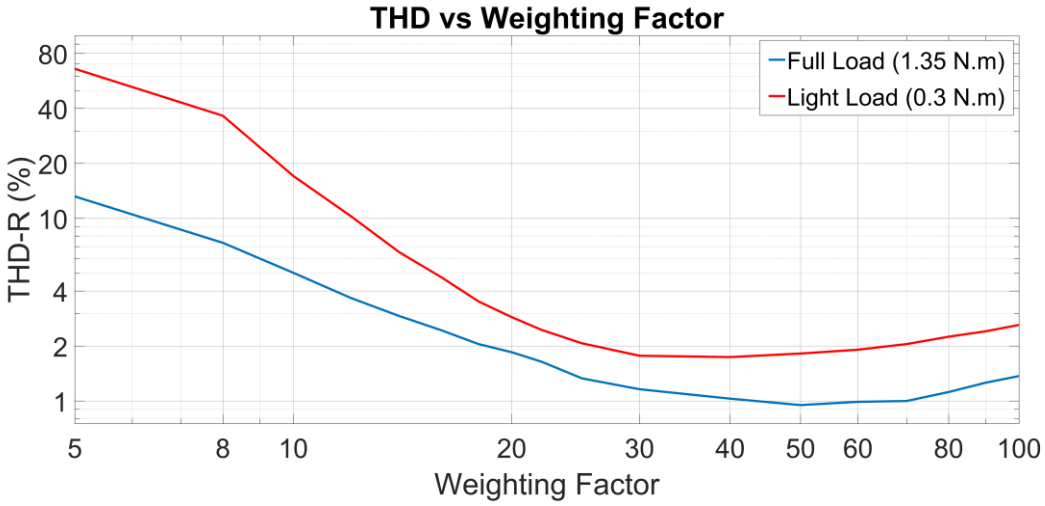

Figure 2.28. Phase current THD versus varying values of weighting factor (λ) for full load and light load at 3000 rpm.

It is observed that for small values of λ (such as $\lambda < 20$), the phase current waveform is perceptibly distorted. As an example, a distorted phase current waveform obtained for light-load operation at 3000 rpm with $\lambda = 8$ case is shown in Fig. 2.29. Looking at the cost function structure defined in (2.29), one can see that the increasing values of λ put more emphasis on the flux magnitude error. Since the flux estimations are current based, this action implicitly improves current waveform quality. From the THD graph of Fig. 2.28, it is seen that increasing λ yields better THD results up to a certain level. Therefore, $\lambda = 50$ is chosen for the weighting factor value as this point is approximately the best spot for current waveform quality for the rated operating point.

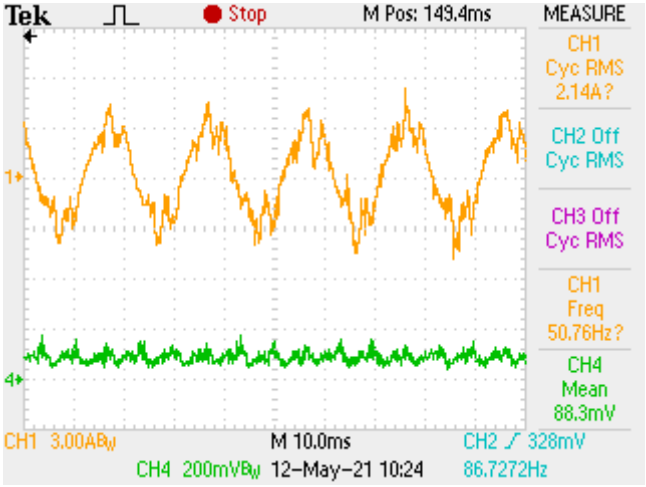

Figure 2.29. Distorted phase current waveform for the operating condition $\zeta_e = 0.35\ N.m, \omega = 4500\ rpm$ for $\lambda = 8$.

2.6.3 Dynamically Modified Weighting Factor

There have been several studies in the literature which propose updating the weighting factor λ during the operation, rather than assuming a fixed value [14], [87]–[89]. By doing so, the controller response can be optimized such that different control tasks are prioritized for different operating scenarios. Weighting factors are calculated as continuous variables depending on the preexisting errors in the respective control variables in [87]. In [88], the weighting factor is optimized in such

a way that the torque ripple is reduced. Neural networks are utilized to tune the weighting factors for a three-level neutral point clamped (NPC) inverter in [89].

For the cost function defined in (2.19), in which no penalization for the control effort to reduce the switching frequency is employed, a very simple approach to dynamically adjust the weighting factor is proposed in [14]. From the preceding discussions on λ, it can be concluded that the increasing values of λ puts more emphasis on current quality. However, during the speed transients, it may be beneficial to reduce the λ value in order to increase the relative importance of the torque error term. A simple formula to address any speed transient situation is given in (2.27). The magnitude of the difference of measured speed and commanded speed (will be called "the speed error" hereon) indicates whether the motor is run in steady-state or a speed transition is on the way.

$$\Delta\omega = \left|\omega_{ref} - \omega_{actual}\right| \tag{2.27}$$

The weighting factor can be adjusted with respect to the speed error term $\Delta\omega$, in such a way that a high value of λ is used in order to minimize the THD for steady-state operation, but λ is decreased to put more emphasis on the torque error term once a dynamic operation is indicated by the speed error term. This variation in λ with respect to $\Delta\omega$ is shown on Fig. 2.30, in which a quadratic relation in between the terms is assumed.

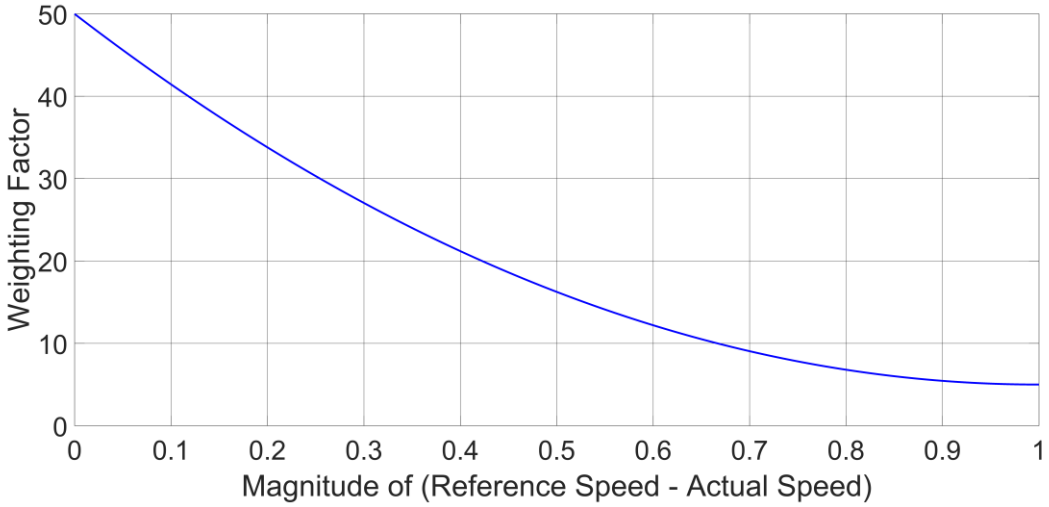

Figure 2.30. Dynamically adjusted λ with respect to $\Delta\omega$.

The effectiveness of the proposed method is tested with the speed reversal operation from -3000 rpm to +3000 rpm under rated load torque, which is depicted in Fig. 2.31, for a fixed value of $\lambda = 50$ for the weighting factor (a) and a dynamic variation of λ with respect to $\Delta\omega$ (b), as shown in Fig. 2.30. The transition time can be observed to be decreased from 276 ms to 210 ms.

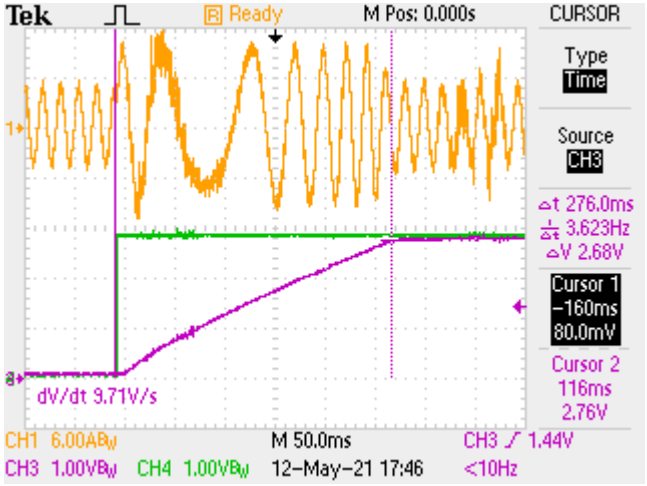

a) Fixed $\lambda = 50$ case

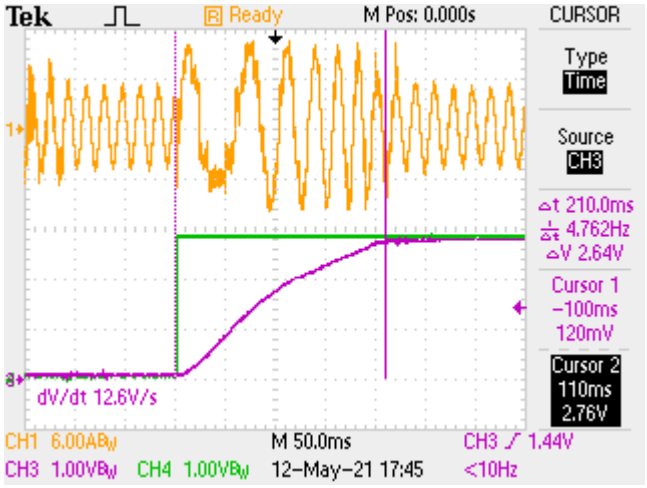

b) Dynamically adjusted case $\lambda(\Delta\omega)$

Figure 2.31. Speed reversal operation of ±3000 rpm under rated load torque, for the fixed $\lambda = 50$ case, and the dynamically adjusted case $\lambda(\Delta\omega)$ (b).

The presented technique is shown to be effective for improving the dynamic response without sacrificing the steady-state performance figures. With the flux magnitude reference of $|\Psi_s|^{ref} = 0.4\ Wb$ (as employed in [14]), the proposed method produced further dynamic performance benefits.

2.7 Conclusion

A comprehensive analysis on FCS-MPC, as applied to the torque control of an IM, is presented in this chapter. The relatively new control method of FCS-MPC is explained in full detail with extensive references to the literature. Both the simulation and experimental studies are conducted and the performance of the implemented motor drive is documented via detailed laboratory results. With the application of FCS-MPC, the implemented motor drive establishes good performance figures for both the steady-state and dynamic modes of operation. Further topics that include computation cost, weighting factor selection, and on the fly weighting factor manipulation are also covered.

In this chapter, a normal induction motor without any fault or abnormality is considered. In the following chapters of the dissertation, machine faults will be considered starting at Chapter 3. Predictive control of an induction motor which suffers an inter-turn short circuit fault on one of its phases will be established in Chapter 4, where the flexibility and fast control response properties of MPC will be utilized for fault detection purposes.

CHAPTER 3

MODELLING OF INTER-TURN SHORT CIRCUIT FAULTS IN INDUCTION MOTORS

3.1 Introduction

In this chapter, fault diagnosis and condition monitoring of electrical machines are considered. Special emphasis is put on the stator inter-turn short circuit (ITSC) faults of induction motors (IMs). Based on the existing models of IM, a new MATLAB-Simulink model, which can simulate the IM with an ITSC fault, is developed.

3.2 Fault Diagnosis and Condition Monitoring of Induction Machines

Considering the vast number of electrical machines utilized worldwide and the critical tasks that they are responsible for, the importance of fault diagnosis and condition monitoring of electrical machines becomes obvious. A swift detection of a machine's fault at an early stage can avoid catastrophic damage, provided that suitable counter-measures are taken to mitigate the fault's effect. Considering an industrial plant utilizing electric motors, this in turn would provide cost savings, extended plant availability, and smooth plant operation [90]. Similarly, for the areas in which electrical motors are utilized such as electric transportation, military, or aerospace, which are considered mission-critical applications, an effective fault diagnosis ability would bear even more significance. Owing to these aspects, fault diagnosis has been an intensive focus of research over the past decades. The interested reader is referred to the review papers [91]–[93] and the books [94], [95] on fault diagnosis and condition monitoring of electrical machines, to examine the plethora of publications on the subject.

Several different sources of electrical machine faults are grouped and depicted in Fig. 3.1, as adapted from [96].

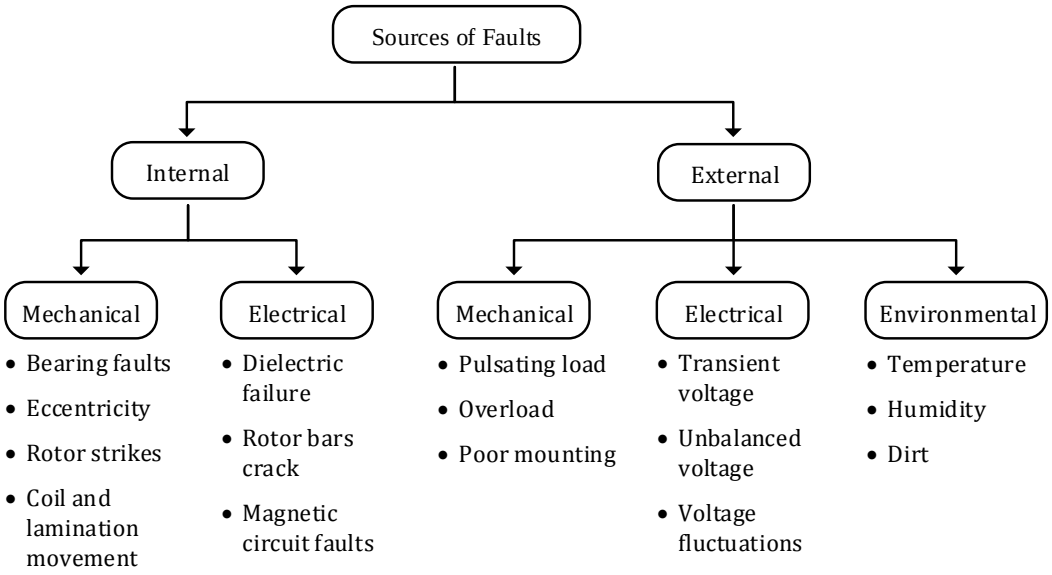

Figure 3.1. Sources of electrical machine faults, adapted from [96].

IM is the most widely used type of electrical motor due to its low cost and ruggedness. The surveys of [97], [98] provide an overview of the numerous publications regarding the fault diagnosis and condition monitoring of IM. Similar reviews are provided for PMSMs in [99], [100].

The IM faults can be broadly classified into three groups, according to their place of occurrence:

- Stator faults
- Rotor faults
- Bearing faults

The percentage distributions of the total faults are depicted in Fig. 3.2. The fault statistics for Fig. 3.2 (a) and 3.2 (b) are adopted from [101] and [102], respectively. Although the motor type, for which the fault data was collected, was not explicitly mentioned in [101], an IM assumption is valid since the data was collected from industrial applications, where the dominating majority of motors is IM. For the fault

numbers given in [102] (page 272, Table 10-19), the ones that correspond to the IM have been utilized for the corresponding figure. It can be concluded from Fig 3.2 that, roughly two-thirds of motor faults are seen in bearings and another fifth in the stator windings. Further information regarding the cause and analysis of stator and rotor failures of IM can be found in [103].

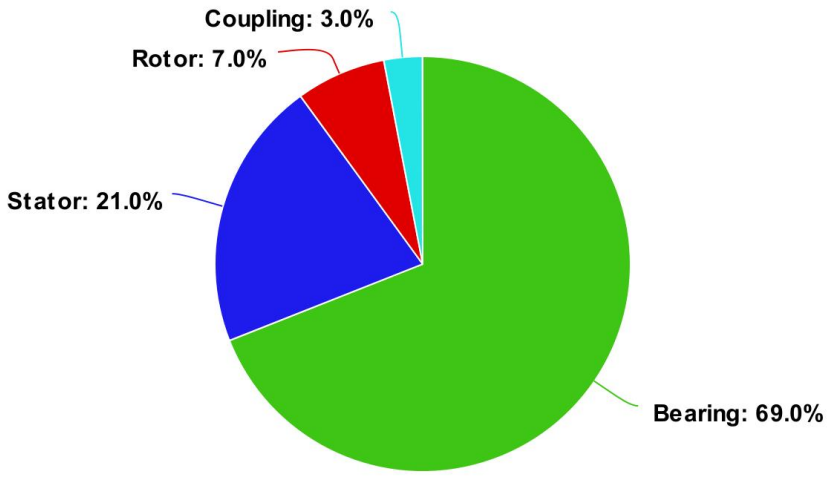

(a) Statistical data obtained from [101]

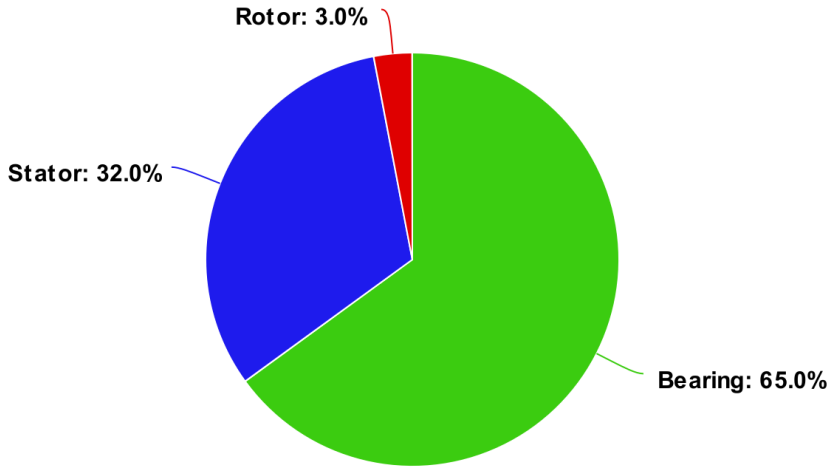

(b) Statistical data obtained from [102]

Figure 3.2. Percent distribution of overall faults for the IM.

The primary focus of this study is the stator faults of IM, which account for 21-32 % of the overall faults, as shown in Fig. 3.2. The insulation material in electric motors are prone to aging due to the corrosive effects such as oxidation, thermo-mechanical stress, vibration, contamination by moisture and oil [104]. The stator faults in IM usually start as turn-to-turn short circuits due to the loss of insulation at some part of the winding [105]. The over-current in the shorted turns quickly creates a hot spot. The inter-turn short circuit (ITSC) faults can evolve into complete phase to phase or phase to ground faults unless the fault is detected and intervened at an early stage. Hence, the detection of an incipient ITSC fault is critical.

Inverter-fed motors are at even more risk of suffering from both ITSC [106] and bearing faults [107], compared to mains-fed ones. Voltage surges from inverters can lead to gradual degradation and finally the loss of winding insulation [106]. Wire samples were tested under adjustable PWM pulses against insulation failure in [108], and the relationship between the fast rise time and failure time is shown. As the emerging modern semiconductor technologies, such as SiC and GaN, become more popular and their utilization in electric drives increases [109], ITSC fault detection is also estimated to be more critical as the machine windings will be experiencing inflicting voltage waves with much higher $^{dV}/_{dt}$ values [110].

Once an ITSC fault is spotted, some countermeasures can be executed by the inverter such as shorting the faulty phase [111] or creating a flux weakening current [112]. For a multi-phase machine, a current injection method to cope with an ITSC fault is proposed in [113]. For an overview of the existing ITSC fault mitigation techniques, the interested reader is referred to [114].

Several clues can be inspected in order to detect an inflicting fault. These can be simple observations such as an unexpected increase in machine temperature, vibration, unbalanced phase currents, etc. Although these basic observations were utilized in the early years of fault diagnosis research, modern studies utilize more advanced and complicated techniques. Modern approaches for fault diagnosis in electrical machines can be broadly classified into three categories [115];

- Observations on fault signatures
- Model-based techniques
- Artificial intelligence-based techniques

In the first category, the fault signatures embedded in the electrical quantities, such as phase currents or voltages, of the motor are investigated in the time and/or frequency domain. The presence of an inter-turn short circuit fault gives rise to negative sequence components and additional components in the harmonic spectra. These fault signatures are then utilized to detect the presence of a fault. To see the current harmonic spectra examples of the induction motors with ITSC and broken rotor faults, the reader is referred to [116]. Similarly, in the second category, the model of the machine is compared to the original case where any inflicting fault would result in an unexpected change. Finally, the third category is for artificial intelligence-based techniques which involves neural networks, expert systems, genetic algorithms, etc. The techniques under this group may require extensive fault data and/or a training period, but they are less sensitive to motor asymmetries and power supply unbalance [115]. For a broader survey and comparison of the existing literature regarding the stator fault diagnostics of IM, the interested reader is referred to [117], [118].

3.3 A New Simulation Model for the IM with an ITSC Fault

In this section, a new Matlab-Simulink model for the IM, which allows the simulation of an IM with an ITSC, is introduced. The mathematical model of the faulted machine is presented first. Then, the new simulation model is developed, which adopts the “voltage behind reluctance, (VBR)” approach.

3.3.1 Modeling the IM with an ITSC

The stator winding of an IM with an ITSC fault on one of its phases is depicted in Fig. 3.3. The loss of insulation between the faulty turns appears as a fault resistance R_f, which then causes the fault current I_f flow over. The ratio of the number of short-circuited turns to the total number of turns in one phase is defined as $N_f/N = \mu$, and it is a direct measure for the severity of an ITSC.

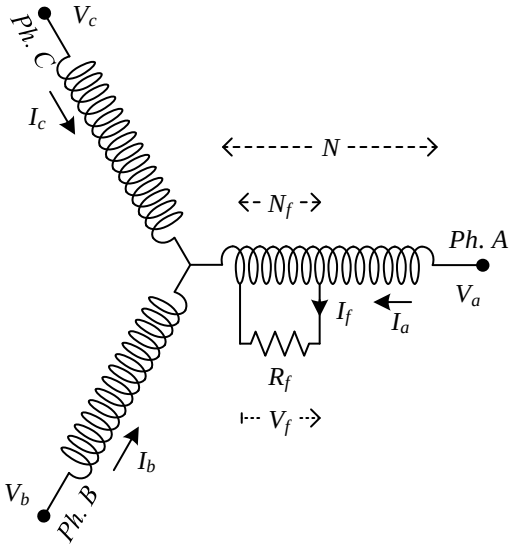

Figure 3.3. The three-phase stator winding of an IM, with an inter-turn short circuit fault of N_f turns on its Phase-A.

There have been several attempts to provide the mathematical model of the IM with an ITSC fault [119]–[123]. In this study, the formulation presented in [120] is adapted with the assumption of the linear distribution of leakage inductance over the faulty turns, i.e. $L_{f-lkg} = \mu L_{ls}$. It is important to note that, for a complete characterization of an ITSC, the motor and winding geometry should be considered in full detail with electromagnetic properties of the core included. Nonetheless, simplified analytical models are still very useful because for most of the time, the main purpose is to diagnose the fault rather than providing its detailed

characterization. Finite element analysis (FEA) based computer simulations can be utilized for a comprehensive profiling of an ITSC fault [124]–[127].

The state-space modeling of a healthy (normal) IM is provided in Chapter 2. The state-space modeling of the IM, properly modified to represent an ITSC (arbitrarily assumed on Phase A) can be summarized as (3.1)-(3.5). Similar to Chapter 2, the formulas hereon are represented from the stationary reference frame, with the complex vector notation: $f_{\alpha\beta} = f_\alpha + jf_\beta$.

$$V_s = R_s I_s + \frac{d\Psi_s}{dt} - \frac{2}{3}\mu I_f R_s \tag{3.1}$$

$$V_r = R_r I_r + \frac{d\Psi_r}{dt} - jw_e \Psi_r \tag{3.2}$$

$$\Psi_s = L_s I_s + L_m I_r - \frac{2}{3}\mu I_f L_s \tag{3.3}$$

$$\Psi_r = L_m I_s + L_r I_r - \frac{2}{3}\mu I_f L_m \tag{3.4}$$

$$\mathrm{T}_e = \frac{3}{2} p L_m \left(I_{s\beta} I_{r\alpha} - I_{s\alpha} I_{r\beta}\right) + p\mu L_m I_f I_{r\beta} \tag{3.5}$$

Voltage equations for the shorted turns can be expressed by (3.6) and (3.7) respectively, where V_f is the voltage and Ψ_f is the flux linkage across the shorted turns. The magnetizing flux in the shorted terms is represented with Ψ_{fm} and is as defined in (3.8).

$$V_f = R_f I_f = \mu R_s (I_{s\alpha} - I_f) + \frac{d\Psi_f}{dt} \tag{3.6}$$

$$\Psi_f = \mu L_{ls}\left(I_{s\alpha} - I_f\right) + \mu L_m \left(I_{s\alpha} + I_{r\alpha} - \frac{2}{3}\mu I_f\right) \tag{3.7}$$

$$\Psi_{fm} = \mu L_m \left(I_{s\alpha} + I_{r\alpha} - \frac{2}{3}\mu I_f\right) \tag{3.8}$$

Zero sequence components arise in the presence of an ITSC and they can be utilized as fault indicators [128]. Although zero-sequence components are also noted in the original formulation of [120], they are not included here for simplicity as they are control-wise ineffective for an IM with a floating neutral. The equivalent circuits for an IM with ITSC and the faulty turns are drawn in Fig. 3.4.

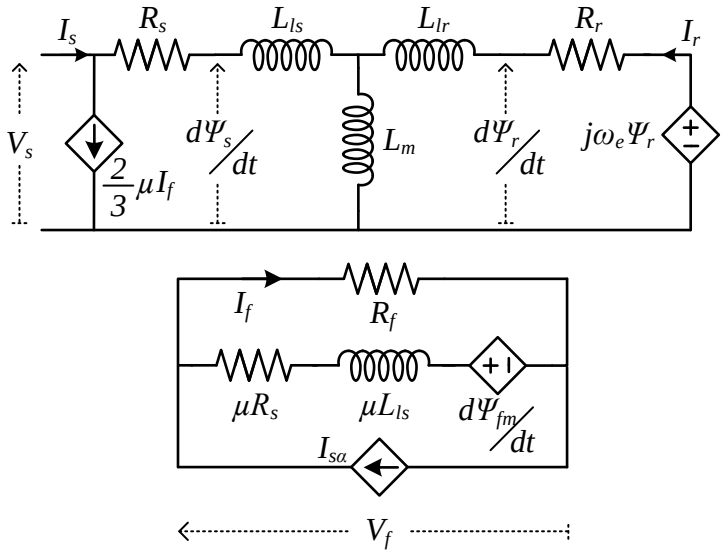

Figure 3.4. The equivalent circuits for the IM with an ITSC and the short-circuited turns.

The equations presented through (3.1)-(3.8) and the equivalent circuit depicted in Fig. 3.4 provide an analytical model of the IM with an ITSC fault. A linear distribution is assumed for the inductance of the shorted terms. Magnetic saturation of the core together with the toothing and slotting effects are neglected in the analytical model.

An analytical model that can represent IMs with ITSC faults, which is implemented in the Simulink environment, is previously reported in [129] but it has not been made available open-source so it could not be evaluated here. In the following, a new IM model that can simulate ITSC faults will be developed based on the voltage behind reactance (VBR) approach.

3.3.2 The "Voltage Behind Reactance" Representation for Induction Motor Modeling

Phases of an electrical machine can be represented as resistive and inductive (RL) branches connected in series with controlled voltage sources as depicted in Fig. 3.5. This type of representation is often called as "voltage behind reactance" (VBR) model and frequently reported in the literature [130]–[134]. Various VBR schemes are presented in [133] with a focus on computational efficiency. VBR based models, which include the effect of magnetic saturation, are developed in [130], [134] and they are also extended to the representation of multi-phase machines [131], [132], [134].

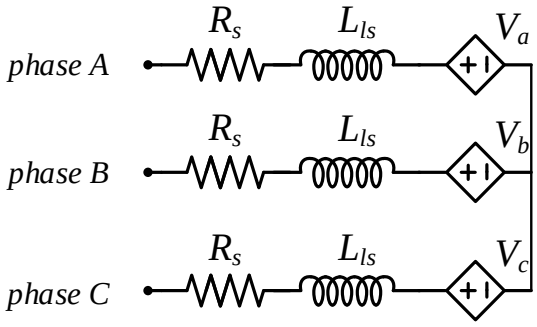

Figure 3.5. A generalized VBR representation of a three-phase electrical machine.

The VBR based models are convenient for circuit-based simulation packages and nodal analysis and may offer numerical efficiency [133], [135]. Modeling different multiphase machine connections and stator winding configurations are easier with VBR representation [134]. In this study, the VBR approach is utilized because it lends itself very suitable for the modeling of IMs with ITSC faults.

It is more intuitive to provide the VBR model of a normal (healthy) IM first, and then to modify it in order to model IMs with ITSC faults. The state-space model of the IM, which was discussed in detail in Chapter 2, is also provided herein (3.9)-(3.14), for the sake of completeness.

$$V_s = R_s I_s + \frac{d\Psi_s}{dt} \tag{3.9}$$

$$V_r = R_r I_r + \frac{d\Psi_r}{dt} - jw_e \Psi_r \tag{3.10}$$

$$\Psi_s = L_s I_s + L_m I_r \tag{3.11}$$

$$\Psi_r = L_m I_s + L_r I_r \tag{3.12}$$

$$\mathrm{T}_e = \frac{3}{2} p \mathcal{Im}(\Psi_s^* . I_s) = \frac{3}{2} p L_m \left(I_{s\beta} I_{r\alpha} - I_{s\alpha} I_{r\beta}\right) \tag{3.13}$$

$$J \frac{d\omega_m}{dt} = \mathrm{T}_e - \mathrm{T}_l \tag{3.14}$$

Examining the equivalent circuit depicted in Fig. 3.4, one can intuitively suggest that, once the voltage across the magnetizing inductance L_m is known (which will be denoted by V_m hereon), the IM can be modeled as R_s and L_{ls} in series with V_m, as shown in Fig. 3.5. The time derivatives of stator and rotor flux linkage terms (${}^{d\Psi_s}/_{dt}$, and ${}^{d\Psi_r}/_{dt}$, respectively) correspond to voltages that appear at the left and right side of V_m, as in Fig. 3. 4. Therefore, the voltage V_m can be derived from these two time derivatives of flux linkages, equations for which are provided in (3.15) and (3.16), by applying the principle of superposition. The resultant equation for V_m is as (3.187).

$$\frac{d\Psi_s}{dt} = V_s - R_s I_s \tag{3.15}$$

$$\frac{d\Psi_r}{dt} = R_r \frac{L_m}{L_r} I_s - \left(\frac{R_r}{L_r} - jw_e\right) \Psi_r \tag{3.16}$$

$$V_m = \left(\frac{d\Psi_s}{dt} L_{lr} + \frac{d\Psi_r}{dt} L_{ls}\right) \frac{L_m}{L_s L_r - L_m^2} \tag{3.17}$$

In a computer simulation environment such as Simulink, the expressions (3.15) and (3.16), which require only the circuit parameters of the machine and observable electrical quantities such as applied phase voltages and phase currents, can be integrated to yield Ψ_s and Ψ_r, respectively.

The resultant VBR scheme that can model an IM is represented with computation blocks in Fig. 3.6. The blocks are depicted with proper references to the equations that they implement.

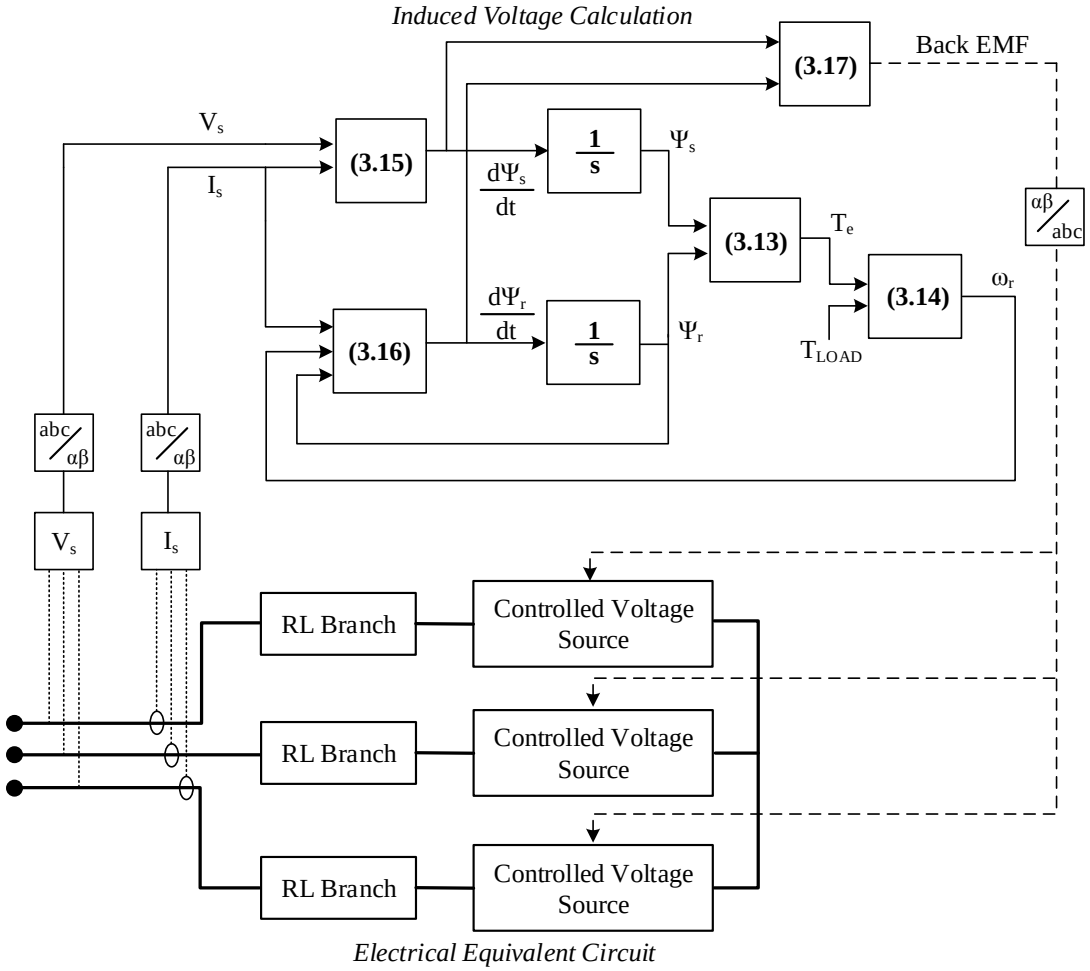

Figure 3.6. An equation-block representation of the VBR modeling of an IM.

A VBR-based model developed for the representation of the IM in Simulink environment is previously provided in [136] and made available through MATLAB Central, an open exchange platform for the community. The faulty IM model is developed through proper modifications of [136], as described in the following.

3.3.3 The Proposed Simulation Model

Once the VBR model of an IM is available, the influence of an ITSC can be modeled easily by rearranging the circuit elements as shown in Fig. 3.7. With the assumptions and notations described in Chapter 3.3.1, the fault is modeled with the fault resistance R_f, effective in parallel to faulty turns.

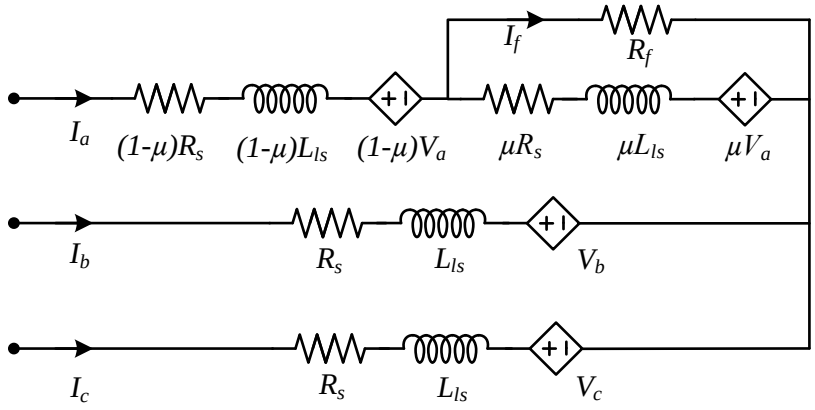

Figure 3.7. A generalized VBR representation of a three-phase electrical machine, with an ITSC fault.

In addition to the change in circuit configuration, in the modeling of the ITSC fault, it is important to consider the fault's influence by utilizing (3.18) and (3.19), instead of (3.15) and (3.16), which stand for the general (healthy) case. This can be easily accomplished by updating the current vector I_s, as shown in (3.20), such that the fault's influence (due to the fault current, I_f) is included in the current.

$$\frac{d\Psi_s}{dt} = V_s - \left(I_s - \frac{2}{3}\mu I_f\right) R_s \tag{3.18}$$

$$\frac{d\Psi_r}{dt} = R_r \frac{L_m}{L_r}\left(I_s - \frac{2}{3}\mu I_f\right) - \left(\frac{R_r}{L_r} - jw_e\right)\Psi_r \tag{3.19}$$

$$I_s' = I_s - \frac{2}{3}\mu I_f \tag{3.20}$$

The simulation model, which is intended for MATLAB-Simulink environment, has been made available as open-source at [61]. Once the simulation model is clicked, the machine parameters are set through a user interface, and the created model is run just like the standard IM model available in the Simulink library. Additional notes regarding the model are also provided in [15] and [137]. An inside view of the developed IM model is shown in Fig. 3.8.

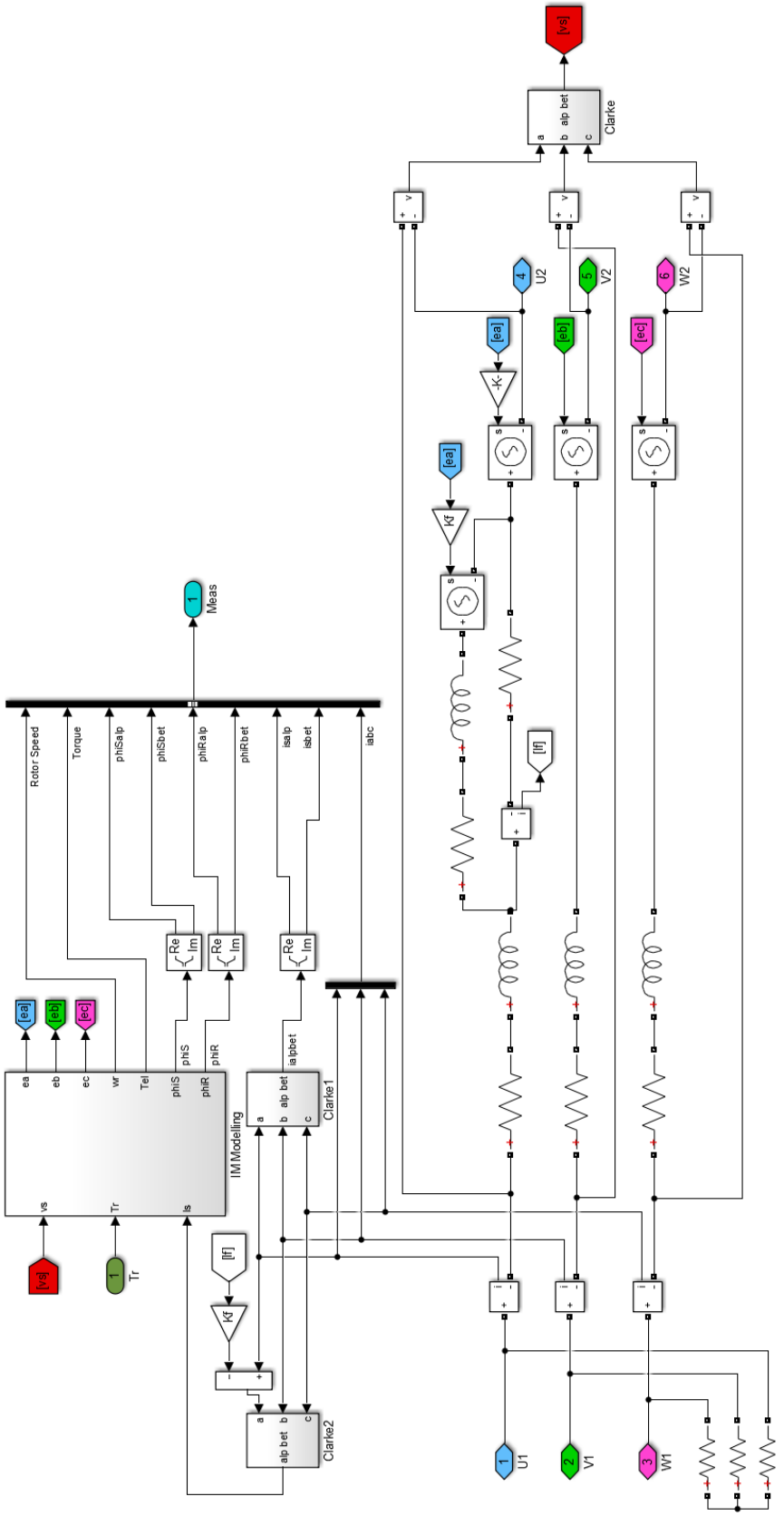

Figure 3.8. The inside view of the developed IM model.

To check the validity of the developed simulation model, it is at first run as a healthy IM and compared to the standard IM model from the Simulink library, being fed from the same AC source (150 V, 50 Hz), under the same mechanical load, as shown in Fig. 3.9. The IM models that are simulated and compared, reflect the simulations of the IM used in the laboratory implementation of MPC and described in detail in Chapter 2. For the simulation of the healthy mode in the developed model, entering zero value for the fault ratio yields simulation errors since Matlab does not allow circuit elements with zero values. Instead, a significantly small ratio for the faulted turns ratio and a large fault resistance value, such as $\mu = 0.0001$ and $R_f = 20\ k\Omega$, can be set to simulate the healthy operation mode.

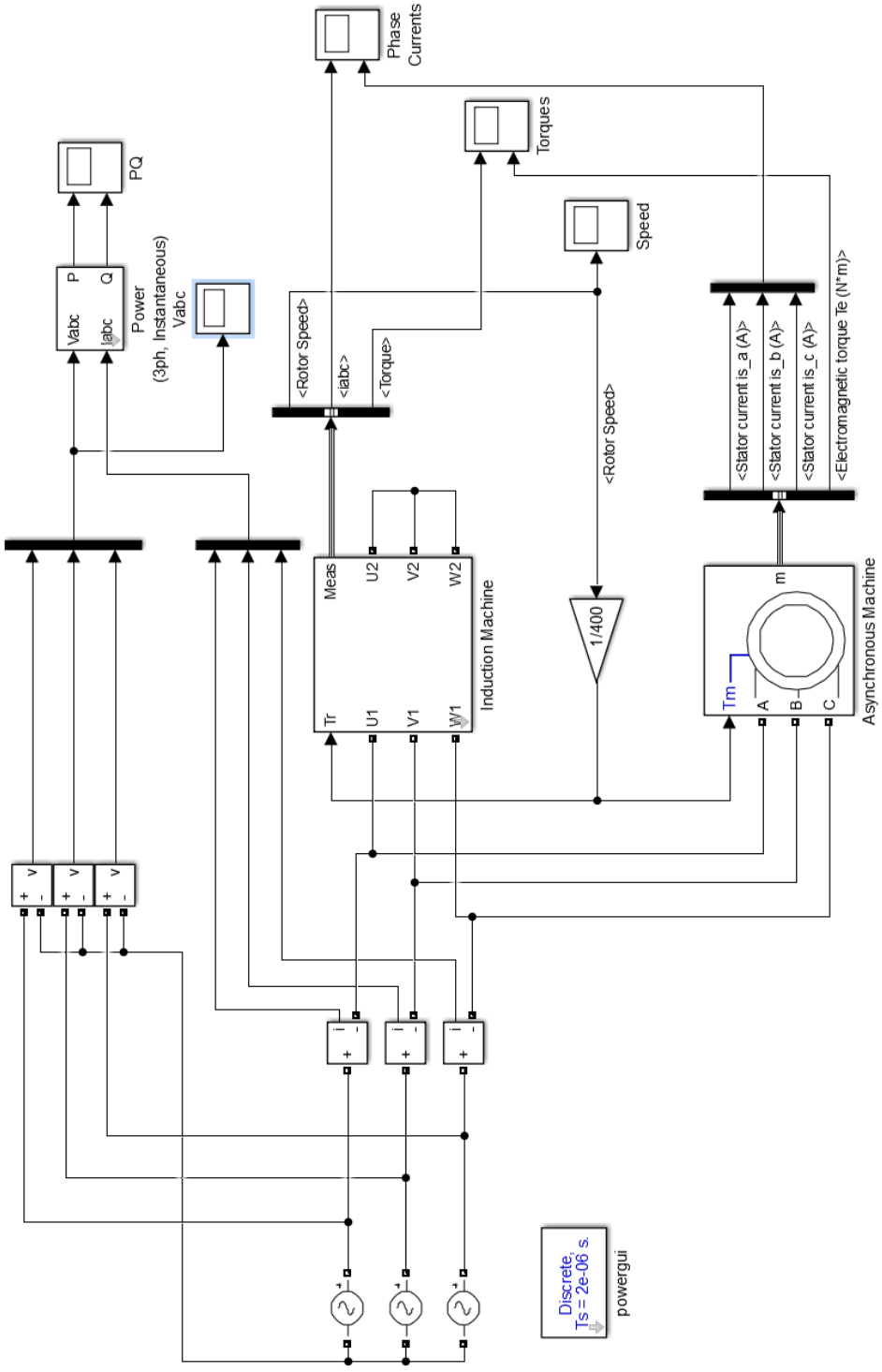

Figure 3.9. The simulation screen that includes the developed model, and the standard model, for comparison.

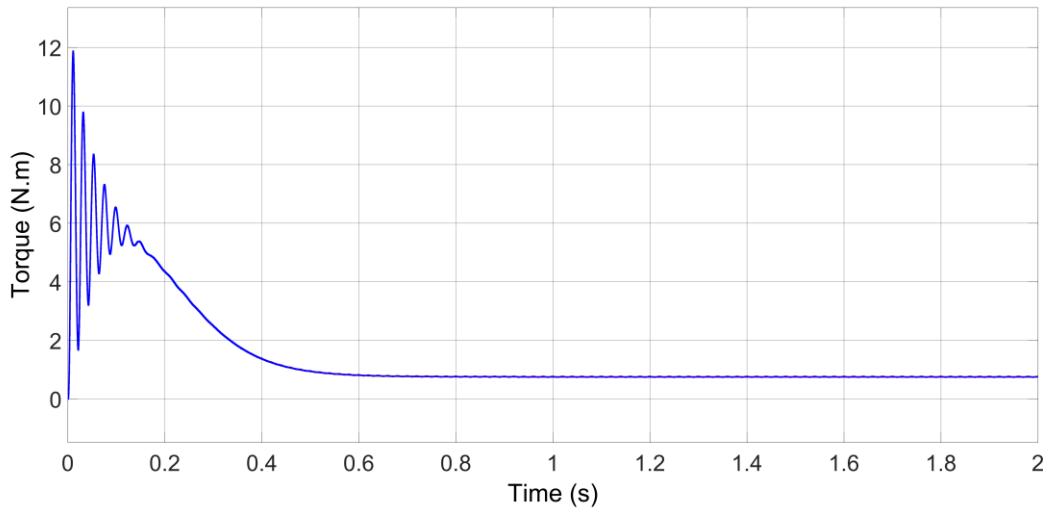

Figure 3.10. The electromagnetic torque waveforms for the healthy case, obtained from both the standard (blue) and the developed model (red).

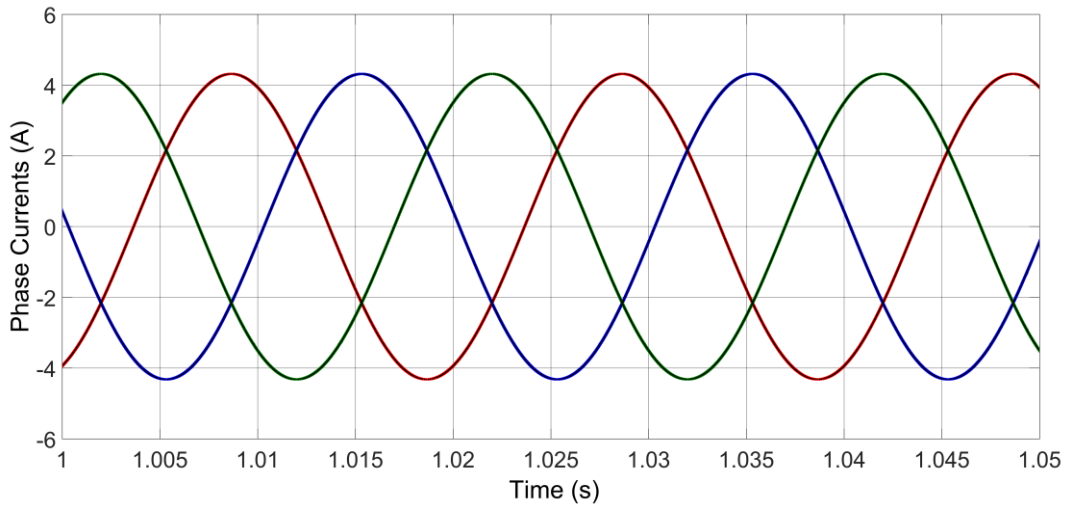

Figure 3.11. The steady-state phase current waveforms for the healthy case, obtained from both the standard (black, dashed lines) and the developed model (in red, blue, green).

Electromagnetic torque and phase currents waveforms are provided in Fig. 3.10 and Fig. 3.11 respectively. It can be concluded from the respective figures that both models produce the exact same waveforms which ensures that no significant modeling or computational error is present in the developed simulation model.

Having verified the proposed model through the comparison with the standard model for healthy mode, the next step is to model an ITSC fault. In the IM machine model, an ITSC of $\mu = 3\%$ along with a fault resistance of $R_f = 0.13\Omega$ is enabled. The torque and phase currents waveforms are depicted in Fig. 3.12 and Fig. 3.13 respectively.

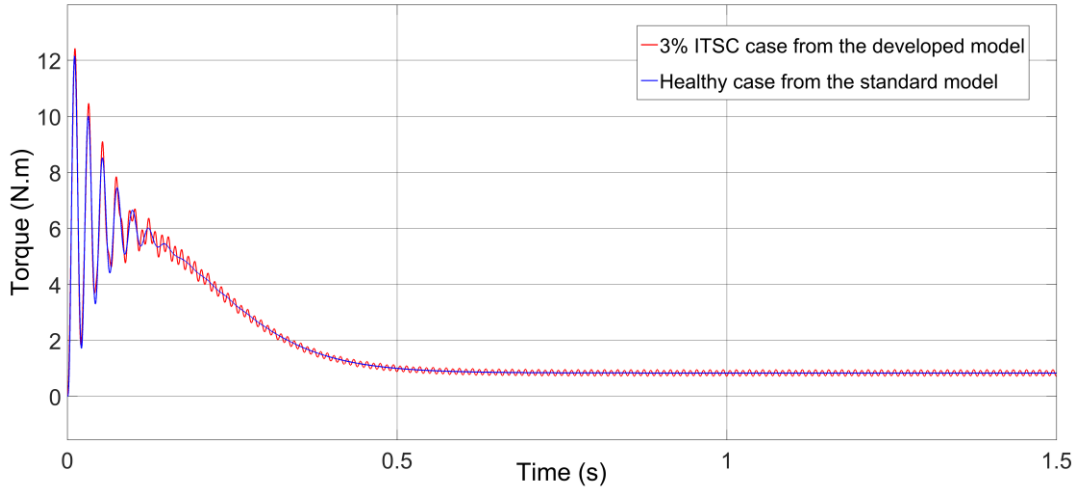

Figure 3.12. The electromagnetic torque waveforms for the 3% ITSC case from the developed model while the healthy case torque waveform from the standard model is kept as reference.

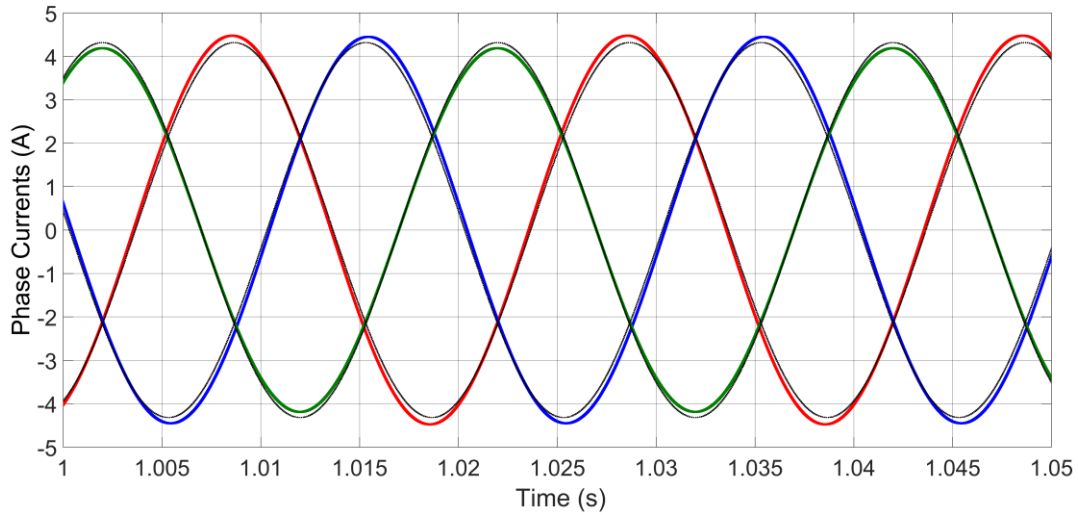

Figure 3.13. The phase current waveforms for the 3% ITSC case from the developed model while the healthy case currents (black, dashed) from the standard model are kept as reference.

Similar figures are repeated in Fig. 3.14 and Fig. 3.15 for an ITSC of $\mu = 5\%$. Waveforms of the healthy case (from the standard Simulink model) are kept in the respective figures in order to provide a visual comparison.

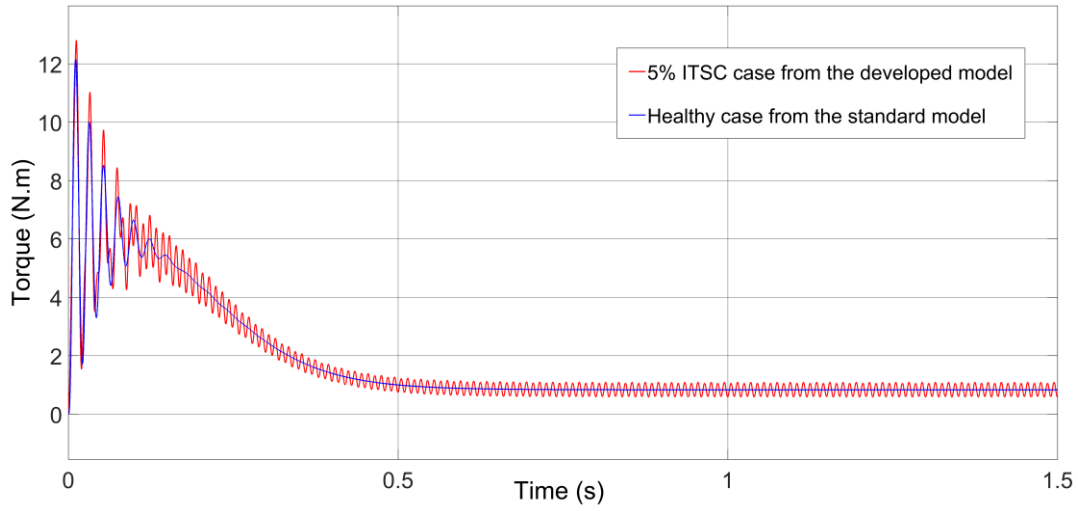

Figure 3.14. The electromagnetic torque waveforms for the 5% ITSC case from the developed model while the healthy case torque waveform from the standard model is kept as reference.

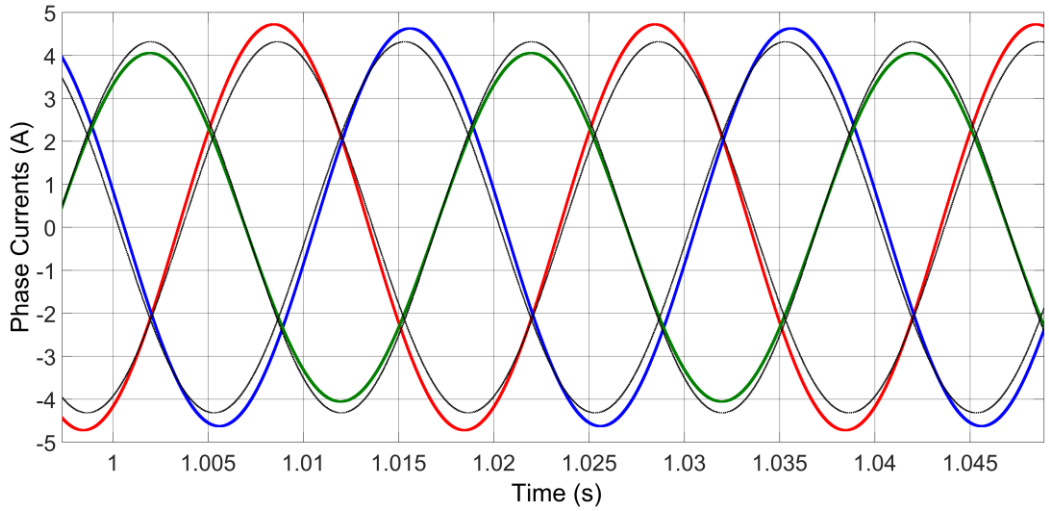

Figure 3.15. The phase current waveforms for the 5% ITSC case from the developed model while the healthy case currents (black, dashed) from the standard model are kept as reference.

From the waveforms depicted in Fig. 3.12 to Fig. 3.15, the influence of the ITSC fault on machine characteristics can be easily observed. The electromagnetic torque waveform exhibits an oscillation at twice the electrical frequency, which is a fundamental signature of ITSC fault occurrence [138]–[140]. Similarly, the current waveforms are no longer balanced; the faulty phase (the waveform in red), and the phase that follows (the waveform in blue), tend to draw larger current values where the phase after (the waveform in green) decreases in magnitude.

Another fundamental fault signature of an ITSC is the presence of second harmonic oscillations in the active and reactive power waveforms of an IM [138], [141], [142]. This property is also successfully reflected in the developed model. Active and reactive power waveforms are obtained for the 5-turn ITSC case and depicted in Fig. 3.16, where the second harmonic oscillations are evident as in the case of torque oscillations, as previously presented.

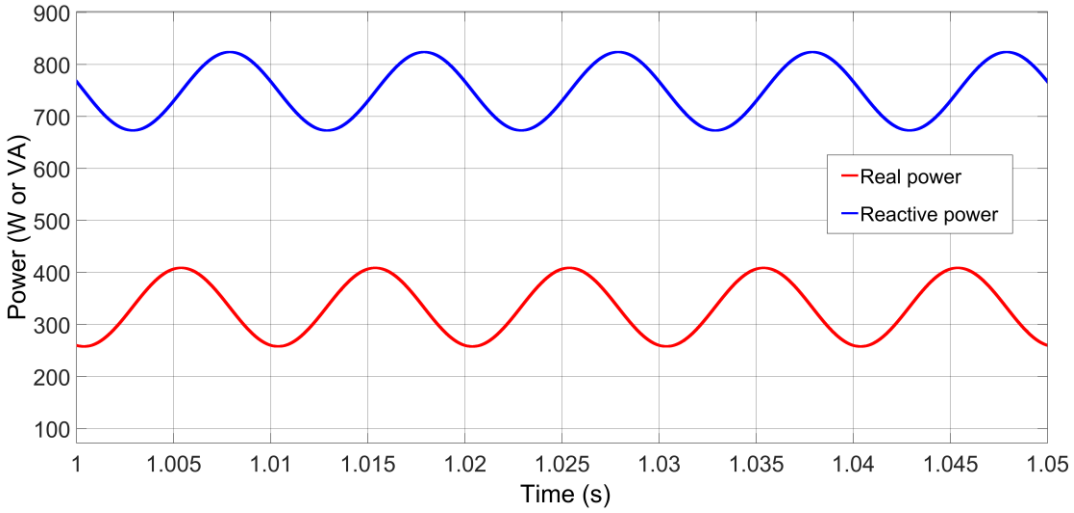

Figure 3.16. The active and reactive power waveforms that exhibit the 2nd harmonic component, for the 5% ITSC case.

3.4 Experimental Verification of the Proposed Model

The effectiveness of the developed Simulink model in simulating the IMs with ITSC faults is also verified through experimental results. The IM, on which the MPC has been applied in Chapter 2, was also utilized for fault diagnosis experimentation. Further details on the machine, regarding the modifications made for the analysis on ITSC influence, are provided in the following chapter.

The IM is fed from a fixed AC supply (150 V, 50 Hz) and the load torque is roughly 1 N.m. The phase currents of the IM for the case of a 3-turns and a 5-turns ITSC fault (out of 104 turns phase winding) are shown in Fig. 3.17, (b), and (c) respectively. The healthy mode phase current figures are also provided in Fig. 3.17 (a) for comparison. Similarly, for a closer examination on the impact of the ITSC fault on phase currents, current waveforms are provided phase by phase, with the healthy mode waveform is kept for reference, in Fig. 3.18, for an ITSC of 5-turns.

The phase, on which the ITSC has occurred, draws a larger current and leads in phase, as can be seen from Channel 1 of Fig. 3.17-3.18. The following phase's (Channel 2) current also increases, but not as much as that of the faulty phase and it is pretty much in phase. Finally, the remaining phase (Ch. 3) turns out to be the least affected one and it slightly decreases in magnitude and slightly leads its initial state.

a)

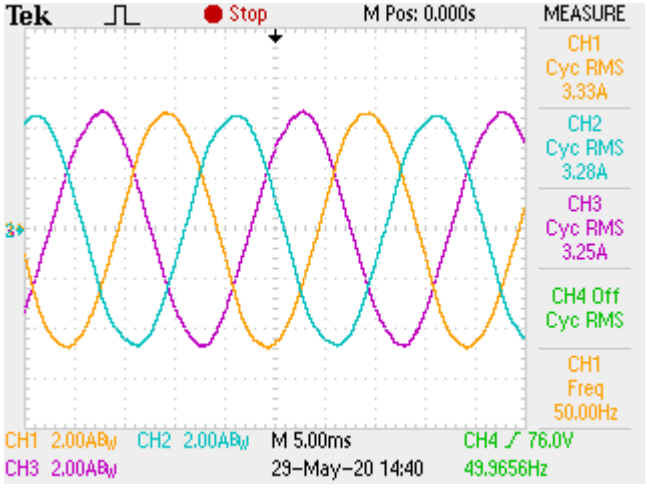

b)

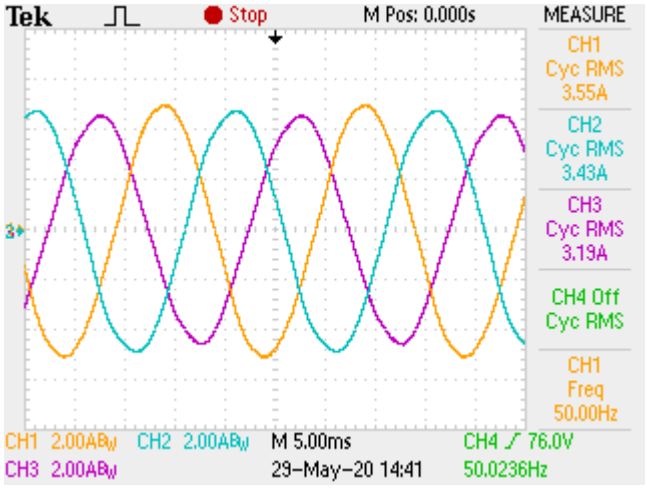

c)

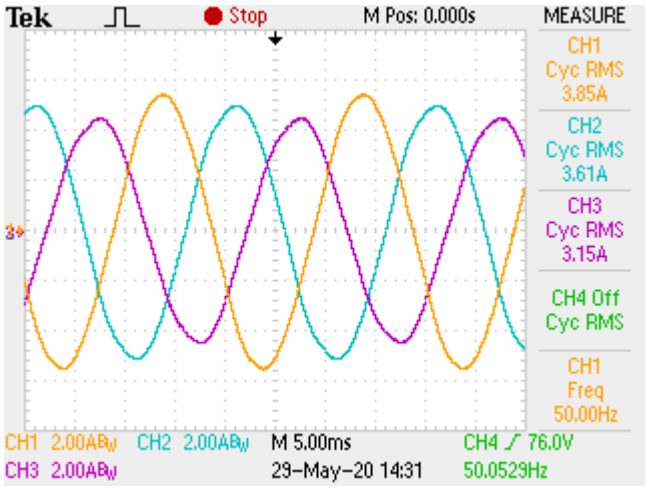

Figure 3.17. The phase current waveforms for the healthy case (a), and the ITSC cases of 3-turns (b), and 5-turns (c) ITSC fault on phase-A (Ch. 1).

a)

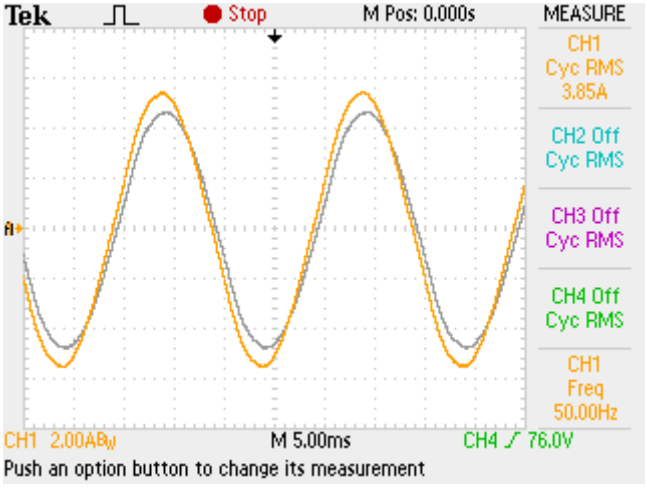

b)

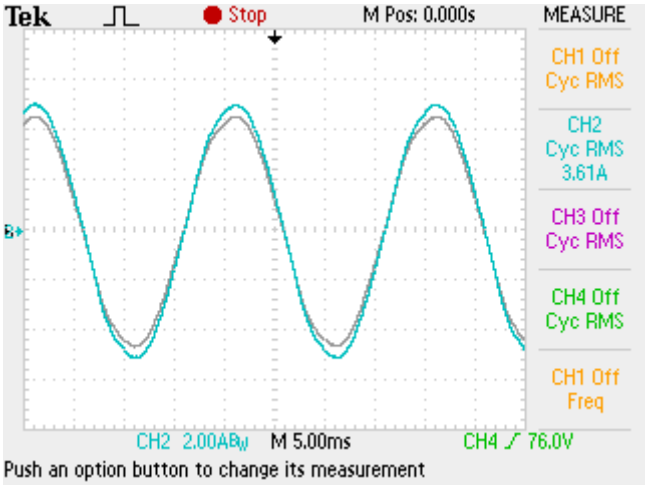

c)

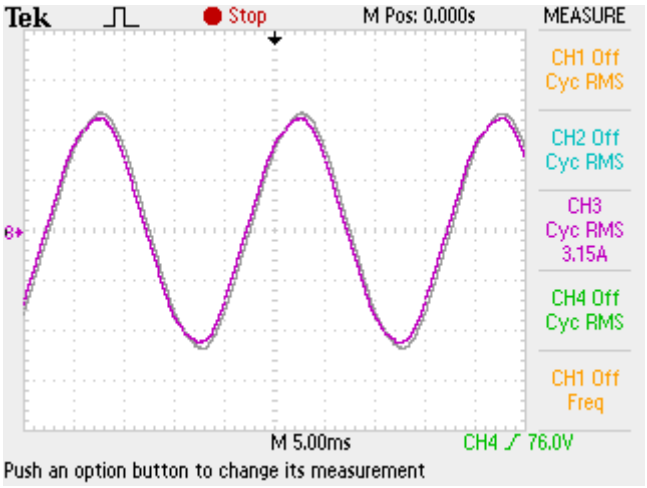

Figure 3.18. The phase current waveforms for the 5 turns ITSC fault on phase-A (Ch. 1), while the healthy case waveforms are kept for reference.

A comparison table which compares the percent changes in phase current magnitudes for the experimental and the simulation results is provided in Table 3.1. For each case, the healthy currents' magnitude is assumed as 1 per unit and the percent changes in magnitude are noted.

Table 3.1 The Comparison between Simulation and Experimental Results.

Case	*Phase A current*	*Phase B current*	*Phase C current*
3% ITSC - Experimental	+7.9%	+4.3%	-3%
5% ITSC - Experimental	+17%	+9.7%	-4.3%
3% ITSC - Simulation	+3.7%	+3%	-3%
5% ITSC - Simulation	+9.3%	+7.2%	-6%

The proposed simulation model is successfully depicting the general pattern of fault's influence on phase current waveforms, which proves its effectiveness. However, the increases in magnitude of current waveforms are under-predicted by the developed model. For example, under the 5-turns ITSC fault case, the current magnitude in the faulted phase increases 17% with respect to the healthy operation but the simulation model shows a 9.3% increase. Similarly, Phase C current magnitude's change is slightly over-predicted. The fundamental reason for this is anticipated as the neglection of the magnetic saturation effect in the core, which becomes critical as a very large amount of fault current is flowing in the case of an ITSC. Besides, the machine's winding geometry and thermal effects are not modelled in the proposed model, and the practical assumption of linear distribution for faulty turns' leakage inductance may not be quite accurate depending on the core and winding structure.

It is obvious that, for a precise simulation of an IM with ITSC fault, a complete model including detailed machine geometry and material characteristics, such as magnetic saturation, is required. Therefore, the proposed simulation model cannot

be expected to perform equally well compared with a detailed FEA simulation. Nonetheless, the proposed model is simple and convenient to use and it can successfully predict and display the nature of influence from an inflicting ITSC fault on machine performance and the related electrical quantities, such as phase currents.

3.5 Conclusion

According to the author's best knowledge, no simple simulation model was available to simulate the IM with an ITSC fault on one of its phases. The fundamental motivation of this chapter is to fill this gap. First, an overview of existing literature on machine faults is presented. Then, the mathematical model of the IM with an ITSC fault is given. Utilizing the VBR approach, a new model that can simulate ITSC faults in IMs is developed. Both experimental and simulation studies are conducted for the verification of the proposed model. As previously discussed, the complete characterization of an ITSC fault would require the full consideration of machine and winding geometry, with the electromagnetic properties of the core material included. However, the simplified analytical model described in this chapter is quite effective in modeling the IM with an ITSC fault, as the experimental results suggest. The developed VBR-based analytical simulation model, which has been made available as open-source at [61], can help researchers with their simulations regarding inter-turn short circuit faults in IMs.

CHAPTER 4

A NOVEL METHOD FOR INTER-TURN SHORT CIRCUIT FAULT DETECTION FROM FCS-MPC VECTORS

4.1 Introduction

In this chapter, a novel and non-invasive ITSC online detection method is presented for an IM, driven by a 2L-VSI, via FCS-MPC. Fault diagnosis for the closed-loop controlled drives is considered first. Based on the observations made for the ITSC fault in a closed-loop controlled drive, a new method for ITSC fault detection is developed. Then, experimental fault detection performance figures and some further discussion on the proposed method are provided. Finally, the fault detection performance of the proposed method is benchmarked with respect to the existing studies from the literature.

The primary contribution detailed in this chapter is the novel algorithm that is developed to detect stator ITSC faults, including the fault location, for an IM driven by FCS-MPC. The proposed algorithm works as a simple add-on to the standard FCS-MPC structure. The basic principle adopted for fault detection is as follows: a healthy IM (without any fault) is expected to be a balanced system. Therefore, one may anticipate that the voltage vectors, which are commanded by the controller, would most likely exhibit a balanced distribution, for a closed-loop motor drive. An ITSC would disrupt to this balanced system; hence, any unexpected deviations in the voltage vectors' distribution would indicate the presence of an ITSC. This approach for fault detection is surely a general one, and it can be extended to other closed-loop control strategies. However, implementing a fault detection algorithm based on inverter switching statistics is way more suitable for FCS-MPC. As the FCS-MPC routine applies discrete voltage vectors as its outputs (rather than voltage signals that are to be modulated) it becomes an easy task to record and evaluate switching vectors

against any unexpected deviation. Of course no practical machine or motor drive system (with its inverter, cabling, etc.) can be perfectly symmetrical. Furthermore, there exists the influence of noise on the controller action. Hence, a perfectly equal distribution among the voltage vectors cannot be expected from even a healthy machine. Nonetheless, variations among the voltage vectors for a healthy IM are observed to be far less than those of an IM with an ITSC, which is be verified by the experimental results.

4.2 ITSC Fault Diagnosis in Closed-Loop Controlled Machines

In the last few decades, electric drives have grown both in numbers and complexity, mainly due to the advances in microprocessor and power semiconductor technologies. A similar trend can be observed for fault diagnosis research: while most of the early works in condition monitoring research concentrate on the fault signatures of line-fed motors, fault diagnosis for inverter-fed, closed-loop controlled drives is gaining more attention for the recent studies [143]–[153]. In the following, a review of the stator short circuit detection schemes intended for closed-loop controlled drives is presented. Then, the influence of an ITSC fault for controlled and uncontrolled cases are examined and compared.

4.2.1 A Review of Stator Short-Circuit Detection Schemes for Closed-Loop Controlled Drives

An effective motor drive controller inherently tries to create a balanced set of phase currents even in the case of an inflicting fault, therefore condition monitoring for closed-loop controlled drive systems becomes especially interesting [143], [144], [146]. This in turn also suggests that fault traces (such as phase current unbalance) can be covered to a large extent, for closed-loop controlled drives. Hence, for a closed-loop motor drive system, it is best to assess any fault detection algorithm in conjunction with the main motor control technique. Among the existing studies cited

as examples of fault detection with closed-loop control, field-oriented control (FOC) is considered in [143], [144], [146]–[152], and direct torque control (DTC) in [145], [153].

A fault detection method that functions along with MPC has been recently published [154], where a PMSM is driven via FCS-MPC, with a predictive current control approach. The main idea in [154] is to run wavelet analysis on the cost function and to spot the unexpected components for fault detection. Cost function and fault's interaction is examined within this study too, and further discussions are provided in the following parts.

Reference [143] is a very early example that presents the impact of control on faulted IM behavior. In the case of stator and rotor faults, harmonic components at $2f$ and $2sf$ are observed in the I_d spectrum, respectively. The harmonic components were found to be quite independent of control parameters and dependent on fault severity. Observing the unexpected components at the frequency spectrum of motor electrical quantities (motor currents or voltages) or control parameters (e.g., e_d, e_q) has been a fundamental method for fault detection. Spotting an unexpected frequency component, which would diminish for a healthy machine, implies the presence of a fault. Among the references cited thus far, [143], [144], [146], [147], [150]–[152] employ frequency-domain analysis based fault detection approaches.

The influence of closed-loop control on an IPMSM with an ITSC is studied in [155], where FOC is compared with the open-loop operation via a six-step voltage waveform. It is observed that FOC performs with lower losses and vibration and is capable of compensating for the disturbances created by the ITSC.

ITSC fault detection through the observation of PWM current ripples is proposed in [149]. The faulty phase will exhibit a lower impedance hence an unexpected increase in the ripple content of a phase current can be utilized as an ITSC indicator. 2-turn faults (out of a total of 62 turns in a phase) could be detected for a 5-phase PMSM drive with FOC. Similarly, the high-frequency impedance is observed and used to spot ITSC fault in [156], for a multi-phase IPMSM. These two approaches require

additional filter circuitry though. Another impedance-based ITSC detection scheme is reported in [146] for parallel operated IMs. No extra filter circuit is utilized, but the phase voltages are sensed.

A fault detection scheme that is capable of identifying both ITSC and demagnetization faults is proposed in [157], for and IPMSM with FOC. The diagnosis is made with the deviation of the torque angle, which is defined as in (4.1). ITSC is diagnosed for $\delta < \delta_h$ and magnet demagnetization fault is diagnosed for $\delta > \delta_h$, where δ_h is the expected torque angle for healthy operation. The method requires training.

$$\delta = -\tan^{-1}(\frac{V_d}{V_q}) \tag{4.1}$$

A model-based ITSC detection method is presented in [158] for a PMSM. The fault detection method is based on the "residual current vector" that is generated by the difference between the estimated and measured stator currents. The proposed method is verified for a wide operating range of the motor and even under dynamic operating conditions. No details regarding the controller are provided, though.

Utilizing inverter switching statistics as a means of fault detection is previously proposed in [148]. Although the basic principle utilized for fault detection is the same in this study, the proposed fault detection method has several differences regarding both the motor control strategy and the figures that indicate fault existence. An additional predictive current control (PCC) routine is implemented alongside FOC in [148], without a detailed description of the applied control scheme. The method to interpret the switching vector distribution is also different. Moreover, the influence of FCS-MPC related parameters, such as the weighting factor (λ) and the sampling frequency, on the fault detection performance is documented in this chapter.

Another study that implicitly utilizes the loss of symmetry due to the ITSC fault is [159]. The unexpected power unbalance between the phases of an electric motor is observed in [159], in order to spot an ITSC fault.

This section aims to provide a review of sufficient depth in the existing literature regarding the ITSC fault detection methods proposed for closed-loop controlled motor drives. The references cited here will be revisited in Chapter 4.3.4**,** in which a benchmarking study for the proposed fault detection method is presented.

4.2.2 An Experimental Analysis on the ITSC Faults under Closed-Loop Control

In order to investigate the influence of closed-loop control on fault signatures that arise in the presence of an ITSC, an experimental procedure is followed. The IM, which was utilized in the MPC implementation and described in Chapter 2, is also used for the closed-loop vs open-loop fault tests. Its stator winding is custom modified as shown in Fig. 4.1, such that intentional ITSC faults can be created over two, three, and five turns, from the extra connections made available (A1, A2, and A3 in Fig. 4.1). No extra resistor is utilized in ITSC tests to resemble an additional fault resistance. However, ITSCs are created over a 2-meter long cable that introduces an extra resistance of approximately 0.13 Ω.

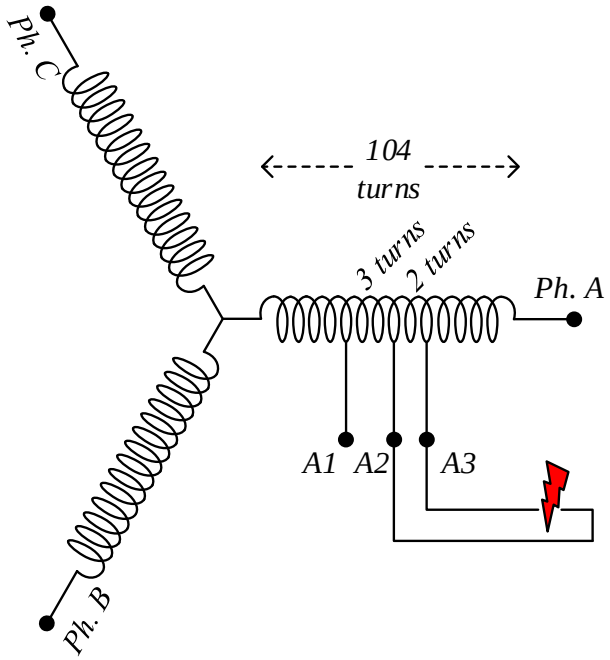

Figure 4.1. A representation for the modified winding diagram of the IM, that allows intentional ITSC creation.

The laboratory setup used in the experimental studies was described in the previous chapter and will not be revisited here. Nonetheless, the functional structure of the experimental setup is provided in Fig. 4.2., for the sake of completeness.

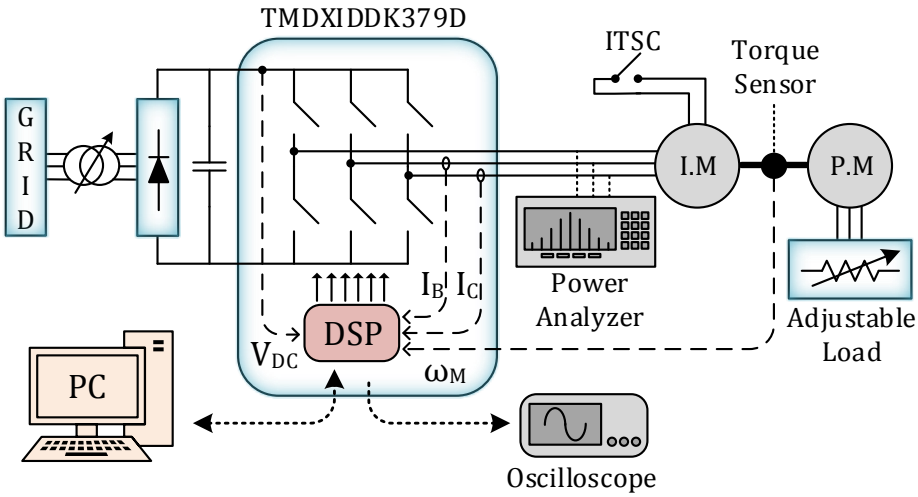

Figure 4.2. Functional structure diagram for the experimental setup used in the ITSC fault analyses.

To exhibit the influence of control during an ITSC situation, the motor is driven both via the closed-loop predictive torque control (as described in Chapter 2) and fed through a fixed AC supply that resembles the rated values (150 V, 50 Hz, 1 N.m load torque). An intentional ITSC fault is created as the short-circuiting of 3-turns at the phase-A winding. The three-phase stator current waveforms for both cases, plus the fault current, are shown in Fig. 4.3. For the inverter-driven cases (Fig. 4.3. c, d), the acquisition mode of the oscilloscope is set to the average of four samples. It can be observed that the faulty phase tends to draw more current, which can lead up to a 10% difference in magnitudes (between Ch1 and Ch3, in Fig. 4.3 a, b), consequently making an unbalanced set of three-phase currents. Whereas, the stator current waveforms for the MPC-controlled, inverter-driven case are almost insensitive to the ITSC, because the predictive controller still manages to create a balanced set of three-phase currents even under the influence of the fault, as shown in Fig. 4.3. c, d.

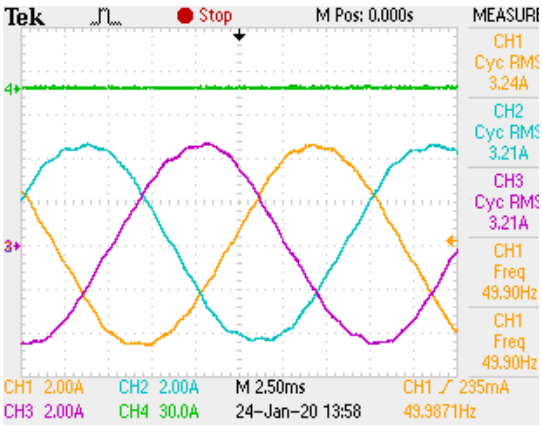

a) Line-fed, no fault.

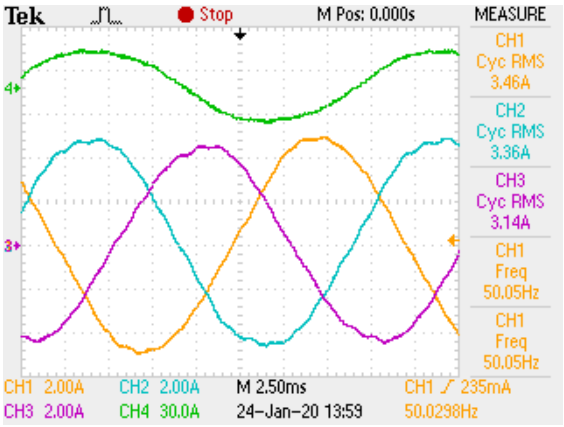

b) Line-fed, ITSC fault of 3 turns.

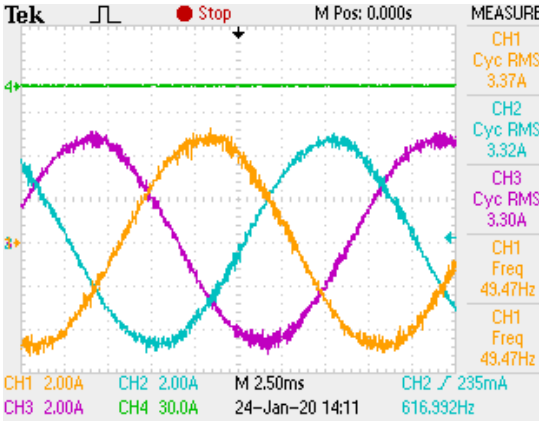

c) Closed-loop control, no fault.

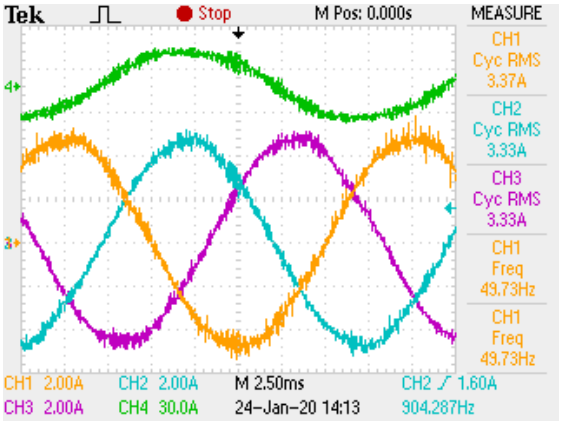

d) Closed-loop control, ITSC fault of 3 turns.

Figure 4.3. Stator phase currents (Ch.1-2-3) and the ITSC current (Ch. 4) for the cases; open-loop without fault (a), open-loop with a fault (b), closed-loop without fault (c), closed-loop with a fault (d), under the operating conditions $f_e = 50, T_e = 1\ \mathrm{N.m}$.

In the frequency domain analysis of the current waveforms, no additional fault-related harmonic components are observed. Similarly, the machine torque waveform does not exhibit any observable ripple or oscillation for the experimented conditions. From the waveform analyzer connected to IM terminals, as shown in Fig. 4.2, it is observed that the line to neutral voltage of the faulty phase turns out to be approximately 1V smaller than the other phases' voltages for the closed-loop controlled case. This is the fundamental reason for the faulty phase current not increasing, contrary to the open-loop operation. We draw two important conclusions from the preceding analysis, as follows:

- An effective closed-loop control can render waveform analysis based fault detection techniques less viable, because the fault signatures are significantly covered or suppressed.

- A controller is expected to apply a balanced set of inverter switching vectors, to create a balanced set of stator currents, for a normal (healthy) operation. However, for an IM with an ITSC fault on one phase, motor phases are no more identical. Therefore, it is intuitive to suggest that the controller would apply an unbalanced set of inverter switching vectors to yield a balanced set of stator currents, for a faulty machine.

Given the two conclusions stated above, the main idea adopted for fault detection in this study is to investigate the controller outputs against any abnormal distribution. As previously noted, the adoption of inverter switching statistics as a means for fault detection is previously reported in [148], where the motor is driven via FOC that is accompanied by a PCC scheme. In the spatial distribution of the weighted mean values of the inverter switching vectors, two distinctive minima at 60° and 240° are reported as an indicator of an ITSC. In the experimental verification of the proposed ITSC detection algorithm, which is described in the following section, in addition to the decrease reported in [148], an increased in the switching vectors that correspond to the faulty phase (e.g., v_1 and v_4 for a fault in phase-A) is observed. Considering that we already observed that the faulty phase's voltage is slightly decreased in case

of an ITSC fault, this seems as a contradiction unless the utilization of zero-vectors is also considered. Furthermore, it is reasonable to consider also that the flux producing capacity of the voltage vector, as formulated in (2.16), that corresponds to the faulty phase is now crippled due to fault, because there exists a parallel resistive path in the winding, as shown in Fig. 3.3, which does not produce flux.

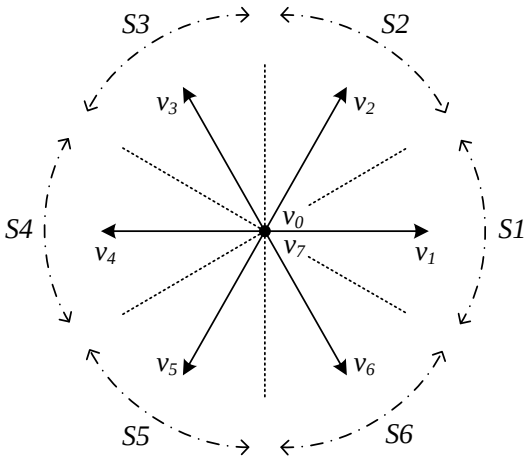

Figure 4.4. Voltage vectors of a 2L-VSI, with sector definitions adapted from [4].

In the attempt of examining ITSC fault's influence on the controller outputs, the inverter switching vectors' count are averaged and recorded for 10 full electrical periods. The records also include the sector information S, which the stator flux vector Ψ_s occupies, with the sector definitions adapted from the classical DTC approach [4]. Table 4.1 shows how many times each vector is applied for the recording time of 10 full electrical periods. The switching data was recorded for the operating condition at rated speed (3000 rpm), rated torque (approximately 1.25 N.m). It should be noted that it is practically not quite possible to observe and record FCS-MPC outputs with perfect precision due to the following reasons:

- The full rotations and sector information ($S_1, S_2, \cdots, S_6$) are decided based on Ψ_s, which is merely an estimated control variable that is prone to noise and ripple.
- Even under steady-state conditions, vector counts do not turn out to be purely constant, they fluctuate to a considerable extent.

- The overall effect of system non-idealities, sensor noises, and discretization errors influences the controller behavior.
- Experimenting with an ITSC fault results in a quick increase in machine temperature. Hence, the winding temperature during the record cannot be held constant, which may implicitly affect switching counts.

Therefore, the switching vector statistics depicted in Table 4.1 should be regarded as a general observation that tries to picture the fault's influence, rather than absolute numbers that are expected to be reproducible with perfect precision.

From Table 4.1, it can be observed that, the utilization of switching vectors that correspond to the faulty phase increase (v_4 during sector 3 and v_1 during sector 6) along with the utilization of zero-vectors also increasing. Consequently, the percent shares of other vectors decrease and the magnitude of the faulty phase's voltage is not increased due to the increase in zero-vectors. The changes in active vector allocations can be quantified with an expression as shown in (4.2).

$$\Delta v_x = \left(\frac{v_x - v_{avg}}{v_{avg}}\right)_{faulty} - \left(\frac{v_x - v_{avg}}{v_{avg}}\right)_{healthy} \tag{4.2}$$

By using (4.2), the approximated percent changes in active vectors due to the inflicting 2-turns ITSC fault were found as follows:

$$(\Delta v_1 + \Delta v_4) \cong 12\%, (\Delta v_2 + \Delta v_5) \cong -9\%, (\Delta v_3 + \Delta v_6) \cong -3\%$$

Table 4.1 Switching vectors' count for the healthy and faulty cases.

Healthy Mode

	S_1	S_2	S_3	S_4	S_5	S_6	Total	Δ (%)
v_0	252	240	252	240	243	242	1469	N.A
v_1	151	0	0	88	430	489	1158	1.7
v_2	476	142	0	0	89	428	1135	-0.3
v_3	410	498	142	0	0	88	1138	0.0
v_4	85	418	474	140	0	0	1117	-1.9
v_5	0	92	440	497	147	0	1176	3.3
v_6	0	0	83	413	476	134	1106	-2.8
Total	1374	1390	1391	1378	1385	1381		

2-Turns ITSC

	S_1	S_2	S_3	S_4	S_5	S_6	Total	Δ (%)	Offset Removed
v_0	223	240	268	215	241	267	1454	N.A	N.A
v_1	173	0	0	87	448	527	1235	8.6	**6.8**
v_2	461	156	0	0	76	384	1077	-5.3	-5.0
v_3	432	478	128	0	0	94	1132	-0.5	-0.5
v_4	84	432	495	167	0	0	1178	3.6	**5.4**
v_5	0	77	405	477	168	0	1127	-0.9	-4.2
v_6	0	0	87	425	455	109	1076	-5.4	-2.6
Total	1373	1383	1383	1371	1388	1381			

The figures depicted on Table 4.1 are program variables that were visually observed and approximated over the Code Composer Studio (CCS) interface. In the later stages of the experimental studies, a better option was enabled: during steady-state operation for both healthy and faulty modes, the MPC output vectors ($v_0, v_{1,} \dots, v_6$) are recorded to an array of 22000 elements. This was made possible by re-allocating unused ram sectors for the program. By doing so, grasping a picture of FCS-MPC in operation was made possible. The predictive controller's operation is depicted in Fig. 4.5 by displaying the applied vectors for approximately 4 electrical cycles, for the operating conditions of 1.35 N.m. load torque at 3000 rpm, with $|\Psi_s|^{ref}$= 0.3 Wb, under a DC-bus voltage of 350 V. It is very insightful to notice how the controller switches through active vectors ($v_1, v_{2,} \cdots, v_6$), with the zero-vectors are interspersed all along, during the electrical periods.

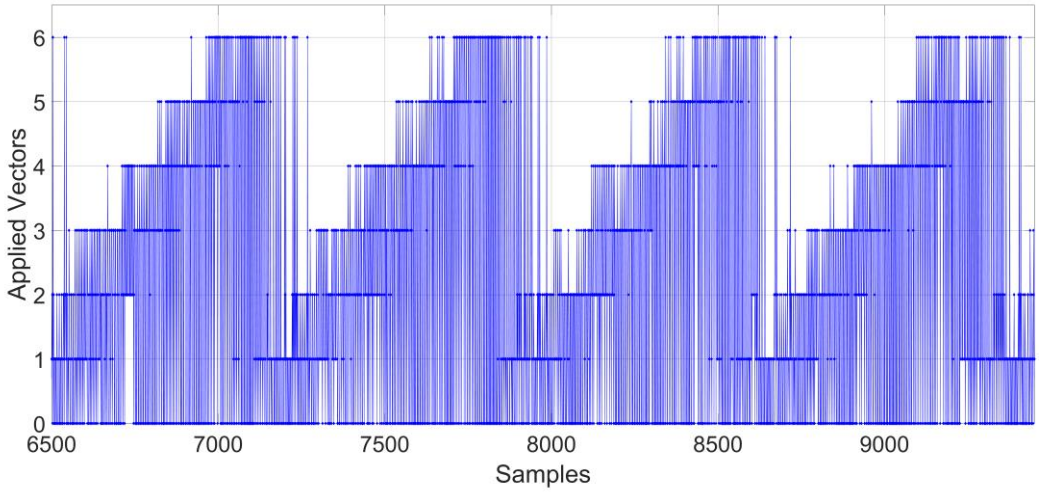

Figure 4.5. A display of MPC operation for 1.35 N.m. load torque at 3000 rpm.

The vectors recorded for 22000 samples were later cropped down such that full electrical periods are covered in the respective series so that inverter switching statistics can be run. The results are depicted in Table 4.2 for two cases of healthy operation and another two cases of operation with an ITSC fault of 2-turns. Table 4.2 clearly illustrates the change in active vector allocation with respect to an inflicting ITSC fault. The records are available at [61].

Table 4.2 Switching vectors' count for the healthy and faulty cases.

	Faulty Record #1	Faulty Record #2	Healthy Record #1	Healthy Record #2
Total Samples	21016	20228	21616	21744
Total Periods	29	28	30	30
v_1 Count	2726	2669	2366	2386
v_2 Count	2247	2194	2442	2469
v_3 Count	2222	2167	2298	2344
v_4 Count	2752	2658	2545	2545
v_5 Count	2202	2230	2319	2319
v_6 Count	2268	2141	2427	2507
$\Delta(\%)\ v_1$	13.4	13.9	-1.4	-1.7
$\Delta(\%)\ v_2$	-6.5	-6.4	1.8	1.7
$\Delta(\%)\ v_3$	-7.5	-7.5	-4.2	-3.5
$\Delta(\%)\ v_4$	14.5	13.4	6.1	4.8
$\Delta(\%)\ v_5$	-8.4	-4.8	-3.4	-4.5
$\Delta(\%)\ v_6$	-5.6	-8.6	1.1	3.2
Phase A $\Delta(\%)$	14	13.7	2.3	1.5
Phase B $\Delta(\%)$	-6.6	-8.1	-1.5	-0.1
Phase C $\Delta(\%)$	-7.4	-5.6	-0.8	-1.4

Based on the observations documented thus far, two approaches can be proposed as potential method to spot an ITSC fault through an analysis of controller outputs, i.e. inverter switching vectors:

- Examination of the unbalance in the allocation of active vectors for full electrical periods.
- Examination of the unbalance in the zero-vector allocation across the sectors of the complex plane.

ITSC fault detection has been accomplished with both of these method. However, the examination of unbalance in the active vectors was found to yield more distinctive results for fault detection, compared to the zero-vector allocation approach. Therefore, the main fault detection strategy that will be proposed in this thesis, is based on active vector allocation and will be described in detail in the following parts.

4.3 A Novel MPC-Based ITSC Detection Method

In the following, a novel, MPC-based ITSC detection method is proposed. The proposed method is first described in detail, then the experimental results, which prove the effectiveness of the method, are presented. Finally, several aspects regarding the proposed method are discussed.

4.3.1 The Algorithm of the Proposed Method

In view of the observations documented for the closed-loop control of an IM with an ITSC fault, an ITSC detection algorithm is developed based on spotting an unusual unbalance in the distribution of the active vector allocation. A flowchart diagram for the developed fault detection strategy is shown in Fig. 4.6. The number of how many times each active vector is applied by the inverter is found with a counter. The counting routine is done for a preset number of full electrical periods, (i.e., as long

as ‘Counter Flag’ in Fig. 4.5 is true), which can be determined by the full rotations of the estimated stator flux (Ψ_s) vector. Once the counting process is complete, the average value of the active vector switching numbers and the percent deviation of each vector with respect to the average are calculated. Considering the influence of system non-idealities and noise on the controller action, the deviation results are then low-pass filtered.

Even for a healthy machine, there may be deviations in the utilization percentages for the active vectors as a perfect symmetry is seldom for a practical motor drive system. The healthy case unbalance figures can be observed from Table 4.2, which are sufficiently smaller compared to the deviations that stem from an ITSC fault. For an improved fault detection performance, the deviations in the normal operation (healthy case) are recorded as offset values and subtracted from the low-pass filter outputs. The filtered and offset-removed values of deviations are evaluated on a phase-basis, and the final result is named as the ‘fault indicating score’, which will be abbreviated as ‘FIS’ hereon. Although already shown in Fig. 4.6, the formula that yields the FIS is stated again in (4.3). The final FIS magnitude is compared to a preset threshold and the ultimate faulty/healthy decision is made based on this comparison.

$$FIS = \left(\Delta v_{1,\%} + \Delta v_{4,\%}\right)^2 + \left(\Delta v_{2,\%} + \Delta v_{5,\%}\right)^2 + \left(\Delta v_{3,\%} + \Delta v_{6,\%}\right)^2 \qquad (4.3)$$

The flowchart depicted in Fig. 4.6 resembles a simple algorithm that is easy to program, and runs without a significant burden to the processor. Further details on these will be provided after a comprehensive analysis on the experimental implementation results of the proposed fault detection method.

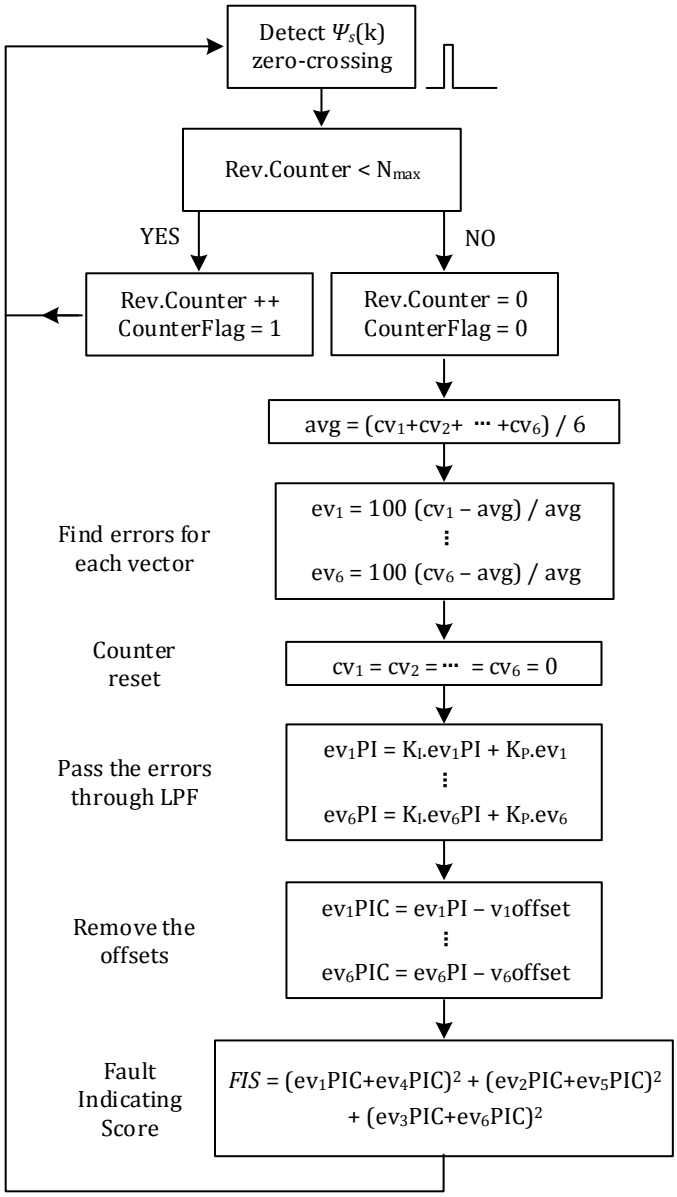

Figure 4.6. Flowchart diagram for the proposed ITSC fault detection algorithm.

4.3.2 Experimental Results for the Fault Detection Performance

The fault detection performance of the proposed algorithm is given in Fig. 4.7 and 4.8, for several torque-speed values, for the ITSC faults of 2-turns (Fig. 4.7) and 3-turns (Fig. 4.8). The 'fault indicating score' (FIS) waveform (green) exhibits a decisive increase after the ITSC is created, the instant of which is marked with a red arrow in the respective figures. A fault/no-fault decision is made by comparing FIS to the preset threshold (purple, high means fault). Both the FIS and the fault decision parameters are observed over the DAC pins of TMDXIDDK379D. Considering that FIS takes different values depending on the operating condition, different multipliers are utilized for better DAC visualization. The numerical value that the unit height of the oscilloscope screen corresponds is marked on the respective graphs in Fig. 4.7 and 4.8. The FIS value can be evaluated by comparison with respect to the unit height value. The results prove the effectiveness of the proposed algorithm over the entire operating range of the motor. Naturally, the higher numbers of shorted turns produce higher FISs hence they are easier to diagnose. A threshold level of $FIS \geq 30$ is set for all of the operating conditions in Fig. 4.7 and 4.8. No experiments regarding the proposed fault detection technique were conducted for the 5-turn ITSC case, for fear of permanent damage to the test machine. In any case, it is the lower severity ITSC faults (roughly 2% and 3% in our results) that shows the effectiveness of any fault detection method.

More stable and decisive results can be obtained for vector counts and the expected unbalance in their allocation, by the utilization of a higher number of electrical periods that the vector counting routine is done (N_{max} in Fig. 4.5). However, this will prolong the fault detection time. There exists a similar trade-off in the process of low-pass filtering the percent deviations observed. Increased low-pass characteristics prevents the fluctuations to a greater extent but the detection time can be delayed. For any practical implementation of the proposed fault detection strategy, these parameters and the trade-off relations should be tuned accordingly. In the presented

fault detection results of Fig. 4.7 and 4.8, the flowchart depicted in Fig. 4.6 is run once for every 5 full cycles of Ψ_s rotation.

Similar to the simulation files of Chapter 2 and Chapter 3, the source codes that include both the MPC motor drive and the proposed fault detection algorithm have been made available as open-source in [61].

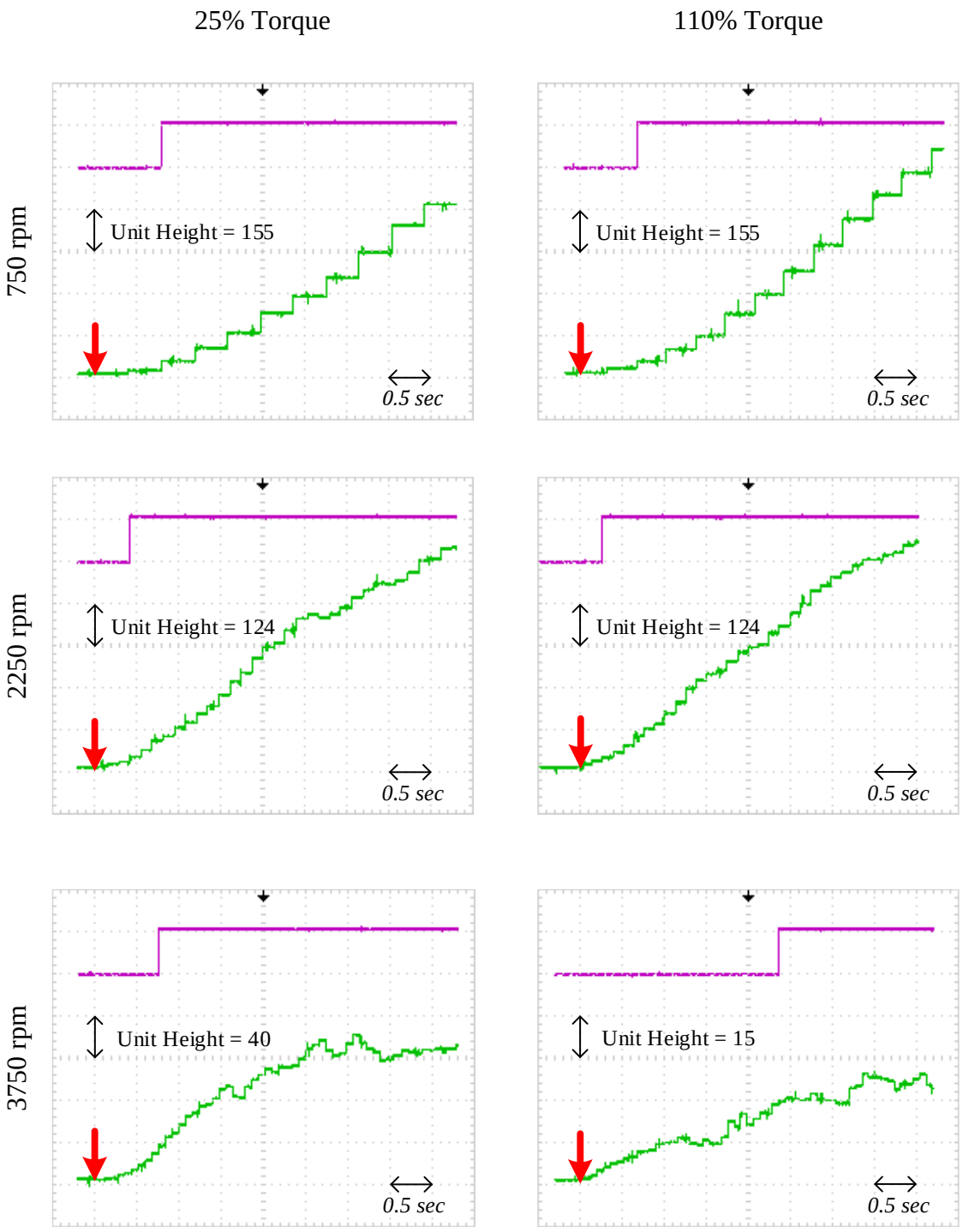

Figure 4.7. Fault detection performance of the proposed algorithm, under several different operation points, for an ITSC fault of 2-turns. FIS waveform: green, fault/no-fault decision: purple. The fault initiation is marked with the red arrow.

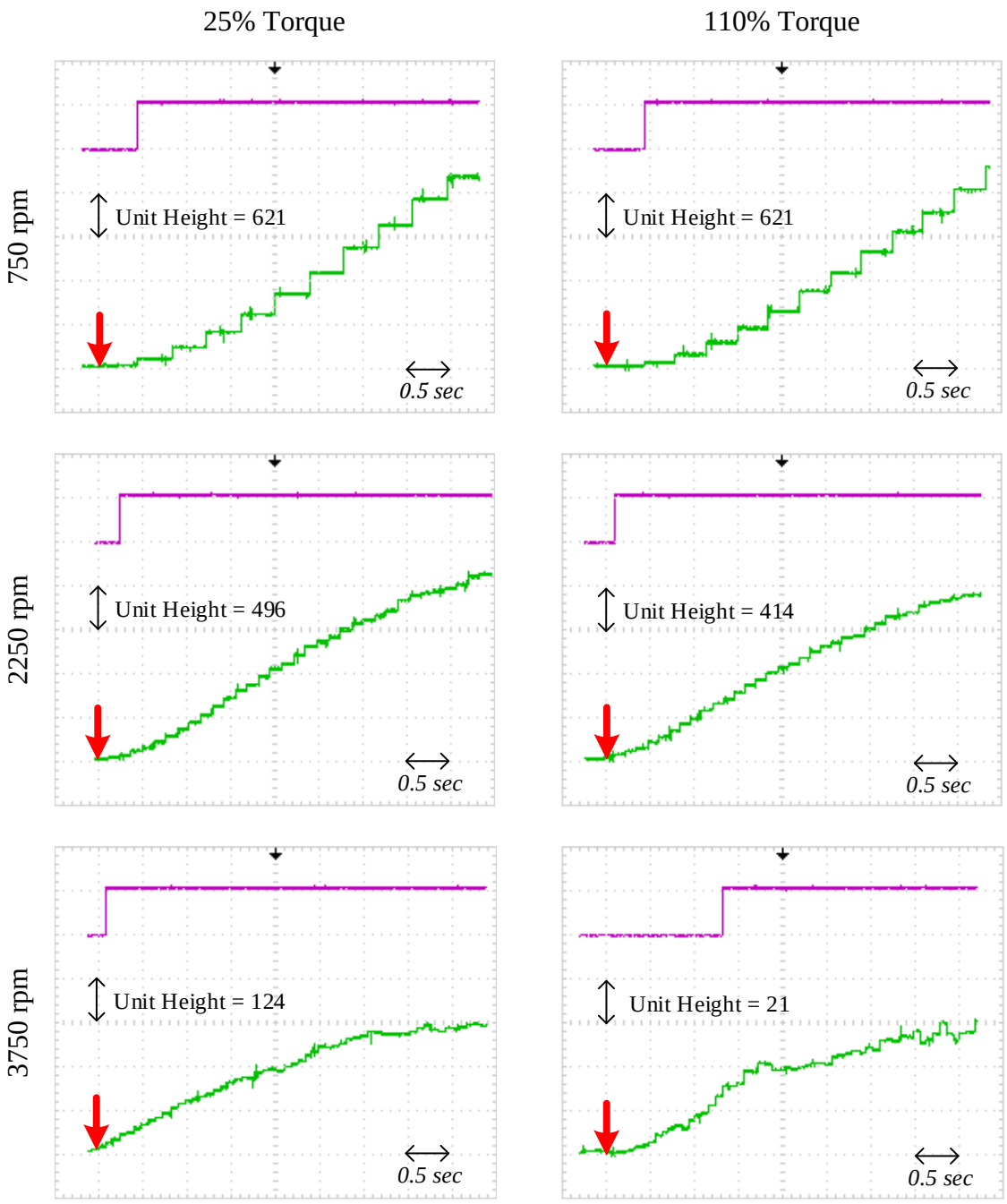

Figure 4.8. Fault detection performance of the proposed algorithm, under several different operation points, for an ITSC fault of 3-turns. FIS waveform: green, fault/no-fault decision: purple. The fault initiation is marked with the red arrow.

4.3.3 Discussions on the Proposed Algorithm

This section includes several discussions about the proposed fault detection strategy, which relies on the inspection of inverter statistics. The first item to be addressed is the suitability of FCS-MPC for the described fault detection method. The fundamental fault signature utilized in this thesis is the unexpected deviations in the controller outputs (i.e. inverter switching states). This is a rather general situation which can be anticipated to work also with other motor drive techniques, such as FOC or DTC. However, FCS-MPC is especially suitable for the proposed algorithm due to the considerations stated as follows:

- As described in detail in Chapter 2, MPC is an intrinsically fast control strategy. This stems from the fact that, the predictive controller does not act on a regular PI structure, which is basically a low-pass filter. The predictive control structure does not need an error term to be created and accumulated. Rather, it applies the most suitable vector in order to instantly minimize its cost function, which tracks the control objectives. Therefore, FCS-MPC can swiftly react to the disturbance created by the ITSC fault, which is then reflected by the change in controller outputs. In the case of FOC, the influence of the ITSC would appear as an additional second order AC term on the dq-quantities [143], [147], [150], which will also be low-pass filtered. Although FOC will also cover fault traces and try to maintain a balanced set of three-phase currents, its PI based control approach makes FOC less viable for the proposed fault detection method.
- In FCS-MPC, the controller outputs are discrete switching states which makes it very easy to record and evaluate the controller outputs in order to designate an unbalance. In the case of FOC, the controller outputs are DC quantities which are to be modulated. Hence, the evaluation of unbalance in FOC would correspond to subtracting and analyzing the second order component discussed above.

- In FOC, the controller outputs are inverse Park transformed and fed into the modulator stage. This translates into the inverter being able to synthesize positive-sequence voltages only. In FCS-MPC controller however, this is not the case and the inverter generates its voltage vectors without being necessarily fixed to a voltage scheme. This property may help the predictive controller structure to be better at repressing the fault's influence and be able to still continue supplying a balanced set of three-phase currents as shown in Fig. 4.3.

It can be observed from Fig. 4.7 and 4.8 that, the FIS magnitude and motor output power are inversely correlated. The reason behind is anticipated as the combination of two effects. First, the zero-vector utilization decreases as the speed, hence the back-EMF, increases. Secondly, a higher load torque demand can allow less margin for the controller to change the vector allocations with regard to fault. Consequently, smaller deviation percentages occur for high speed – high torque region.

For the preceding fault detection figures, the fault/no-fault decision is made solely on the comparison $FIS \geq 30$, and the fault flag is latched once the FIS exceeds 30. The threshold value is set by observing the FIS values over the entire torque-speed region and choosing a value large enough to avoid false triggers and small enough to spot the ITSC fault in the high torque – high speed region where the FIS turns out to be smaller than the rated operating condition. Utilizing statistical methods to decide on the threshold value or even setting a dynamic threshold based on the operating conditions would contribute to the proposed fault detection strategy.

Out of the three main IM fault types, namely stator, rotor, and bearing faults as discussed in Chapter 3, only the stator ITSC fault is considered in this thesis and other fault types are kept beyond the scope. Hence, the proposed algorithm's response to these types of faults could not have been tested. Nonetheless, these faults can be distinguished from ITSCs by their nature of the occurrence. A broken rotor fault's influence would be experienced equally by each stator phase. Bearing faults is a mechanical issue, and its rate of progression is expected to be slower than that

of an ITSC. In any case, it would be beneficial to spot any unexpected deviations in the controller output, even if the inflicting fault's type is falsely identified.

There exists a complex interaction between the fault and the controller. The influence of an ITSC fault on the controller is previously presented in [160], in which a DTC-driven IM is assumed. The presence of an ITSC fault causes errors in torque and flux estimation and DTC was found to be compensating the visible effects until the control is lost. No fault detection scheme is presented in [160], neither the changes in the vector allocations due to the fault are discussed. Although a similar attempt is provided in this chapter for ITSC and MPC interaction, in order to explain the ITSC fault's effect on MPC; there is still a gap in the literature on how the faults affect or corrupt the controller performance. Hence, this subject can be addressed as future work.

In order to assess the proposed algorithm's performance under dynamic operating conditions (where the speed command and the load torque varies), the motor drive is commanded to run with a triangular wave speed command, such that the motor changes speed from 750 rpm to 3750 rpm in approximately one second. Since the mechanical load to the motor is a PMSM run as a generator feeding a resistive load as described in Chapter 2, the load torque also varies quadratically with respect to the speed. The resultant FIS response shown in Fig. 4.9 suggests that the proposed algorithm can work in the dynamic case, too.

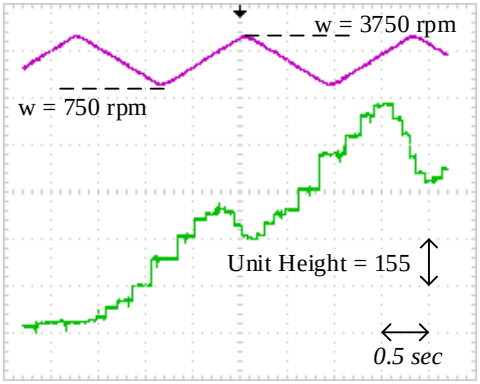

Figure 4.9. The fault detection performance of the proposed algorithm under dynamic operation. Purple: motor speed in rpm. Green: fault indicating score.

In Chapter 4.3.1, the low-pass filtering of the active voltage vector deviations was discussed. To illustrate the effect of the low-pass filtering stage, both the unfiltered deviation figures and the regular FIS waveform are shown on the same graph in Fig. 4.10 for an ITSC fault of 2-turns at rated operating points. As previously discussed, low-pass filtering avoids fluctuations to a considerable extent at the expense of delayed response. Although a significantly faster response could be obtained by less filtering (or no filtering at all), this might risk false decisions.

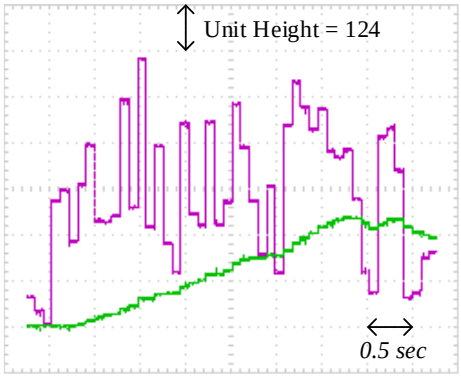

Figure 4.10. The FIS waveforms; calculated from the low-pass filtered deviations (green) and the unfiltered version (purple).

As a further investigation of the proposed fault detection algorithm's performance, several different FIS waveforms, five for the healthy operation at rated values case and another five for the 2-turns ITSC case, are depicted on the same graph, in Fig. 4.11. It can be seen from the Fig.4.11 that the algorithm is reliable as the healthy case produces FIS close to zero.

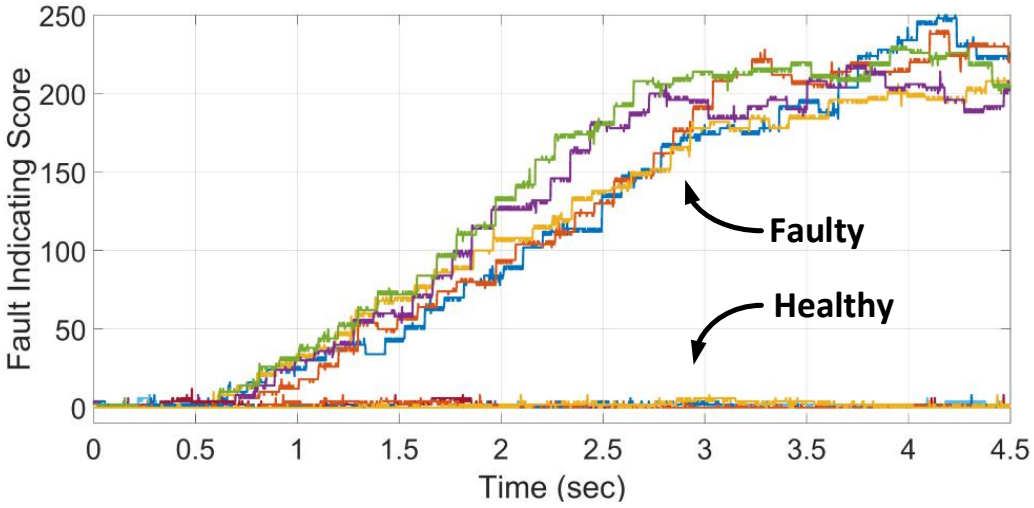

Figure 4.11. Several different FIS waveforms; for both the healthy case and the two turns ITSC case under rated operating conditions.

As described in detail in Chapter 2, choosing $|\Psi_s|^{ref} = 0.4$ for the induction machine on which the experiments are done, corresponds to an increased-flux mode such that its power factor is relatively low (around 0.5). In order to check the influence of the level of magnetization on the fault detection performance, the algorithm is run for a decreased stator flux magnitude level of $|\Psi_s|^{ref} = 0.3$, instead of $|\Psi_s|^{ref} = 0.4$. Fault detection performance is depicted in the same fashion in Fig. 4.12. It can be concluded from Fig. 4.12 that; the fault detection performance is even better in this case, mainly due to the higher utilization of zero vectors for the high-speed operating points. Therefore, $|\Psi_s|^{ref} = 0.4$ mode of operation resembles a worst case scenario compared to a more convenient flux setting of $|\Psi_s|^{ref} = 0.3$. Results for both cases are provided in this chapter, for the sake of completeness and to utilize the flux level as a parameter in the fault detection performance.

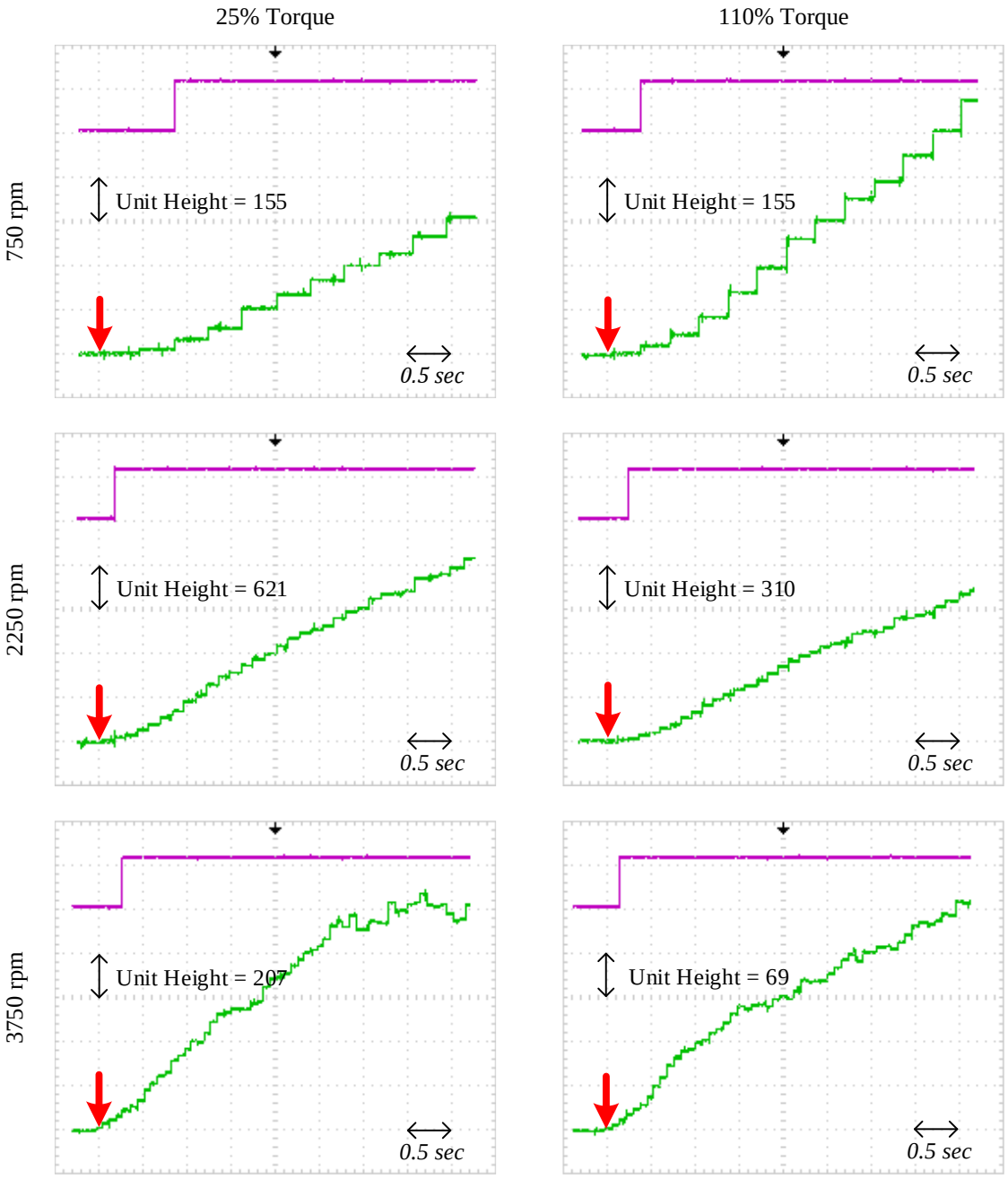

Figure 4.12. Fault detection performance of the proposed algorithm, under several different operation points, for an ITSC fault of 2-turns, with $|\Psi_s|^{ref} = 0.3$. FIS waveform: green, fault/no-fault decision: purple. The fault initiation is marked with the red arrow.

Although it is not expected for a machine to recover from an ITSC fault and go back to its normal (healthy) operation, in order to express the strong correlation between the ITSC fault and the FIS, a fault-removal case is depicted in Fig. 4.13. The intentional ITSC fault of 2-turns was cleared at the instant marked with the red arrow. It can be observed that the FIS quickly decays to near-zero values (healthy case) which then proves that FIS is a strong indicator of fault presence.

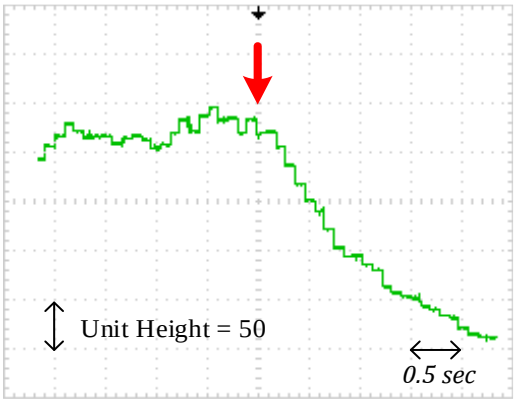

Figure 4.13. The FIS waveform (green); for the removal of a 2-turns ITSC fault. The red arrow indicates fault removal instant.

In FCS-MPC, the weighting factor (λ) is a fundamental parameter that tunes the controller response. Increased value of λ puts more emphasis on the flux magnitude error term and implicitly improves the phase current waveform quality. Several different λ values, ranging from 30 to 100 have been tested. Phase current THD is near minimal for $\lambda = 50$ (1.3%) and increasing λ further provides little to no decrease in THD. For $\lambda < 30$, the current waveforms become perceptibly distorted. The effect of λ on the fault detection performance is also similar; although the proposed method still detects faults, smaller values of λ make FIS smaller. Furthermore, oscillations in FIS and discrepancies such as different amounts of deviations for the same group of vectors (e.g., $\Delta v_1 \neq \Delta v_4$) are magnified for $\lambda \leq 30$. The results depicted in Fig. 4.7 and 4.8 are provided for $\lambda = 50$.

A similar relation exists between fault detection performance and the sampling frequency. Due to the powerful microprocessor utilized in the experimental setup, the computation time is merely 11.4 μs hence a rather high sampling frequency of 40 kHz could be implemented. Experiments repeated with a sampling frequency of 20 kHz still provide fault detection with decreased FIS.

In order to stress further on the last two topics, i.e., the influence on sampling frequency and the weighting factor λ on the fault detection performance, additional FIS waveforms are provided in Fig. 4.14 and 4.15. The sampling frequency is reduced to 20 kHz and $\lambda = 25$ is set. In this configuration, fault detection could not be made for the rated operating conditions. For 2250 rpm and rated torque, the FIS waveform of Fig. 4.14 was obtained, for which the ITSC fault was barely spotted with a deliberately reduced fault threshold of just 5, due to the much smaller FIS values compared to the standard case.

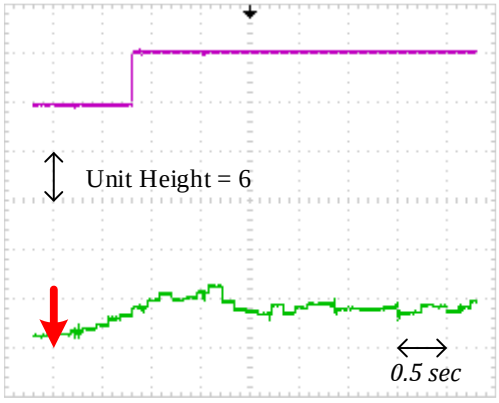

Figure 4.14. The FIS waveform for 2250 rpm and rated torque under 20 kHz sampling frequency and $\lambda = 25$. FIS waveform: green, fault/no-fault decision: purple. The fault initiation is marked with the red arrow.

While the sampling frequency is still at 20 kHz, $\lambda = 40$ is set which prioritizes the stator flux error in the cost function hence implicitly stator current waveforms. Even though the FIS waveform takes smaller values compared to the original case, fault

detection at rated condition could be achieved with this arrangement, as shown in Fig. 4.15. The fault threshold was set back to 30 as in the original setting.

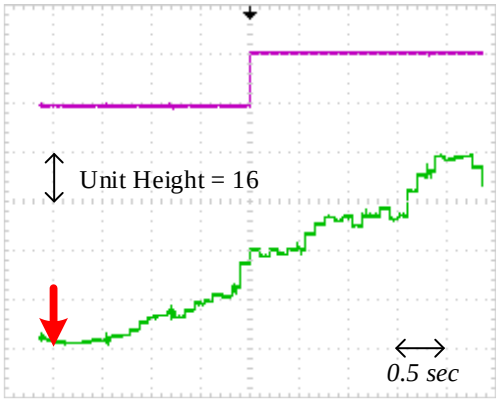

Figure 4.15. The FIS waveform at rated operating conditions under 20 kHz sampling frequency and $\lambda = 40$. FIS waveform: green, fault/no-fault decision: purple. The fault initiation is marked with the red arrow.

It is evident from the Fig. 4.14 and Fig. 4.15 that a high-performance control on the current waveform quality is a pre-condition for the proposed fault detection approach. Reduced control performance due to either both sampling rate reduction or selecting an inconvenient λ results in the loss of fault detection capability.

The last issue to be discussed here is a rather generic one: considering the detection performance of ITSC faults, the fault resistance is a critical parameter. As described earlier, although the intentional short circuits were created over a long external cable, which introduces an additional resistance of $0.13\ \Omega$, no additional resistance was utilized to resemble the fault resistance, in the experimental results depicted so far. To examine the performance of the proposed fault detection algorithm, the fault detection results are repeated for additional resistances of $0.2\ \Omega$ and $0.33\ \Omega$ included in the short circuit path, and shown in Fig. 4.16. The experiments are done for $3000\ rpm$ operation, with $|\Psi_s|^{ref} = 0.3$.

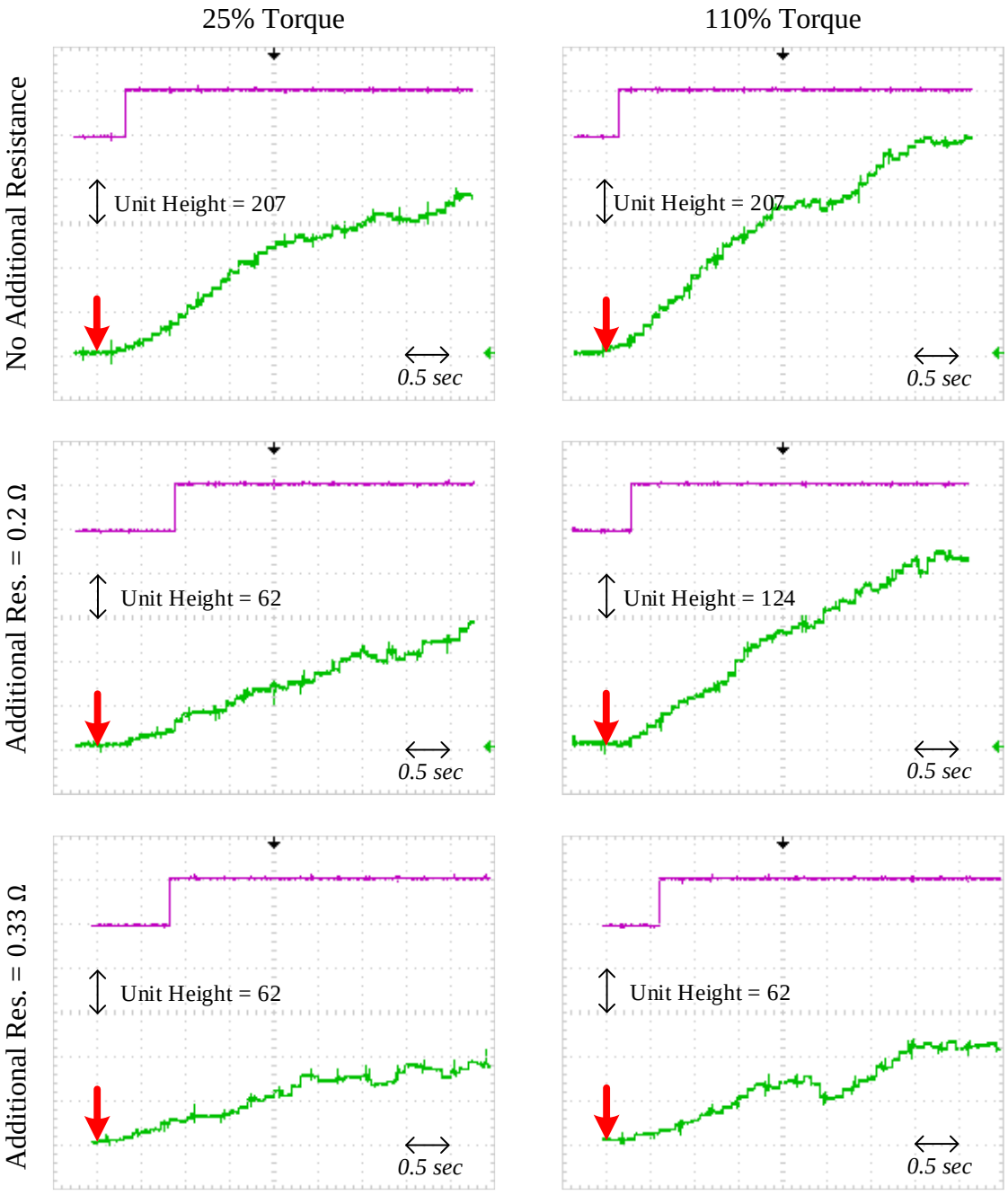

Figure 4.16. Fault detection performance with additional fault resistances of 0.2 Ω and 0.33 Ω. FIS waveform: green, fault/no-fault decision: purple. The fault initiation is marked with the red arrow.

It can be concluded from Fig. 4.16 that, although the lower FISs are observed with increasing external resistances, the proposed algorithm is still able to detect the inflicting fault, at least for the rated operation. As the fault resistance directly determines the fault current, hence the strength of fault's influence on motor operation, fault detection is harder for increasing values of fault resistance.

In order to exemplify the influence of fault resistance, fault current waveforms are recorded and depicted in Fig. 4.17, for $\omega = 3000\, rpm, T_e = 1.35\, N.m$ operation, with $|\Psi_s|^{ref} = 0.3$. Since the fault current is a direct result of the back-EMF over the shorted turns divided by the fault resistance, the increasing values of fault resistance resembles a challenge for any fault detection algorithm. It is also worthwhile to note that being able to detect the fault with the extra resistance of $0.33\ \Omega$ is especially meaningful for the proposed algorithm, because the fault current for that particular case is close to the rated phase current magnitude, as can be seen on Fig. 4.17.

a)

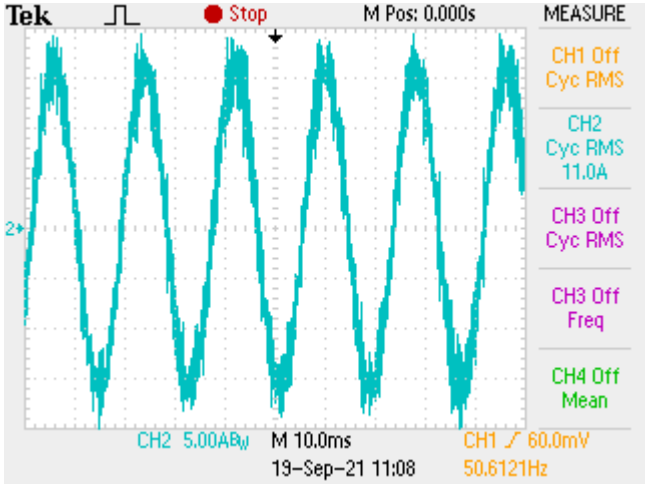

b)

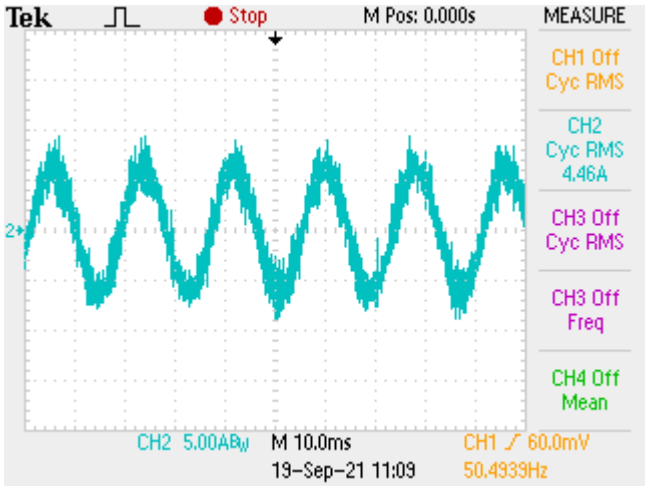

c)

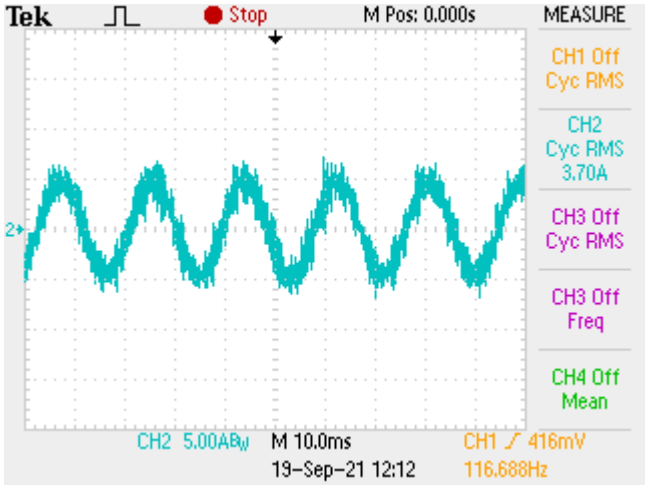

Figure 4.17. The fault current waveforms for no external resistance (a), and with external resistances of of 0.2 Ω (b), and 0.33 Ω (c) at rated operation with $|\Psi_s|^{ref} = 0.3$.

4.3.4 A Benchmarking Study for the Proposed Fault Detection Method

An exact benchmarking between any two fault diagnosis methods requires experimentation with the same machine, fault, and operating conditions, hence it is hard to realize. Nonetheless, the complete assessment of the proposed fault detection method should consider the previously suggested fault detection strategies. Therefore, several selected ITSC fault detection schemes developed for closed-loop controlled machines are compared in Table 4.3 with the proposed algorithm. For the sake of completeness, the proposed algorithm (as published in [16]) is also included in the first raw of Table 4.3.

A fundamental parameter that can be utilized for benchmarking in fault diagnosis methods would be the severity factor (μ), which was defined as the ratio of the shorted turns to the total number of turns in the phase ($\mu = N_f/N_{ph}$). With the proposed method, two shorted turns (out of 104 turns in a phase) are detected ($\mu =$ 1.9%), which can be considered quite satisfactory among the other methods presented in Table 4.3. It should be noted that the severity ratios may differ in some of the papers cited in Table 4.3, due to the adoption of different definitions for the severity ratio, as in [150] and [145]. Furthermore, additional fault resistances may or may not be utilized, and the physical structures of the artificial faults created for the experiments would differ. Therefore, the severity factor alone should not be regarded as an ultimate quality figure. A single-turn fault option was not made available in the experimental IM; hence this case could not be tested. FIS waveforms obtained for the two turns fault in Fig. 4.7 suggest that a single-turn fault could have been detected too, at least for the low to medium speed region.

Table 4.3 A Review of Existing Fault Diagnosis Methods That Consider Closed-Loop Controlled Machines.

Ref.	Motor Type & Control Method	Severity (%) ($\mu = N_f/N_{ph}$)	Detection Method
[16]	**IM, FOC**	**1.9**	**Inverter Statistics**
[144]	PMSM, FOC	9.85	Freq.-Domain Analysis
[143]	IM, FOC	8.33	Freq.-Domain Analysis
[161]	IM, FOC	0.93	Impedance
[147]	IM, FOC	0.32	Freq.-Domain Analysis
[148]	IM, FOC+PCC	0.76	Inverter Statistics
[149]	PMSM, FOC	3.23	PWM Ripple
[150]	PMSM, FOC	1.39	Freq.-Domain Analysis
[151]	PMSM, FOC	2.78	Time-Freq. Distribution
[152]	IM, FOC	0.30	High Freq. Injection
[145]	IM, DTC	1.08	Freq.-Domain Analysis
[153]	IM, DTC	2.04	Freq.-Domain Analysis
[154]	PMSM, FCS-MPC	5.00	Wavelet Tr. on Cost Fnc.
[157]	FOC, IPMSM	1.38	Torque-Angle
[156]	Non-specified, IPMSM	12.50	Impedance
[158]	Non-specified, PMSM	1.85	Current Estimation Error

It can be concluded from Table 4.3 that; frequency domain analysis is the favored strategy for fault detection. In most papers, fault detection has been reduced to addressing unexpected frequency components that would otherwise diminish for a healthy machine. This can be addressed as a major simplification in the respective studies because making the final decision is whole another algorithm to be implemented and tuned. A faulty/healthy decision, as shown in the respective fault detection figures provided so far, is presented only in [150].

In this paper, the proposed fault detection algorithm is tested for several different speed and load torque levels where fault detection performance for a wide torque-speed range was documented only in a limited number of studies ([144], [147], [150], [161],[158]) from Table 4.3. Similarly, fault detection performance under dynamic operating conditions is depicted in Fig. 10 of this study where only [151] and [158] consider the dynamic case, among the references of Table 4.3.

The publications on fault diagnostics almost unanimously express how critical it is to detect a fault as soon as possible to avoid catastrophic damage. Considering the rate of progression of an ITSC fault, it is very interesting to see that fault detection time is explicitly mentioned only in [152]. The elapsed time between fault's occurrence and detection is reported below two seconds in [152], which is roughly equal to the detection times of this paper, which can be observed from Fig. 4.7.

Among the fault diagnosis algorithms listed in Table II, details regarding the microcontroller on which the fault detection algorithm is implemented and the computational burden brought by its application are virtually non-existent. The ITSC detection strategy presented in this paper runs on the same CPU alongside the FCS-MPC routine. The total time spent on the full execution of the flowchart depicted in Fig. 4.6 is experimentally measured by setting a DAC pin high at the beginning of the fault detection algorithm and setting the same pin low at the algorithm's end. The algorithm execution time is merely 11.4 μs, and can be seen in Fig. 4.18. The algorithm is very intuitive, and it is straightforward to be implemented as a simple add-on to the standard FCS-MPC structure. The proposed algorithm is online and

non-evasive. Neither an additional circuit (as in [149], and [156]) nor an external sensor (as in [145]) is required.

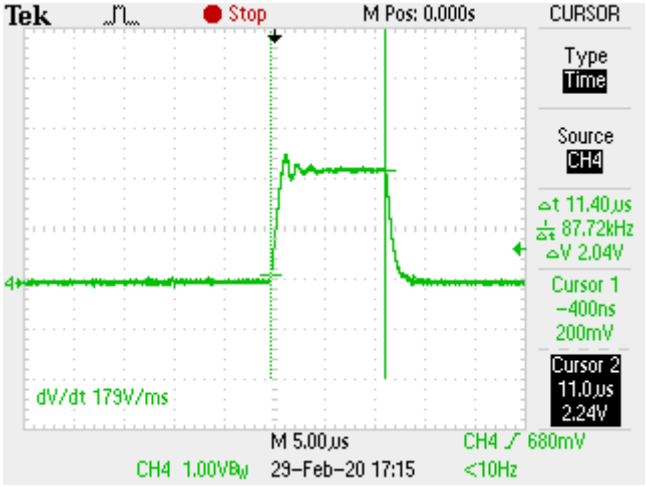

Figure 4.18. The fault detection algorithm's execution time.

4.4 An Alternative Approach: ITSC Detection via Zero-Vector Distribution Unbalance

In Section 4.2, two strategies for fault detection were proposed as follows:

- Examination of the unbalance in the allocation of active vectors.
- Examination of the unbalance in the zero-vector allocation across the sectors of the complex plane.

Due to its better fault detection performance, the proposed fault detection algorithm is built on the examination of the unbalance in the allocation of active vectors. On the other hand, examination of the unbalance in the zero-vector allocation across the sectors of the complex plane is also another useful approach for fault detection. Therefore, fault detection via the zero-vector observation approach will be described in this section, for the sake of completeness.

The fundamental idea utilized here is to expect a balanced distribution in the utilization of zero vectors across the sectors of the complex plane as depicted in Fig. 4.4. An ITSC fault would disturb this balance. Hence, the examination of zero-vector allocations, the flowchart of which is depicted in Fig. 4.19, can be proposed as a means for fault detection.

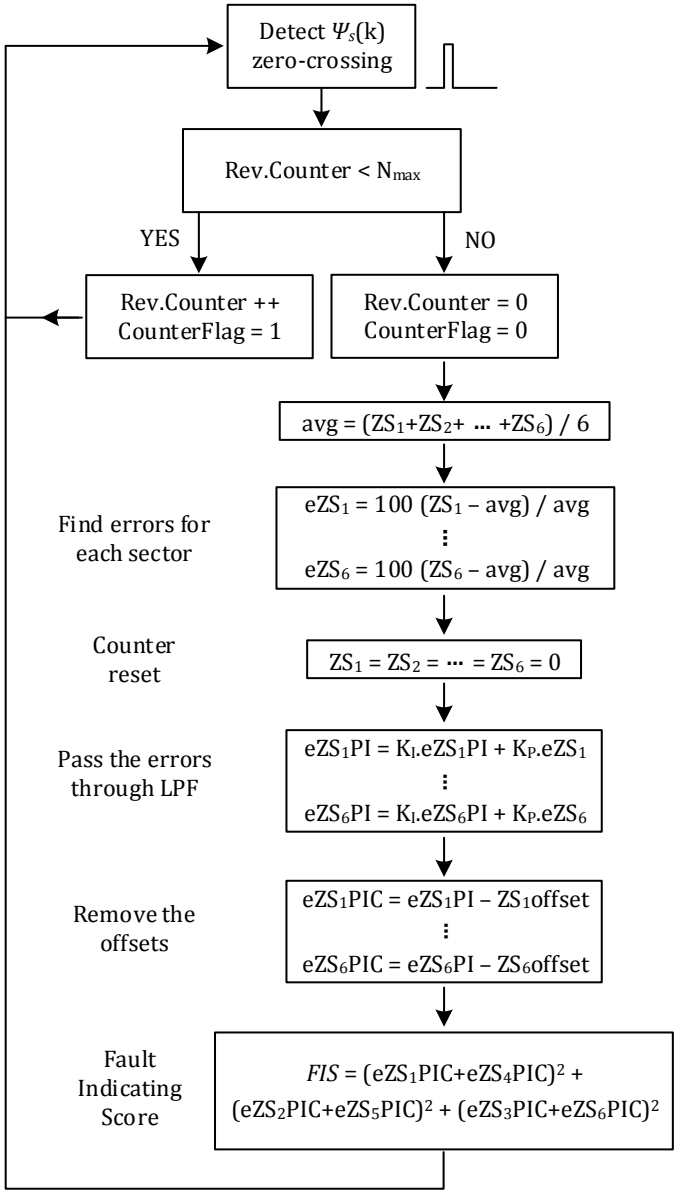

Figure 4.19. Flowchart diagram for the ITSC fault detection algorithm via zero-vector distribution.

The fault detection performance of the zero-vector distribution approach is depicted in Fig. 4.20 for an ITSC of 2-turns. The flowchart depicted in Fig. 4.19 is nearly identical to the one depicted in Fig. 4.6, i.e., the flowchart for the active vector counting based fault detection approach. The fundamental difference here is that; the active vectors are not counted. Rather, the sector that the stator flux vector is currently occupying is noted (S_1, S_2, etc.) by increasing its corresponding counter, whenever a zero vector is selected by the optimization routine.

Although there is definitely a correlation between an ITSC fault and the unbalance in the allocation of zero vectors across the sectors of the complex plane, this fault detection approach significantly underperforms the former approach. The FIS values were initially zeroed during the recording of Fig. 4.20 yet a large amount of FIS fluctuations and false-positive results were observed during the experiments. Moreover, no intelligible data was observed for the low speed – high torque operation. The FIS scores follow no regular trend in their magnitudes.

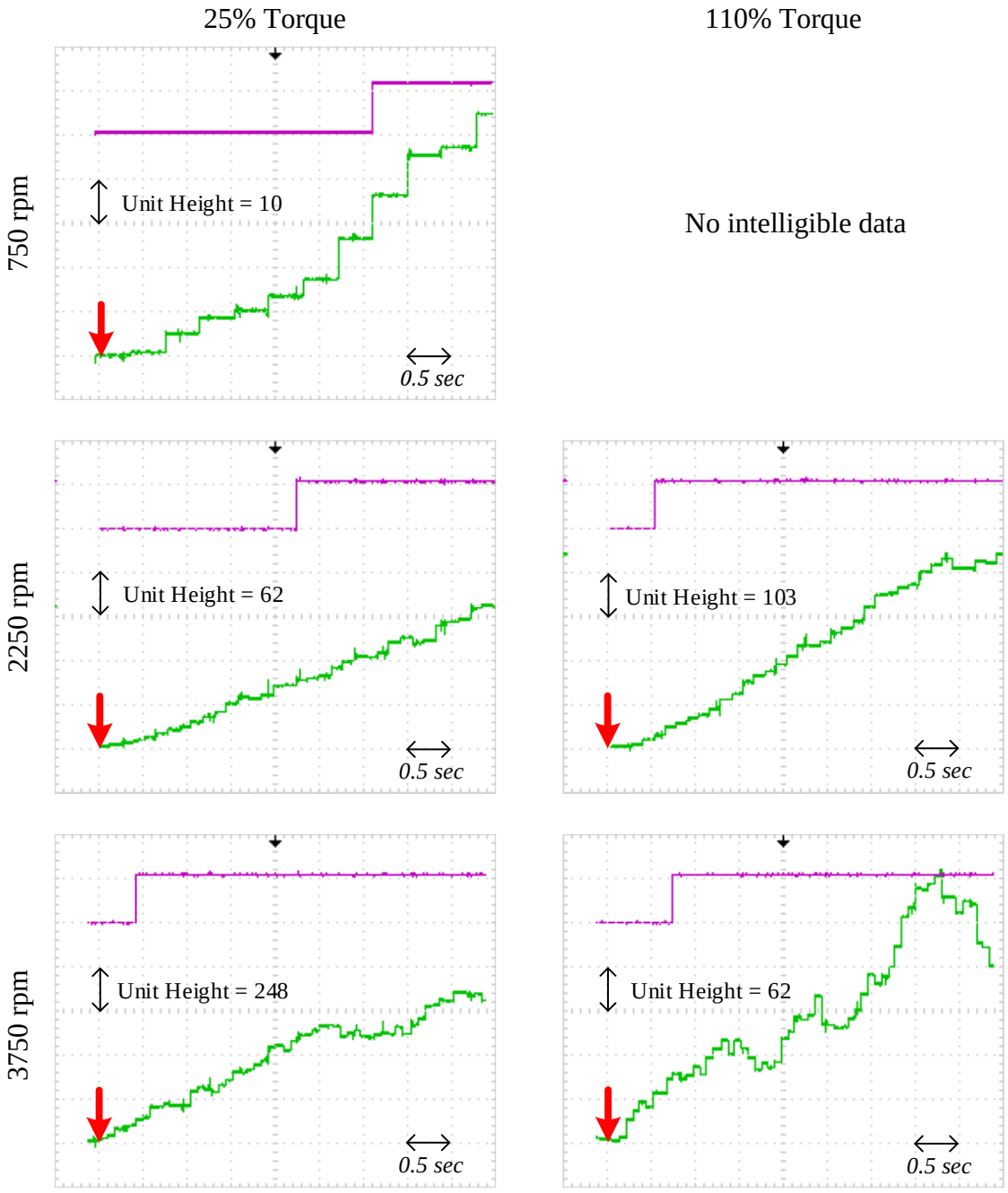

Figure 4.20. Fault detection performance of the zero-vector distribution approach, under several different operation points, for an ITSC fault of 2-turns. FIS waveform: green, fault/no-fault decision: purple. The fault initiation is marked with the red arrow.

For the healthy case under the rated conditions, the FIS waveform is plotted in Fig. 4.21, which shows that the FIS has considerable magnitude and a false-positive diagnosis is made, which was not the case for the former approach. Due to the large fluctuations and relatively larger FIS values, the fault indicator's threshold was set at 100, but it was lowered to 30 for the low-speed case in order to be able to diagnose the inflicting fault.

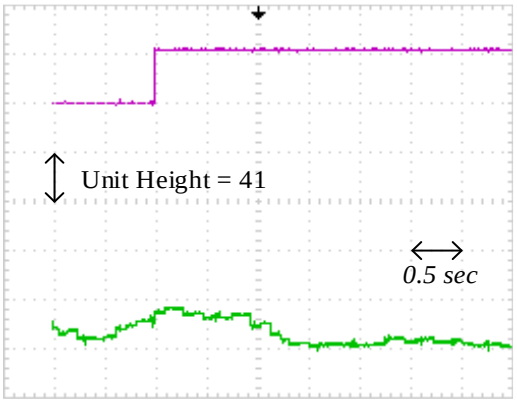

Figure 4.21. A false-positive example during healthy operation at rated values, with the zero-vector allocation approach. FIS waveform: green, fault/no-fault decision: purple.

Consequently, ITSC fault detection via the unbalance in the allocation of zero vectors across the sectors of the complex plane will not be pursued further as a fault detection method. Experimental results, which were obtained under the high-flux reference case, are provided though. Finally, it is worth noting that the zero vector firing numbers were observed to decrease by 22% in sectors S_1 and S_4, and increase by roughly 20% in sectors S_3 and S_6, under rated operating conditions.

4.5 Further Considerations on ITSC Fault Detection via Predictive Control

In this part, some further issues regarding the predictive controller and ITSC fault interaction will be discussed. This chapter is intended as an attempt to re-apply and evaluate some selected fault detection methods and approaches previously reported in the literature.

4.5.1 The Relation Between the ITSC Fault and the Current Ripples

The first issue to be examined here is the interaction between the ITSC fault and the current ripple, or consequently; high-frequency impedance of the faulty phase. We can see that this interaction has been utilized as a fault signature in the existing literature from Table 4.3. Experimental verification of this interaction would be informative. Therefore, current ripple under an ITSC fault has been observed under the ITSC fault. Considering the fact that the FCS-MPC strategy results in a variable switching frequency operation, capturing the current ripples clearly on the oscilloscope screen is problematic. To overcome this problem, constant DC currents are commanded to flow over the phases, in such a way that 4.33 A flows over the phase that the ITSCs are to be created and returns from the other two phases, while the motor is at a stand-still. The current reading setting of the current clamp is set to the AC mode to capture the ripples only. The current ripple waveforms corresponding to the healthy case (a) and the 2-turns ITSC fault case (b) are depicted in Fig. 4.22. The DC bus voltage level was reduced to 300 V for this experiment in order to avoid overheating due to larger current ripples that may result due to the lack of the back EMF in stand-still operation.

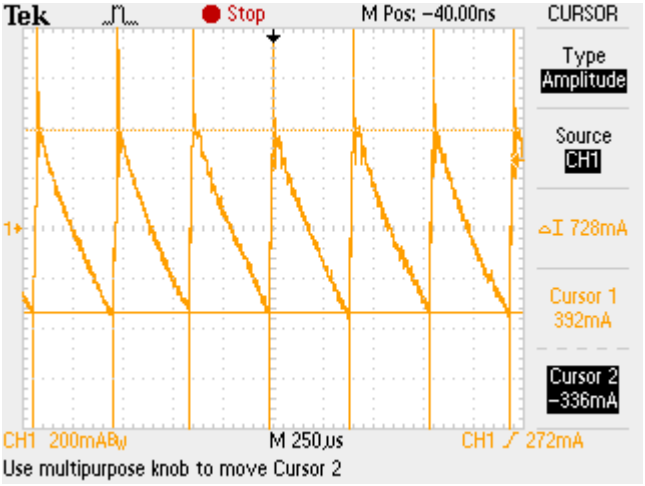

a) Peak to peak current ripple of 728 mA for the healthy case.

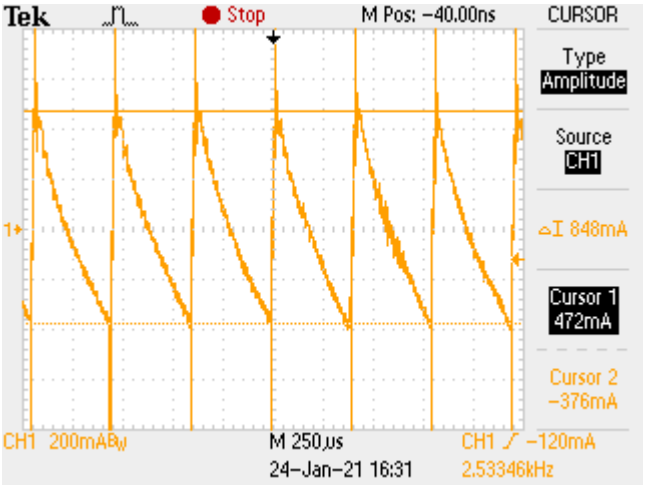

b) Peak to peak current ripple of 848 mA for the 2-turns ITSC fault case.

Figure 4.22. The current ripples for the healthy case (a), and the 2-turns ITSC fault (b).

It can be observed from Fig. 4.22 that the current ripple is increased by approximately 16% by the presence of an ITSC fault. Hence, we can conclude that the ITSC fault effectively reduces the high-frequency impedance of the phase that is created on, and consequently increases the current ripple.

4.5.2 The Relation Between the ITSC Fault and the Cost Function

The second issue to be considered here is the interaction between the cost function output and the inflicting ITSC fault. As thoroughly explained in Chapter 2, the FCS-MPC routine evaluates all possible switching combinations with a cost function. The switching vector for which the cost function evaluation yields the minimum value is selected as the optimum and applied at the next switching state.

The cost function output (for simplicity, will be shortly referred to as the "cost", hereon) is a characteristic feature of the FCS-MPC. It has recently been utilized as an ITSC fault indicator in [154], for a PMSM drive controlled by FCS-MPC. It is very intuitive to expect deviations in cost with an inflicting fault. The study reported in [154] will not be repeated here, but even a broad examination of the cost and fault's interaction would be informative.

The cost function waveform (to be precise: the minimum cost value obtained for each control cycle) is obtained by feeding the related parameter to the DAC pins of the development kit (TMDXIDDK379D) and displayed in Fig. 4.23. As detailed in Chapter 2, due to the powerful microprocessor utilized in the implementation, the control frequency is set to a rather high value of 40 kHz. Therefore, the expected deviations in electrical quantities per control action, hence the magnitude of the cost function is small in magnitude. For a nice visualization of the cost function, proper multipliers (10000 for Fig.4.23) are adopted when feeding the cost function figure into the DAC pin, which creates corresponding analog outputs that can be observed via an oscilloscope. Therefore, throughout this discussion, the voltage value displayed on the oscilloscope is not directly meaningful. Rather, the influence of the

ITSC on cost function level and shape is to be examined. All of the following cost function figures were recorded under rated operating conditions of the IM. High-flux operation is adopted as in the case of Fig. 4.7-4.8, i.e., $|\Psi_s|^{ref} = 0.4$.

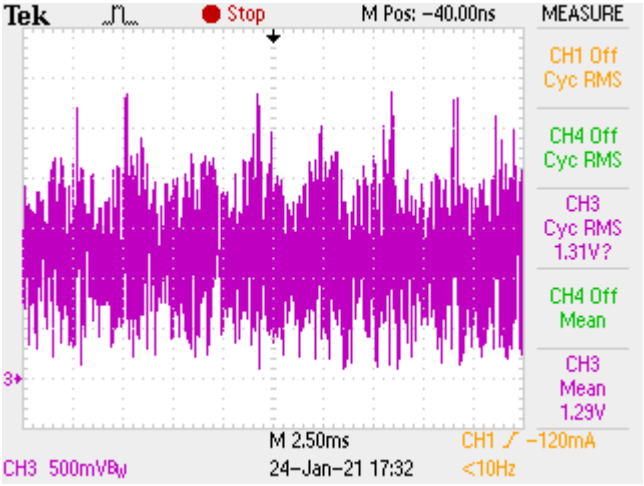

Figure 4.23. The cost function waveform for the healthy operation at rated operation, with a DAC multiplier of 10000.

Since the cost function waveform's frequency (40 kHz) is much higher than the electrical frequencies of interest, low-pass filtering the cost function output would provide more intelligible results. Therefore, a low-pass filter of PI form is utilized for the display of cost function graphs, with filter parameters $K_I = 0.95, K_P = 0.05$. Therefore, while the high-frequency jumps and the influence of noise are eliminated, behavior with respect to the electrical frequencies of interest is preserved.

The low pass filtered cost function waveforms are depicted in Fig. 4.24, for the healthy (a) and faulty cases; 2-turns (b) and 3-turns (c) ITSC. A multiplier of 15000 is adopted for DAC visualization.

a)

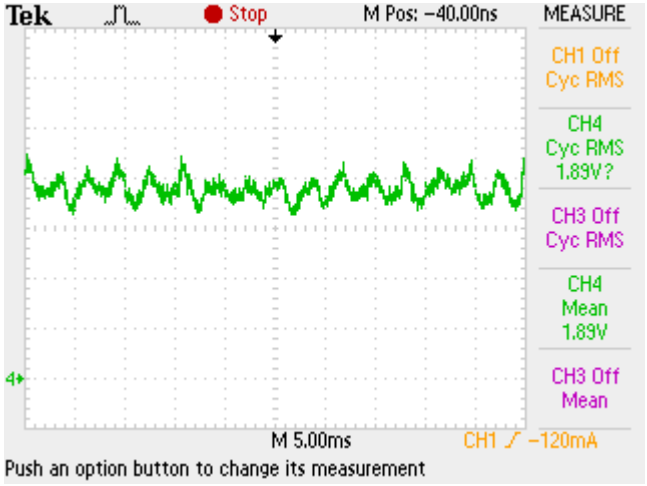

b)

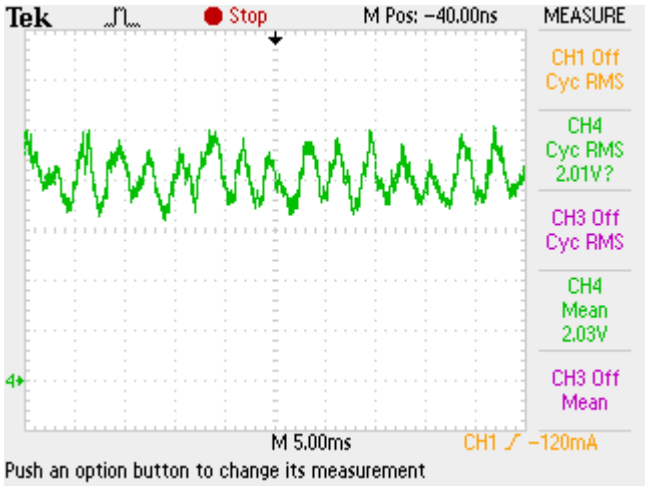

c)

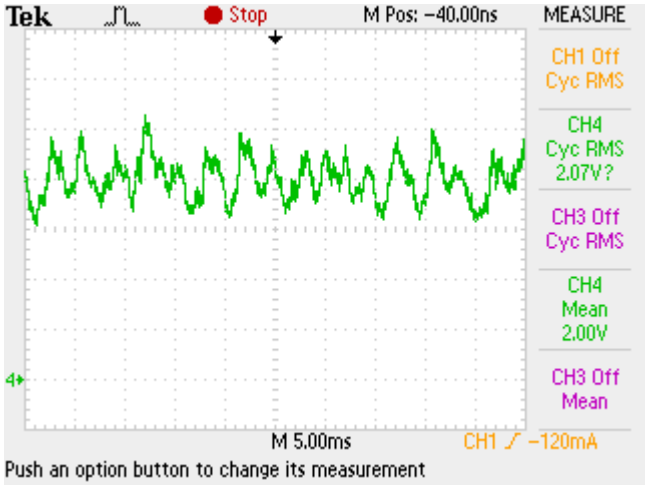

Figure 4.24. The low-pass filtered cost function waveforms for the healthy (a) and faulty operation (2-turns (b), and 3-turns (c)) at rated operation.

Considering the cost function waveforms depicted in Fig. 4.24, it is obvious that the cost function is affected by the presence of an ITSC fault. Both the average DC value is increased and the included AC ripple is intensified. However, a fault detection approach based solely upon a magnitude comparison for cost function outputs would not be effective due to two reasons. First, the changes in cost function waveforms due to the inflicting fault are not as dramatic as those of the proposed algorithm's FIS waveforms. Secondly, the natural variations and ripples would trigger false alarms in a magnitude-based fault detection strategy. The waveforms provided in Fig. 4.24 were observed to have significant oscillations that may be even larger than the changes in magnitude created by the fault's influence.

The next step for the analysis of the fault and cost function interaction will be the frequency domain analysis. Two separate cost function waveforms for healthy operation and another two for the 3-turns ITSC fault case for rated speed and load were recorded. The spectral density graphs for these waveforms were obtained using FFT operations on MATLAB and the resultant comparison graph is depicted in Fig. 4.25.

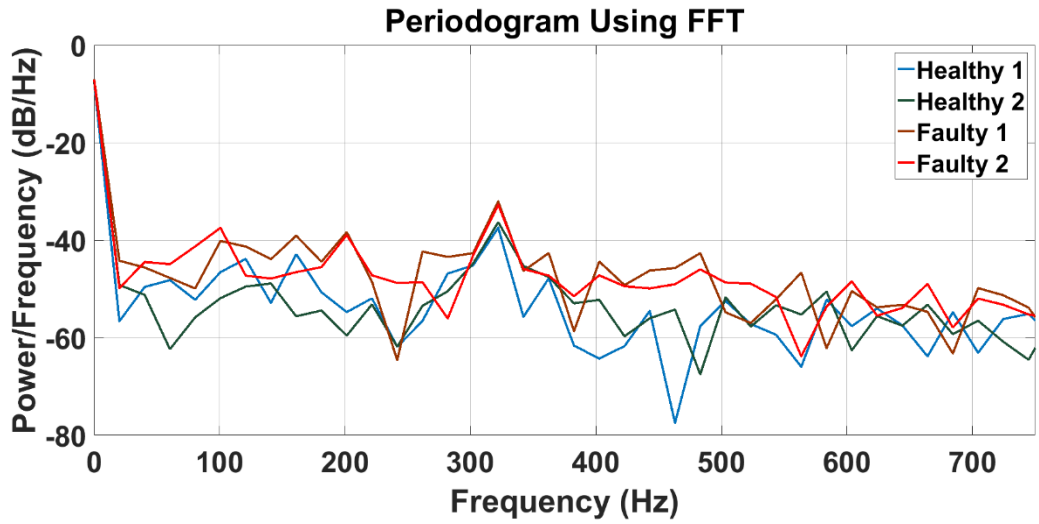

Figure 4.25. Spectral density graphs for the cost function waveforms under healthy and faulty operation.

Several observations regarding the cost function's response to an ITSC fault can be made by examining Fig. 4.24 and Fig. 4.25. Although the fault causes an increase both in the average value and the AC content of the cost function, the trend is not very regular so that the spectral density graph can be easily utilized as a fault indication method. In the spectral distribution, there are significant differences even for the healthy operation waveform. The increase corresponding to 320 Hz (roughly the 6^{th} harmonic) is not large in magnitude but it is found to be consistent. Significant changes in magnitude (most presumably due to the ITSC fault) occur for roughly 200 Hz and 450 Hz, but even these variations are small compared to the drastic FIS response of the proposed algorithm. Consequently, the cost function waveform is found to be definitely responsive to the fault occurrence but the experimental evaluation regarding its nature of response does not offer a simple tool for fault diagnostics as the one utilized for the proposed algorithm.

From the preceding discussion, it can be concluded that although there exists some interaction between the ITSC fault and the cost function output value as expected, the interaction was not found to be strong enough to be utilized as a reliable fault indicator, at least for our motor and drive structure and its related settings. Reference [154] proposes an ITSC detection scheme based on running wavelet transform on the cost function for an FCS-MPC driven PMSM. In the experimental results of [154], it can be seen that the cost function waveform exhibits a decisive increase in magnitude with the initialization of the fault, without even running any transformation. Besides, motor current waveforms are perceptibly distorted, furthermore, even the speed oscillations are magnified. In our experiments, however, the experimented ITSC effect is small and it is successfully covered by the controller. The main difference between these two attempts that investigate ITSC and cost function relationship can be anticipated as the difference whether the fault significantly alters the controlled parameters or not. In our experimental analysis, the ITSC cannot move the controlled parameters significantly away from their healthy case therefore the cost function's response is not exaggerated.

4.5.3 The Relation Between the ITSC Fault and the Current Prediction Error

The third issue to be considered here is the interaction between the current estimation performance and the ITSC fault. It is natural to suggest that any inflicting fault would inevitably disrupt the mathematical model assumed for the healthy case. We have seen in the preceding parts that the ITSC fault makes the high-frequency impedance decrease and causes the current ripples to increase, such that these features were utilized as fault indication methods [149], [156]. ITSC fault detection based on observing the difference between the predicted and measured current is previously proposed in [158]. In the following, a similar approach will be implemented for our FCS-MPC driven IM case.

In FCS-MPC, predicting the next value of the motor currents under the influence of the available voltage vectors is a fundamental part of the control routine, as explained in Chapter 2 in detail. Consider that the current prediction for the optimum vector, that is the vector that yields the minimum cost and selected for application, is noted in every control cycle and this recorded current prediction is compared to the real current value which is recently measured when the next control cycle comes. The difference between the predicted and the measured current values can be expected to increase with the presence of an ITSC. This approach is especially suitable for the FCS-MPC strategy because the current prediction step is already in the control routine therefore no significant computation burden is brought with the inclusion of prediction performance observation.

Standard FCS-MPC strategy is run in the stationary stator reference frame, i.e., αβ domain. Therefore, to evaluate the current prediction error, there exist multiple options as formulated in (4.4)-(4.6). Total error in magnitude is evaluated in (4.4), where (4.5) and (4.6) evaluates the prediction errors for α and β axes, respectively. The difference between the predicted and measured currents is named “current

prediction error" and abbreviated as "*CPE*". Superscripts *p* and *m* stand for predicted and measured respectively.

$$CPE_{TOTAL} = \left(I_{\alpha}^{p} - I_{\alpha}^{m}\right)^{2} + \left(I_{\beta}^{p} - I_{\beta}^{m}\right)^{2} \tag{4.4}$$

$$CPE_{\alpha} = \left(I_{\alpha}^{p} - I_{\alpha}^{m}\right)^{2} \tag{4.5}$$

$$CPE_{\beta} = \left(I_{\beta}^{p} - I_{\beta}^{m}\right)^{2} \tag{4.6}$$

As in the case of FIS and cost function waveforms, CPE waveforms too will be visualized through the DAC pins. The motor drive development platform TMDXIDDK379D is a 3.3 V system, it outputs a corresponding analog signal and over its DAC pins, for a digital input between 0 and 4096. Considering the high control frequency (40 kHz) thus the small intervals for current prediction, CPE values turn out to be small in magnitude. Therefore, while feeding them into the DAC stage, a multiplier of 6000 is utilized. Anyhow, similar to the discussions presented for the FIS waveform analysis, rather than the exact values of the observed quantities, the relative change in the waveforms due to the inflicting fault is meaningful. The lower excitation mode ($|\Psi_s|^{ref} = 0.3$) is adopted in the experimentation for the following analysis as the CPE response was found to be more responsive.

A typical CPE waveform is shown in Fig. 4.26 for the rated operating conditions described earlier. Since the sampling and the control rate are set to 40 kHz, the CPE waveform is also a rather high-frequency one. As in the case of analysis on the cost function, low-pass filtering the CPE waveforms would yield more intelligible results. Therefore, the low-pass filtered waveforms (PI type, with filter parameters $K_I = 0.95, K_P = 0.05$) are utilized hereon for the analysis on prediction error and ITSC fault's interaction.

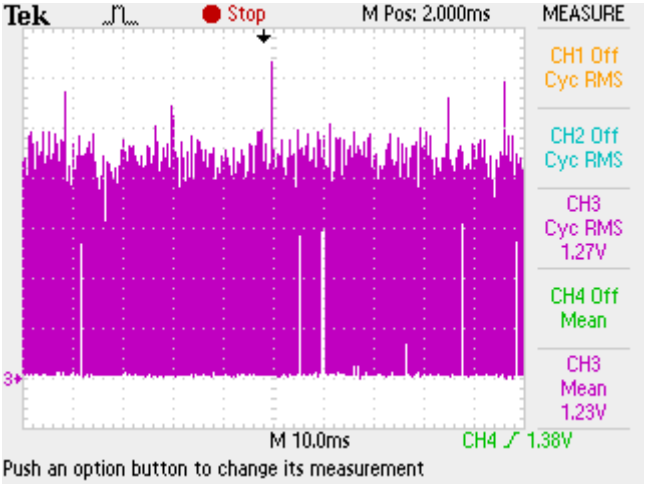

Figure 4.26. Current prediction error (CPE) waveform for the healthy motor under rated operating conditions, the unfiltered case.

The low-pass filtered CPE waveforms for the healthy case are displayed in Fig. 4.27a, b, and c, for CPE_{TOTAL} (as in (4.3)), CPE_{α} (as in (4.4)), and CPE_{β} (as in (4.5)) respectively. For the 2-turns ITSC fault case, Fig. 4.28 is created with the same notation. It is important to note again that the ITSC fault is created on "Phase A", which is coincident with the α-axis.

a)

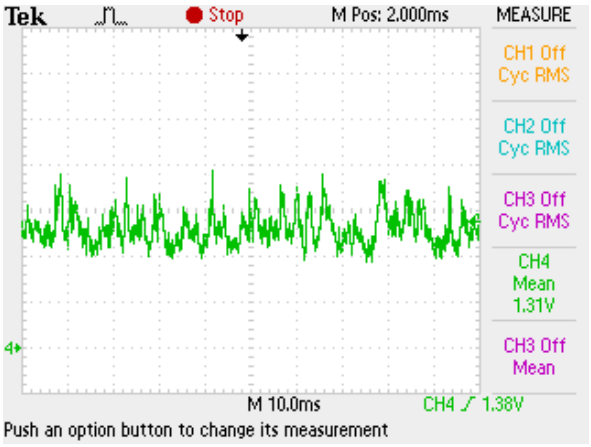

b)

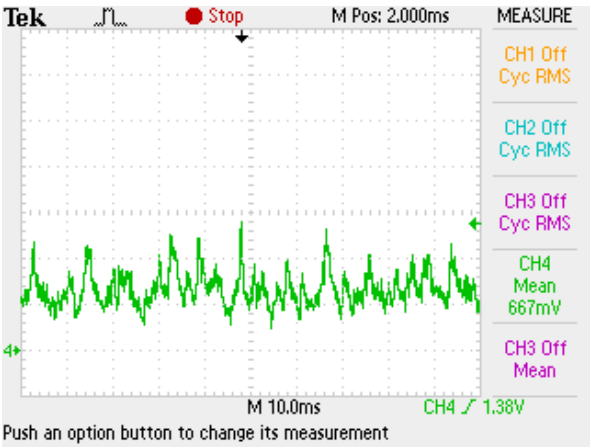

c)

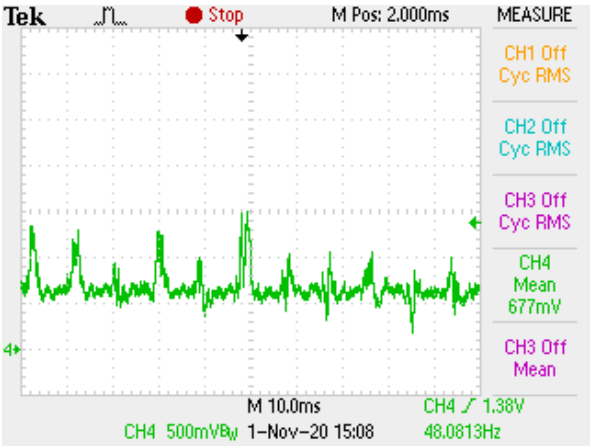

Figure 4.27. Low-pass filtered current prediction error (CPE) waveforms for the healthy motor under rated operating conditions, CPE_{TOTAL} (a), CPE_{α} (b), and CPE_{β} (c).

a)

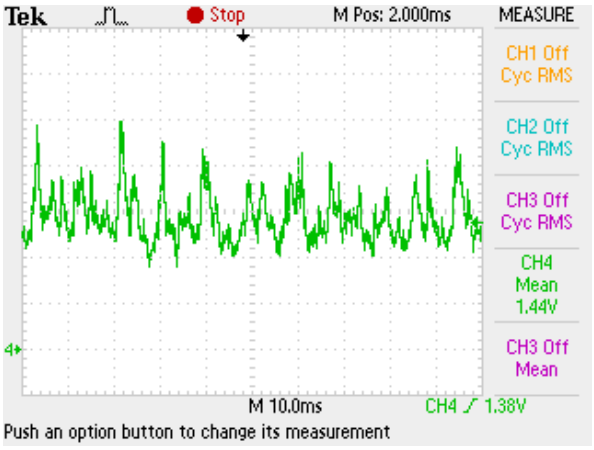

b)

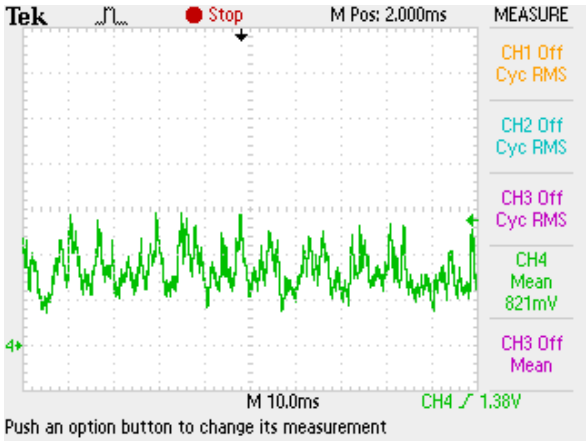

c)

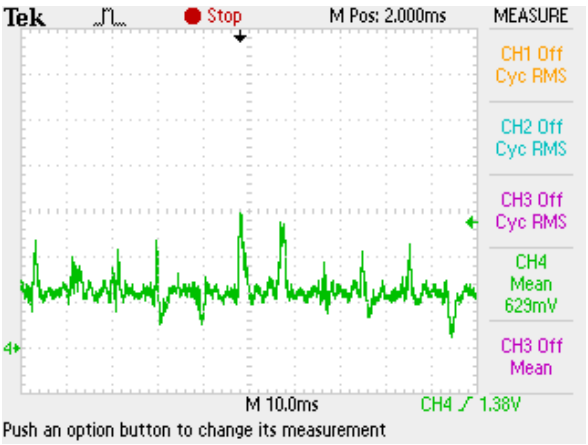

Figure 4.28. Low-pass filtered current prediction error (CPE) waveforms for the 2-turns ITSC fault, under rated operating conditions, CPE_{TOTAL} (a), CPE_{α} (b), and CPE_{β} (c).

From Fig. 4.27 and 4.28, it can be concluded that the current estimation error increases with the emergence of an ITSC fault. For the reader's convenience, the results from Fig. 4.27 and 4.28 are provided in Table 4.4.

Table 4.4 Current Prediction Error's Change due to the Inflicting Fault.

Item	*Healthy (V)*	*Faulty (V)*	*Change (%)*
α-Axis Current Prediction Error	0.67	0.82	22.4%
β-Axis Current Prediction Error	0.68	0.63	-7.4%
Total Current Prediction Error	1.31	1.44	9.9%

Looking at the mean values from the measurement column on the right-hand side, the mean value of the CPE_{TOTAL} can be observed to increase by nearly 10%, where the increase in CPE_{α} is roughly 22%. Since the fault current is on the α-axis hence can create no flux on the β-axis, the CPE_{β} waveform turns out to be almost insensitive to the fault. This feature can be utilized for the localization of a fault for a fault detection strategy based on the current prediction error. Consequently, the ITSC fault's effect on current prediction performance is observed to be as expected and this already known fault detection strategy is verified for the FCS-MPC driven IM.

4.6 Conclusion

Fault diagnosis of electric motors becomes more complicated for the case of inverter-driven, closed-loop controlled applications because the controller inherently tries to create a balanced set of current even under faulty conditions. In this chapter, a novel stator inter-turn short detection algorithm is developed, which detects and identifies the short-circuit fault based on the unexpected deviations in the predictive

controller's outputs. The proposed algorithm is intuitive, non-invasive, and works as a simple extension to the model predictive control routine. In the experimental verification, short-circuits of 2 and 3-turns are effectively detected and located (out of a total number of 104-turns in a phase) for the tested IM. The effectiveness of the proposed algorithm is documented with laborious experimental data: fault detection performance is verified over a large torque and speed range, even further in the dynamic operating condition. The fault detection time was below 2 seconds in the worst case, while the computational burden to the processor and the memory is negligible. The proposed algorithm is tested under several variations that include different flux level settings, sampling time, and λ value. A detailed benchmarking study is presented between the proposed algorithm and the existing ITSC-fault detection methods reported in the literature. The benchmarking results support the value and the effectiveness of the proposed fault detection technique. Further issues regarding the fault and the controller reaction, such as the change in the high-frequency impedance, the increase in the current prediction error, and the fault's influence on the cost function are also documented.

CHAPTER 5

CONCLUSIONS

The thesis is concluded with this chapter. A brief summary of the dissertation is presented first. Then, the contributions to the literature, which are made throughout this thesis work, are listed. Finally, future work related to the findings of this thesis is addressed.

5.1 A Brief Summary of the Thesis

The fundamental aspect of this study has been bridging the two major fields of power electronics research, namely; model predictive control and fault diagnosis. A comprehensive analysis of MPC with numerous references to the contemporary literature is presented first. Then the focus is narrowed down to the FCS-MPC case, as applied to the PTC of an IM. Covering both the theoretical fundamentals, computer simulations, and the experimental implementation aspects, the PTC of an IM is described in full detail. Laborious experiments have been conducted and documented, which suggest an effective motor drive operation, based on both steady-state performance figures and swift dynamic response.

Having presented a detailed MPC implementation, the next focus becomes the fault diagnosis of electrical machines, as the second main aspect of this study. After an overview of fault sources and types in electrical machines, the ITSC fault is analyzed. ITSCs are quite critical faults that need a very fast identification (in the order of a few seconds) or else they quickly develop further until the total destruction of the machine. They are the second most common fault type encountered in electrical machines after bearing faults, which often gradually arise due to

mechanical fatigue, hence not as severe in view of the urgency for fast fault identification.

Motivated from the lack of a simple simulation tool in the literature, to analyze the IM with an ITSC fault, a new model is developed based on the VBR model. The effectiveness of the developed simulation model is verified by comparison to the laboratory data obtained from a custom-modified IM, on which artificial ITSC faults can be created for experimental purposes.

Based on these two main topics, namely MPC and fault diagnosis, a novel method, which can detect ITSC faults of an IM effectively and efficiently, is developed and documented in Chapter 4. A review of the existing techniques from the literature that deals with ITSC detection for closed-loop controlled motor drive systems is presented first. Special emphasis is put on fault detection under closed-loop control because, in such systems, the controller inherently covers the fault traces, trying to create a balanced set of currents despite the inflicting fault. Utilizing this fact, a fault detection method is proposed which evaluates the unexpected unbalance in the controller outputs to identify a fault. The effectiveness of the developed fault detection technique is verified with detailed experiments. A benchmarking study is presented which compares the new method to the existing methods from the literature. It is shown that the developed method is a fast and effective one, capable of identifying ITSC faults with a significantly low severity ratio and shown to be effective over a wide operating range in the torque-speed plane. In order to provide a very brief analysis here, the advantages and the shortcomings of the proposed fault detection algorithm are listed as follows:

Advantages of the proposed method:

- Experimentally verified effectiveness: low severity ITSC fault detection (1.9%) over the entire range of operation, including the dynamic case
- Intuitive algorithm and ease of implementation as a natural add-on to the FCS-MPC routine, with no significant burden to the CPU (11.4 μs execution time).

- Sufficiently small fault detection time (below 2 seconds at worst).

Shortcomings of the proposed method:

- Fault/No-Fault decision is made on an empirically determined threshold value, which is also kept constant for different points on the torque-speed plane.
- No discrimination effort is made for other types of machine faults (i.e. bearing and rotor faults).

Further issues regarding the interaction between the predictive controller and the inflicting fault have also been analyzed. These include fault's influence on current prediction error, cost function, and the change in the high-frequency impedance.

5.2 Contributions Made to the Literature

Throughout this thesis work, 4 conference papers and a journal paper are published, as listed in Appendix A. The main contributions of these publications are summarized as follows:

- A method to reduce the number of prediction vectors is proposed in [12]. Furthermore, the influence of the zero vector selection (v_0 or v_7) is discussed with regard to switching loss.
- The experimental setup, which has been described in detail in Chapter 2, is proposed as a simple, fast, and low-cost way of FCS-MPC implementation in [13].
- An experimental weighting factor (λ) tuning procedure based on phase current THD is proposed in [14]. The simulation studies and the theoretical background prepared for [12]–[14] constitute the backbone of Chapter 2.
- The VBR-based IM model, which can simulate ITSC faults and discussed in Chapter 3 is first introduced in [15].

- The ITSC fault detection algorithm, which is based on the unexpected unbalance in the active vector allocation, is proposed in [16]. Chapter 4 is largely built upon [16], with several extra discussions included.

5.3 Future Prospects

Within the context of this thesis, there are several issues that can be regarded as future work. The most prominent one is the full description of how the inflicting fault influences the vector selection routine of the predictive controller. Although several observations and explanations are provided in Chapters 3 and 4, a full characterization is still absent.

The novel fault detection method is evaluated on a three-phase IM in order to show its effectiveness. However, the true value of any fault detection method would be appreciated with the utilization of a fault-tolerant machine and its driver, which also includes a post-fault operation strategy. Therefore, implementing the proposed method (or a variant of it) in a fault-tolerant (and/or multiphase) motor drive system and making the transition to the post-fault operation mode once the method signals an inflicting fault would be of much more practical value.

The new simulation model that can simulate the IM with an ITSC fault was presented in Chapter 3 and it was shown to be effective at depicting the faulty machine behavior. The basic deficiency of the model was identified as the neglection of the magnetic saturation of the core. An improved model would be more successful at simulating the faulty machine provided that the magnetic saturation is also included in the model.

In the developed fault diagnosis method, the essential signature utilized for fault detection is the unbalance that arises in the controller's outputs. Simple techniques are utilized to evaluate this unbalance, and the final fault/no-fault decision is given by comparison to a threshold, which is empirically determined from experiments.

Utilizing statistical techniques or advanced tools such as machine learning or artificial intelligence in the fault diagnosis effort would bear significant potential.

REFERENCES

[1] A. Pye, "$264bn [electric drives]," *Eng. Technol.*, vol. 10, no. 2, pp. 60–60, Mar. 2015, doi: 10.1049/et.2015.0206.

[2] A. M. EL-Refaie, "Toward a Sustainable More Electrified Future: The Role of Electrical Machines and Drives," *IEEE Electrif. Mag.*, vol. 7, no. 1, pp. 49–59, Mar. 2019, doi: 10.1109/MELE.2018.2889551.

[3] G. Abad, *Power Electronics and Electric Drives for Traction Applications*. Chichester, UK: John Wiley & Sons, Ltd, 2016. doi: 10.1002/9781118954454.

[4] I. Takahashi and T. Noguchi, "A New Quick-Response and High-Efficiency Control Strategy of an Induction Motor," *IEEE Trans. Ind. Appl.*, vol. IA-22, no. 5, pp. 820–827, Sep. 1986, doi: 10.1109/TIA.1986.4504799.

[5] M. Depenbrock, "Direct self-control (DSC) of inverter-fed induction machine," *IEEE Trans. Power Electron.*, vol. 3, no. 4, pp. 420–429, Oct. 1988, doi: 10.1109/63.17963.

[6] I. Boldea, "Control issues in adjustable speed drives," *IEEE Ind. Electron. Mag.*, vol. 2, no. 3, pp. 32–50, Sep. 2008, doi: 10.1109/MIE.2008.928605.

[7] G. S. Buja and M. P. Kazmierkowski, "Direct torque control of PWM inverter-fed AC motors - A survey," *IEEE Trans. Ind. Electron.*, vol. 51, no. 4, pp. 744–757, 2004, doi: 10.1109/TIE.2004.831717.

[8] J. Rodriguez and P. Cortes, *Predictive Control of Power Converters and Electrical Drives*. Chichester, UK: John Wiley & Sons, Ltd, 2012. doi: 10.1002/9781119941446.

[9] C. Liu, "Emerging Electric Machines and Drives — An Overview," *IEEE Trans. Energy Convers.*, vol. 33, no. 4, pp. 2270–2280, Dec. 2018, doi: 10.1109/TEC.2018.2852732.

[10] F. Betin, G. Capolino, D. Casadei, B. Kawkabani, E. Levi, and L. Parsa, “Trends in Electrical Machines Control,” *IEEE Ind. Electron. Mag.*, vol. 8, no. 2, pp. 43–55, 2014.

[11] M. Kazmierkowski, L. Franquelo, J. Rodriguez, M. Perez, and J. Leon, “High-Performance Motor Drives,” *IEEE Ind. Electron. Mag.*, vol. 5, no. 3, pp. 6–26, Sep. 2011, doi: 10.1109/MIE.2011.942173.

[12] I. Sahin and O. Keysan, “A new model predictive torque control strategy with reduced set of prediction vectors,” in *2018 IEEE 12th International Conference on Compatibility, Power Electronics and Power Engineering (CPE-POWERENG 2018)*, Apr. 2018, pp. 1–6. doi: 10.1109/CPE.2018.8372531.

[13] I. Sahin and O. Keysan, “A simplified discrete-time implementation of FCS-MPC applied to an IM drive,” in *2019 21st European Conference on Power Electronics and Applications (EPE ’19 ECCE Europe)*, Sep. 2019, p. P.1-P.8. doi: 10.23919/EPE.2019.8915204.

[14] I. Sahin, O. Keysan, and E. Monmasson, “Experimental tuning and design guidelines of a dynamically reconfigured weighting factor for the predictive torque control of an induction motor,” in *2020 22nd European Conference on Power Electronics and Applications (EPE’20 ECCE Europe)*, Sep. 2020, p. P.1-P.8. doi: 10.23919/EPE20ECCEEurope43536.2020.9215739.

[15] I. Sahin, G. H. Bayazit, and O. Keysan, “A Simulink Model for the Induction Machine with an Inter-Turn Short Circuit Fault,” in *2020 International Conference on Electrical Machines (ICEM)*, Aug. 2020, pp. 1273–1279. doi: 10.1109/ICEM49940.2020.9270853.

[16] I. Sahin and O. Keysan, “Model Predictive Controller Utilized as an Observer for Inter-Turn Short Circuit Detection in Induction Motors,” *IEEE Trans. Energy Convers.*, vol. 36, no. 2, pp. 1449–1458, Jun. 2021, doi: 10.1109/TEC.2020.3048071.

[17] M. Morari and J. H. Lee, “Model predictive control: past, present and future,” *Comput. Chem. Eng.*, vol. 23, no. 4–5, pp. 667–682, May 1999, doi: 10.1016/S0098-1354(98)00301-9.

[18] J. H. Lee, “Model predictive control: Review of the three decades of development,” *Int. J. Control. Autom. Syst.*, vol. 9, no. 3, pp. 415–424, Jun. 2011, doi: 10.1007/s12555-011-0300-6.

[19] P. Karamanakos and T. Geyer, “Guidelines for the Design of Finite Control Set Model Predictive Controllers,” *IEEE Trans. Power Electron.*, vol. 35, no. 7, pp. 7434–7450, Jul. 2020, doi: 10.1109/TPEL.2019.2954357.

[20] S. Vazquez *et al.*, “Model Predictive Control: A Review of Its Applications in Power Electronics,” *IEEE Ind. Electron. Mag.*, vol. 8, no. 1, pp. 16–31, Mar. 2014, doi: 10.1109/MIE.2013.2290138.

[21] S. Vazquez, J. Rodriguez, M. Rivera, L. G. Franquelo, and M. Norambuena, “Model Predictive Control for Power Converters and Drives: Advances and Trends,” *IEEE Trans. Ind. Electron.*, vol. 64, no. 2, pp. 935–947, Feb. 2017, doi: 10.1109/TIE.2016.2625238.

[22] G. Papafotiou, G. Demetriades, and V. Agelidis, “Technology Readiness Assessment of Model Predictive Control in Medium- and High-Voltage Power Electronics,” *IEEE Trans. Ind. Electron.*, vol. 0046, no. c, pp. 1–1, 2016, doi: 10.1109/TIE.2016.2521350.

[23] F. Wang, X. Mei, and S. Member, “Model Predictive Control for Electrical Drive Systems-An Overview,” *CES Trans. Electr. Mach. Syst.*, vol. 1, no. 3, pp. 219–230, 2017, doi: 10.23919/TEMS.2017.8086100.

[24] P. Karamanakos, T. Geyer, N. Oikonomou, F. D. Kieferndorf, and S. Manias, “Direct model predictive control: A review of strategies that achieve long prediction intervals for power electronics,” *IEEE Ind. Electron. Mag.*, vol. 8, no. 1, pp. 32–43, 2014, doi: 10.1109/MIE.2013.2290474.

[25] C. Bordons and C. Montero, “Basic Principles of MPC for Power Converters: Bridging the Gap between Theory and Practice,” *IEEE Ind. Electron. Mag.*, vol. 9, no. 3, pp. 31–43, 2015, doi: 10.1109/MIE.2014.2356600.

[26] S. Kouro, M. A. Perez, J. Rodriguez, A. M. Llor, and H. A. Young, “Model Predictive Control: MPC’s Role in the Evolution of Power Electronics,” *IEEE Ind. Electron. Mag.*, vol. 9, no. 4, pp. 8–21, 2015, doi: 10.1109/MIE.2015.2478920.

[27] J. Rodriguez *et al.*, “State of the Art of Finite Control Set Model Predictive Control in Power Electronics,” *IEEE Trans. Ind. Informatics*, vol. 9, no. 2, pp. 1003–1016, May 2013, doi: 10.1109/TII.2012.2221469.

[28] S. Kouro, P. Cortes, R. Vargas, U. Ammann, and J. Rodriguez, “Model Predictive Control—A Simple and Powerful Method to Control Power Converters,” *IEEE Trans. Ind. Electron.*, vol. 56, no. 6, pp. 1826–1838, Jun. 2009, doi: 10.1109/TIE.2008.2008349.

[29] F. B. Teresa Orłowska-Kowalska, José Rodríguez, *Advanced and Intelligent Control in Power Electronics and Drives*, Springer International Publishing, 2014. doi: 10.1007/978-3-319-03401-0.

[30] T. Geyer, *Model Predictive Control of High Power Converters and Industrial Drives*. John Wiley & Sons Ltd, 2017. ISBN: 978-1-119-01090-6

[31] A. Linder, R. Kanchan, R. Kennel, and P. Stolze, *Model-Based Predictive Control of Electric Drives*. Cuvillier Verlag Göttingen, 2010. ISBN: 3869553987

[32] V. Yaramasu and B. Wu, *Model Predictive Control of Wind Energy Conversion Systems*. Wiley-IEEE Press, 2016. ISBN: 978-1-118-98858-9

[33] T. Geyer, “Low complexity model predictive control in power electronics and power systems,” Swiss Federal Institute of Technology (ETH) Zurich, Ph.D. Thesis, 2005. [Online]. Available: http://www.tobiasgeyer.org/Geyer05_thesis.pdf

[34] P. Karamanakos, “Model Predictive Control Strategies for Power Electronics Converters and AC Drives,” National University of Athens, Ph.D. Thesis, 2015.

[35] M. Habibullah, “Simplified Finite-State Predictive Torque Control Strategies for Induction Motor Drives,” The University of Sydney, Ph.D. Thesis, 2016.

[36] F. Wang, “Model Predictive Torque Control for Electrical Drive Systems with and without an Encoder,” Technischen Universitat Munchen, Ph.D. Thesis, 2014.

[37] M. Habibullah, D. D.-C. Lu, D. Xiao, and M. F. Rahman, “A Simplified Finite-State Predictive Direct Torque Control for Induction Motor Drive,” *IEEE Trans. Ind. Electron.*, vol. 0046, no. c, pp. 1–1, 2016, doi: 10.1109/TIE.2016.2519327.

[38] Y. Yang, H. Wen, and D. Li, “A Fast and Fixed Switching Frequency Model Predictive Control with Delay Compensation for Three-Phase Inverters,” *IEEE Access*, vol. 5, pp. 17904–17913, 2017, doi: 10.1109/ACCESS.2017.2751619.

[39] B. Hu, L. Kang, J. Liu, J. Zeng, S. Wang, and Z. Zhang, “Model Predictive Direct Power Control With Fixed Switching Frequency and Computational Amount Reduction,” *IEEE J. Emerg. Sel. Top. Power Electron.*, vol. 7, no. 2, pp. 956–966, Jun. 2019, doi: 10.1109/JESTPE.2019.2894007.

[40] H. J. Yoo, T. T. Nguyen, and H. M. Kim, “MPC with constant switching frequency for inverter-based distributed generations in microgrid using gradient descent,” *Energies*, vol. 12, no. 6, pp. 7–9, 2019, doi: 10.3390/en12061156.

[41] F. Wang, Z. Zhang, X. Mei, J. Rodríguez, and R. Kennel, "Advanced Control Strategies of Induction Machine: Field Oriented Control, Direct Torque Control and Model Predictive Control," *Energies*, vol. 11, no. 1, p. 120, Jan. 2018, doi: 10.3390/en11010120.

[42] J. Rodriguez, R. M. Kennel, J. R. Espinoza, M. Trincado, C. A. Silva, and C. A. Rojas, "High-Performance Control Strategies for Electrical Drives: An Experimental Assessment," *IEEE Trans. Ind. Electron.*, vol. 59, no. 2, pp. 812–820, Feb. 2012, doi: 10.1109/TIE.2011.2158778.

[43] J. Holtz, "Advanced PWM and Predictive Control-An Overview," *IEEE Trans. Ind. Electron.*, vol. 63, no. 6, pp. 3837–3844, 2016, doi: 10.1109/TIE.2015.2504347.

[44] T. Geyer, G. Papafotiou, and M. Morari, "Model Predictive Direct Torque Control—Part I: Concept, Algorithm, and Analysis," *IEEE Trans. Ind. Electron.*, vol. 56, no. 6, pp. 1894–1905, Jun. 2009, doi: 10.1109/TIE.2008.2007030.

[45] G. Papafotiou, J. Kley, K. G. Papadopoulos, P. Bohren, and M. Morari, "Model predictive direct torque control - Part II: implementation and experimental evaluation," *IEEE Trans. Ind. Electron.*, vol. 56, no. 6, pp. 1906–1915, 2009, doi: 10.1109/TIE.2008.2007032.

[46] Y. Zhang, B. Xia, H. Yang, and J. Rodriguez, "Overview of model predictive control for induction motor drives," *Chinese J. Electr. Eng.*, vol. 2, no. 1, pp. 62–76, Jun. 2016, doi: 10.23919/CJEE.2016.7933116.

[47] J. Holtz, "Sensorless control of induction machines - With or without signal injection?," *IEEE Trans. Ind. Electron.*, vol. 53, no. 1, pp. 7–30, 2006, doi: 10.1109/TIE.2005.862324.

[48] J. Holtz, "The representation of AC machine dynamics by complex signal flow graphs," *IEEE Trans. Ind. Electron.*, vol. 42, no. 3, pp. 263–271, Jun. 1995, doi: 10.1109/41.382137.

[49] J. Holtz, “The induction motor-a dynamic system,” in *Proceedings of IECON’94 - 20th Annual Conference of IEEE Industrial Electronics*, 1994, vol. 1, pp. P1–P6. doi: 10.1109/IECON.1994.397757.

[50] J. Holtz, “Dynamic representation of AC drive systems by complex signal flow graphs,” *IEEE Int. Symp. Ind. Electron.*, pp. 1–6, 1994, doi: 10.1109/isie.1994.333121.

[51] J. Holtz, “Sensorless control of induction motor drives,” *Proc. IEEE*, vol. 90, no. 8, pp. 1359–1394, Aug. 2002, doi: 10.1109/JPROC.2002.800726.

[52] P. L. Jansen and R. D. Lorenz, “A Physically Insightful Approach to the Design and Accuracy Assessment of Flux Observers for Field Oriented Induction Machine Drives,” *IEEE Trans. Ind. Appl.*, vol. 30, no. 1, pp. 101–110, 1993, doi: 10.1109/28.273627.

[53] J. Hu and B. Wu, “New integration algorithms for estimating motor flux over a wide speed range,” *IEEE Trans. Power Electron.*, vol. 13, no. 5, pp. 969–977, 1998, doi: 10.1109/63.712323.

[54] N. R. N. Idris and A. H. M. Yatim, “An improved stator flux estimation in steady-state operation for direct torque control of induction machines,” *IEEE Trans. Ind. Appl.*, vol. 38, no. 1, pp. 110–116, 2002, doi: 10.1109/28.980364.

[55] M. Hinkkanen, “Analysis and design of full-order flux observers for sensorless induction motors,” *IEEE Trans. Ind. Electron.*, vol. 51, no. 5, pp. 1033–1040, 2004, doi: 10.1109/TIE.2004.834964.

[56] M. Barut, S. Bogosyan, and M. Gokasan, “Speed-sensorless estimation for induction motors using extended Kalman filters,” *IEEE Trans. Ind. Electron.*, vol. 54, no. 1, pp. 272–280, 2007, doi: 10.1109/TIE.2006.885123.

[57] N. T. West and R. D. Lorenz, “Digital implementation of stator and rotor flux-linkage observers and a stator-current observer for deadbeat direct torque control of induction machines,” *IEEE Trans. Ind. Appl.*, vol. 45, no. 2, pp. 729–736, 2009, doi: 10.1109/TIA.2009.2013567.

[58] D. Stojic, M. Milinkovic, S. Veinovic, and I. Klasnic, “Improved Stator Flux Estimator for Speed Sensorless Induction Motor Drives,” *IEEE Trans. Power Electron.*, vol. 30, no. 4, pp. 2363–2371, Apr. 2015, doi: 10.1109/TPEL.2014.2328617.

[59] K. Wang, R. D. Lorenz, and N. A. Baloch, “Improvement of Back-EMF Self-Sensing for Induction Machines When Using Deadbeat-Direct Torque and Flux Control,” *IEEE Trans. Ind. Appl.*, vol. 53, no. 5, pp. 4569–4578, 2017, doi: 10.1109/TIA.2017.2711964.

[60] P. Cortes, J. Rodriguez, C. Silva, and A. Flores, “Delay Compensation in Model Predictive Current Control of a Three-Phase Inverter,” *IEEE Trans. Ind. Electron.*, vol. 59, no. 2, pp. 1323–1325, Feb. 2012, doi: 10.1109/TIE.2011.2157284.

[61] İ. Şahin, “Simulation Files, Codes, and Supplementary Material for the PhD Thesis,” *GitHub Repository*, 2021. [Online]. Available: https://github.com/ilkersahin78/phd_thesis_repo (accessed 09.09.2021)

[62] Y. Cho, Y. Bak, and K. Lee, “Torque-Ripple Reduction and Fast Torque Response Strategy for Predictive Torque Control of Induction Motors,” *IEEE Trans. Power Electron.*, vol. 33, no. 3, pp. 2458–2470, Mar. 2018, doi: 10.1109/TPEL.2017.2699187.

[63] S. A. Davari, “Predictive Direct Angle Control of Induction Motor,” *IEEE Trans. Ind. Electron.*, vol. 63, no. 8, pp. 5276–5284, 2016, doi: 10.1109/TIE.2016.2551198.

[64] A. A. Ahmed, B. K. Koh, and Y. Il Lee, “A Comparison of Finite Control Set and Continuous Control Set Model Predictive Control Schemes for Speed Control of Induction Motors,” *IEEE Trans. Ind. Informatics*, vol. 14, no. 4, pp. 1334–1346, 2018, doi: 10.1109/TII.2017.2758393.

[65] C. A. Rojas, J. Rodriguez, F. Villarroel, J. R. Espinoza, C. A. Silva, and M. Trincado, “Predictive Torque and Flux Control Without Weighting Factors,” *IEEE Trans. Ind. Electron.*, vol. 60, no. 2, pp. 681–690, Feb. 2013, doi: 10.1109/TIE.2012.2206344.

[66] H. Miranda, P. Cortes, J. I. Yuz, and J. Rodriguez, “Predictive Torque Control of Induction Machines Based on State-Space Models,” *IEEE Trans. Ind. Electron.*, vol. 56, no. 6, pp. 1916–1924, 2009, doi: 10.1109/TIE.2009.2014904.

[67] M. Amiri, J. Milimonfared, and D. A. Khaburi, “Predictive Torque Control Implementation for Induction Motors Based on Discrete Space Vector Modulation,” *IEEE Trans. Ind. Electron.*, vol. 65, no. 9, pp. 6881–6889, 2018, doi: 10.1109/TIE.2018.2795589.

[68] F. Wang, Z. Zhang, A. Davari, J. Rodríguez, and R. Kennel, “An experimental assessment of finite-state Predictive Torque Control for electrical drives by considering different online-optimization methods,” *Control Eng. Pract.*, vol. 31, pp. 1–8, 2014, doi: 10.1016/j.conengprac.2014.06.004.

[69] N. Al-Sheakh Ameen, A. A. Naassani, and R. M. Kennel, “Design of a digital system dedicated for electrical drive applications,” *EPE J. (European Power Electron. Drives Journal)*, vol. 20, no. 4, pp. 37–44, 2010, doi: 10.1080/09398368.2010.11463776.

[70] P. Karamanakos, P. Stolze, R. M. Kennel, S. Manias, and H. du Toit Mouton, “Variable Switching Point Predictive Torque Control of Induction Machines,” *IEEE J. Emerg. Sel. Top. Power Electron.*, vol. 2, no. 2, pp. 285–295, Jun. 2014, doi: 10.1109/JESTPE.2013.2296794.

[71] Fengxiang Wang, Zhe Chen, P. Stolze, J.-F. Stumper, J. Rodriguez, and R. Kennel, "Encoderless Finite-State Predictive Torque Control for Induction Machine With a Compensated MRAS," *IEEE Trans. Ind. Informatics*, vol. 10, no. 2, pp. 1097–1106, May 2014, doi: 10.1109/TII.2013.2287395.

[72] Texas Instruments, "DesignDRIVE Development Kit IDDK v2.2.1 - User's Guide," 2015. [Online]. Available: https://www.ti.com/lit/ug/sprui44/sprui44.pdf (accessed 09.09.2021)

[73] Texas Instruments, "TMS320F2837xD Dual-Core Delfino ™ Microcontrollers," Product Datasheet, 2018. [Online]. Available: http://www.ti.com/lit/ds/symlink/tms320f28377d.pdf (accessed 09.09.2021)

[74] Texas Instruments, "TMS320F2837xD Dual-Core Delfino Microcontrollers ™ Technical Reference Manual," 2008. [Online]. Available: https://www.ti.com/lit/ug/spruhm8h/spruhm8h.pdf (accessed 09.09.2021)

[75] Texas Instruments, "DesignDRIVE Development Kit IDDK v2.2.1 - Hardware Reference Guide," 2015. [Online]. Available: https://www.ti.com/cn/lit/ug/sprui43/sprui43.pdf

[76] R. Ramamoorthy, B. Larimore, and M. Bhardwaj, "Sensored Field Oriented Control of 3-Phase Permanent Magnet Synchronous Motors using F2837x," Application Note, 2016. [Online]. Available: www.ti.com/lit/an/sprabz0/sprabz0.pdf

[77] "IEEE Power Engineering Society," "IEEE Standard Test Procedure for Polyphase Induction Motors and Generators," 1991.

[78] Texas Instruments, "controlSUITE," 2019. [Online]. http://www.ti.com/tool/CONTROLSUITE (accessed Sep. 09, 2019).

[79] Texas Instruments, "C2000WARE," 2019. [Online]. http://www.ti.com/tool/C2000WARE (accessed Sep. 09, 2019).

[80] C. D. Townsend, G. Mirzaeva, and G. C. Goodwin, “Deadtime Compensation for Model Predictive Control of Power Inverters,” *IEEE Trans. Power Electron.*, vol. 32, no. 9, pp. 7325–7337, Sep. 2017, doi: 10.1109/TPEL.2016.2630712.

[81] C. Xia, T. Liu, T. Shi, and Z. Song, “A simplified finite-control-set model-predictive control for power converters,” *IEEE Trans. Ind. Informatics*, vol. 10, no. 2, pp. 991–1002, 2014, doi: 10.1109/TII.2013.2284558.

[82] T. Geyer, “Computationally efficient model predictive direct torque control,” *IEEE Trans. Power Electron.*, vol. 26, no. 10, pp. 2804–2816, 2011, doi: 10.1109/TPEL.2011.2121921.

[83] M. Preindl and S. Bolognani, “Model Predictive Direct Torque Control With Finite Control Set for PMSM Drive Systems, Part 1: Maximum Torque Per Ampere Operation,” *IEEE Trans. Ind. Informatics*, vol. 9, no. 4, pp. 1912–1921, Nov. 2013, doi: 10.1109/TII.2012.2227265.

[84] W. Xie *et al.*, “Finite-control-set model predictive torque control with a deadbeat solution for PMSM drives,” *IEEE Trans. Ind. Electron.*, vol. 62, no. 9, pp. 5402–5410, 2015, doi: 10.1109/TIE.2015.2410767.

[85] P. Cortes *et al.*, “Guidelines for weighting factors design in Model Predictive Control of power converters and drives,” in *2009 IEEE International Conference on Industrial Technology*, Feb. 2009, pp. 1–7. doi: 10.1109/ICIT.2009.4939742.

[86] T. Geyer, “Algebraic Tuning Guidelines for Model Predictive Torque and Flux Control,” *IEEE Trans. Ind. Appl.*, vol. 54, no. 5, pp. 4464–4475, 2018, doi: 10.1109/TIA.2018.2835375.

[87] L. M. A. Caseiro, A. M. S. Mendes, and S. M. A. Cruz, “Dynamically Weighted Optimal Switching Vector Model Predictive Control of Power Converters,” *IEEE Trans. Ind. Electron.*, vol. 66, no. 2, pp. 1235–1245, 2019, doi: 10.1109/TIE.2018.2829689.

[88] S. A. Davari, D. A. Khaburi, and R. Kennel, “An improved FCS-MPC algorithm for an induction motor with an imposed optimized weighting factor,” *IEEE Trans. Power Electron.*, vol. 27, no. 3, pp. 1540–1551, 2012, doi: 10.1109/TPEL.2011.2162343.

[89] O. Machado, F. J. Rodriguez, E. J. Bueno, and P. Martin, “A Neural Network-Based Dynamic Cost Function for the Implementation of a Predictive Current Controller,” *IEEE Trans. Ind. Informatics*, vol. 13, no. 6, pp. 2946–2955, 2017, doi: 10.1109/TII.2017.2691461.

[90] G. B. Kliman, W. J. Premerlani, B. Yazici, R. A. Koegl, and J. Mazereeuw, “Sensorless, online motor diagnostics,” *IEEE Comput. Appl. Power*, vol. 10, no. 2, pp. 39–43, Apr. 1997, doi: 10.1109/67.582451.

[91] S. Nandi, H. A. Toliyat, and X. Li, “Condition Monitoring and Fault Diagnosis of Electrical Motors—A Review,” *IEEE Trans. Energy Convers.*, vol. 20, no. 4, pp. 719–729, Dec. 2005, doi: 10.1109/TEC.2005.847955.

[92] P. J. Tavner, “Review of condition monitoring of rotating electrical machines,” *IET Electr. Power Appl.*, vol. 2, no. 4, p. 215, 2008, doi: 10.1049/iet-epa:20070280.

[93] M. Riera-Guasp, J. A. Antonino-Daviu, and G. A. Capolino, “Advances in electrical machine, power electronic, and drive condition monitoring and fault detection: State of the art,” *IEEE Trans. Ind. Electron.*, vol. 62, no. 3, pp. 1746–1759, 2015, doi: 10.1109/TIE.2014.2375853.

[94] J.-C. Trigeassou, *Electrical Machines Diagnosis*. Hoboken, NJ, USA: John Wiley & Sons, Inc, 2011. doi: 10.1002/9781118601662.

[95] H. A. Toliyat, S. Nandi, S. Choi, and H. Meshgin-kelk, *Electric Machines - Modeling Condition Monitoring and Fault Diagnosis*. 2013. ISBN: 9781138073975

[96] S. A. S. Al Kazzaz and G. K. Singh, “Experimental investigations on induction machine condition monitoring and fault diagnosis using digital signal processing techniques,” *Electr. Power Syst. Res.*, vol. 65, no. 3, pp. 197–221, 2003, doi: 10.1016/S0378-7796(02)00227-4.

[97] P. Zhang, Y. Du, T. G. Habetler, and B. Lu, “A survey of condition monitoring and protection methods for medium-voltage induction motors,” *IEEE Trans. Ind. Appl.*, vol. 47, no. 1, pp. 34–46, 2011, doi: 10.1109/TIA.2010.2090839.

[98] A. Bellini, F. Filippetti, C. Tassoni, and G. A. Capolino, “Advances in diagnostic techniques for induction machines,” *IEEE Trans. Ind. Electron.*, vol. 55, no. 12, pp. 4109–4126, 2008, doi: 10.1109/TIE.2008.2007527.

[99] Z. Ullah and J. Hur, “A comprehensive review of winding short circuit fault and irreversible demagnetization fault detection in PM type machines,” *Energies*, vol. 11, no. 12, 2018, doi: 10.3390/en11123309.

[100] Y. Chen, S. Liang, W. Li, H. Liang, and C. Wang, “Faults and Diagnosis Methods of Permanent Magnet Synchronous Motors: A Review,” *Appl. Sci.*, vol. 9, no. 10, p. 2116, May 2019, doi: 10.3390/app9102116.

[101] A. H. Bonnett and C. Yung, “Increased efficiency versus increased reliability,” *IEEE Ind. Appl. Mag.*, vol. 14, no. 1, pp. 29–36, 2008, doi: 10.1109/MIA.2007.909802.

[102] IEEE, *IEEE Recommended Practice for the Design of Reliable Industrial and Commercial Power Systems*, vol. 2007. 2007.

[103] A. H. Bonnett and G. C. Soukup, “Cause and Analysis of Stator and Rotor Failures in Three-Phase Squirrel-Cage Induction Motors,” *IEEE Trans. Ind. Appl.*, vol. 28, no. 4, pp. 921–937, 1992, doi: 10.1109/28.148460.

[104] S. Bin Lee *et al.*, “Condition Monitoring of Industrial Electric Machines: State of the Art and Future Challenges,” *IEEE Ind. Electron. Mag.*, vol. 14, no. 4, pp. 158–167, Dec. 2020, doi: 10.1109/MIE.2020.3016138.

[105] S. Grubic, J. M. Aller, B. Lu, and T. G. Habetler, “A survey on testing and monitoring methods for stator insulation systems of low-voltage induction machines focusing on turn insulation problems,” *IEEE Trans. Ind. Electron.*, vol. 55, no. 12, pp. 4127–4136, 2008, doi: 10.1109/TIE.2008.2004665.

[106] M. Fenger, S. R. Campbell, and J. Pedersen, “Motor winding problems: Caused by inverter drives,” *IEEE Ind. Appl. Mag.*, vol. 9, no. 4, pp. 22–31, Jul. 2003, doi: 10.1109/MIA.2003.1206913.

[107] D. Macdonald and W. Gray, “PWM drive related bearing failures,” *IEEE Ind. Appl. Mag.*, vol. 5, no. 4, pp. 41–47, 1999, doi: 10.1109/2943.771365.

[108] Weijun Yin, “Failure mechanism of winding insulations in inverter-fed motors,” *IEEE Electr. Insul. Mag.*, vol. 13, no. 6, pp. 18–23, Nov. 1997, doi: 10.1109/57.637150.

[109] A. K. Morya *et al.*, “Wide bandgap devices in AC electric drives: Opportunities and challenges,” *IEEE Trans. Transp. Electrif.*, vol. 5, no. 1, pp. 3–20, 2019, doi: 10.1109/TTE.2019.2892807.

[110] A. Morya and H. A. Toliyat, “Insulation design for Wide Bandgap (WBG) device based voltage source converter fed motors,” *2017 IEEE 5th Work. Wide Bandgap Power Devices Appl. WiPDA 2017*, vol. 2017-Decem, pp. 74–79, 2017, doi: 10.1109/WiPDA.2017.8170525.

[111] J. A. Haylock, B. C. Mecrow, A. G. Jack, and D. J. Atkinson, “Operation of fault tolerant machines with winding failures,” *IEEE Trans. Energy Convers.*, vol. 14, no. 4, pp. 1490–1495, 1999, doi: 10.1109/60.815095.

[112] A. J. Mitcham, G. Antonopoulos, and J. J. A. Cullen, “Implications of shorted turn faults in bar wound PM machines,” *IEE Proc. - Electr. Power Appl.*, vol. 151, no. 6, p. 651, 2004, doi: 10.1049/ip-epa:20040686.

[113] B. Wang, J. Wang, A. Griffo, and L. Huang, “A Turn Fault Mitigation Strategy Based on Current Injection Technique for a Triple Three-Phase PMA SynRM,” *IEEE Trans. Ind. Electron.*, vol. 67, no. 4, pp. 2511–2522, Apr. 2020, doi: 10.1109/TIE.2019.2908595.

[114] P. Arumugam, T. Hamiti, and C. Gerada, “Turn–turn short circuit fault management in permanent magnet machines,” *IET Electr. Power Appl.*, vol. 9, no. 9, pp. 634–641, Nov. 2015, doi: 10.1049/iet-epa.2015.0020.

[115] F. Duan, “Induction Motor Parameters Estimation and Faults Diagnosis using Optimisation Algorithms,” The University of Adelaide, 2014.

[116] W. T. Thomson and M. Fenger, “Current signature analysis to detect induction motor faults,” *IEEE Ind. Appl. Mag.*, vol. 7, no. 4, pp. 26–34, 2001, doi: 10.1109/2943.930988.

[117] G. S. Yadava, B. Singh, and A. Siddique, “A Review of Stator Fault Monitoring Techniques of Induction Motors,” *IEEE Trans. Energy Convers.*, vol. 20, no. 1, pp. 106–114, 2005, doi: 10.1109/TEC.2004.837304.

[118] A. Gandhi, T. Corrigan, and L. Parsa, “Recent advances in modeling and online detection of stator interturn faults in electrical motors,” *IEEE Trans. Ind. Electron.*, vol. 58, no. 5, pp. 1564–1575, 2011, doi: 10.1109/TIE.2010.2089937.

[119] A. Berzoy, A. A. S. Mohamed, and O. Mohammed, “Complex-Vector Model of Interturn Failure in Induction Machines for Fault Detection and Identification,” *IEEE Trans. Ind. Appl.*, vol. 53, no. 3, pp. 2667–2678, 2017, doi: 10.1109/TIA.2016.2632068.

[120] R. M. Tallam, T. G. Habetler, and R. G. Harley, “Transient model for induction machines with stator winding turn faults,” *IEEE Trans. Ind. Appl.*, vol. 38, no. 3, pp. 632–637, 2002, doi: 10.1109/TIA.2002.1003411.

[121] X. Chang, V. Cocquempot, and C. Christophe, “A model of asynchronous machines for stator fault detection and isolation,” *IEEE Trans. Ind. Electron.*, vol. 50, no. 3, pp. 578–584, 2003, doi: 10.1109/TIE.2003.812471.

[122] D. C. Patel and M. C. Chandorkar, “Modeling and analysis of stator interturn fault location effects on induction machines,” *IEEE Trans. Ind. Electron.*, vol. 61, no. 9, pp. 4552–4564, 2014, doi: 10.1109/TIE.2013.2288191.

[123] M. Arkan, D. Kostic-Perovic, and P. J. Unsworth, “Modelling and simulation of induction motors with inter-turn faults for diagnostics,” *Electr. Power Syst. Res.*, vol. 75, no. 1, pp. 57–66, 2005, doi: 10.1016/j.epsr.2004.08.015.

[124] C. W. Ho, D. R. Bertenshaw, A. C. Smith, T. Chan, and M. Sasic, “Three-dimensional finite element analysis of large electrical machine stator core faults,” *IET Electr. Power Appl.*, vol. 8, no. 2, pp. 60–67, 2014, doi: 10.1049/iet-epa.2013.0065.

[125] A. Berzoy, A. A. S. Mohamed, and O. Mohammed, “Impact of Inter-Turn Short-Circuit Location on Induction Machines Parameters Through FE Computations,” *IEEE Trans. Magn.*, vol. 53, no. 6, 2017, doi: 10.1109/TMAG.2017.2665639.

[126] K. Prasob, N. P. Kumar, and T. B. Isha, “Inter-turn short circuit fault analysis of PWM inverter fed three-phase induction motor using Finite Element Method,” *Proc. IEEE Int. Conf. Circuit, Power Comput. Technol. ICCPCT 2017*, 2017, doi: 10.1109/ICCPCT.2017.8074384.

[127] C. Rojas, M. G. Melero, M. F. Cabanas, J. M. Cano, G. A. Orcajo, and F. Pedrayes, “Finite element model for the study of inter-turn short circuits in induction motors,” *2007 IEEE Int. Symp. Diagnostics Electr. Mach. Power Electron. Drives, SDEMPED*, pp. 415–419, 2007, doi: 10.1109/DEMPED.2007.4393130.

[128] M. A. Cash, T. G. Habetler, and G. B. Kliman, “Insulation failure prediction in ac machines using line-neutral voltages,” *IEEE Trans. Ind. Appl.*, vol. 34, no. 6, pp. 1234–1239, 1998, doi: 10.1109/28.738983.

[129] F. Duan and R. Zivanovic, “A model for induction motor with stator faults,” *Power Eng. Conf.*, pp. 1–5, 2012, [Online]. Available: http://ieeexplore.ieee.org/xpls/abs_all.jsp?arnumber=6360198

[130] F. Therrien, M. Chapariha, and J. Jatskevich, “Constant-Parameter Voltage-Behind-Reactance Induction Machine Model Including Main Flux Saturation,” *IEEE Trans. Energy Convers.*, vol. 30, no. 1, pp. 90–102, Mar. 2015, doi: 10.1109/TEC.2014.2342258.

[131] N. Amiri, S. Ebrahimi, J. Jatskevich, and H. W. Dommel, “Saturable and Decoupled Constant-Parameter VBR Model for Six-Phase Synchronous Machines in State-Variable Simulation Programs,” *IEEE Trans. Energy Convers.*, vol. 34, no. 4, pp. 1868–1880, 2019, doi: 10.1109/TEC.2019.2907268.

[132] N. Amiri, S. Ebrahimi, Y. Huang, J. Jatskevich, and S. D. Pekarek, “Constant-Parameter Voltage-Behind-Reactance Modeling of Five-Phase Synchronous Machines with Air-Gap Flux Harmonics,” *IEEE Trans. Energy Convers.*, vol. 35, no. 1, pp. 119–129, 2020, doi: 10.1109/TEC.2019.2942828.

[133] L. Wang, J. Jatskevich, and S. D. Pekarek, “Modeling of induction machines using a voltage-behind-reactance formulation,” *IEEE Trans. Energy Convers.*, vol. 23, no. 2, pp. 382–392, 2008, doi: 10.1109/TEC.2008.918601.

[134] A. S. Abdel-Khalik, S. Ahmed, A. A. Elserougi, and A. M. Massoud, “A voltage-behind-reactance model of five-phase induction machines considering the effect of magnetic saturation,” *IEEE Trans. Energy Convers.*, vol. 28, no. 3, pp. 576–592, 2013, doi: 10.1109/TEC.2013.2258467.

[135] L. Wang and J. Jatskevich, “A Voltage-Behind-Reactance Synchronous Machine Model for the EMTP-Type Solution,” *IEEE Trans. Power Syst.*, vol. 21, no. 4, pp. 1539–1549, Nov. 2006, doi: 10.1109/TPWRS.2006.883670.

[136] P. Tricoli, “Induction machine model,” *MATLAB Central File Exchange*, 2015. https://www.mathworks.com/matlabcentral/fileexchange/53174-induction-machine-model (accessed Sep. 09, 2021).

[137] İ. Şahin, G. H. Bayazıt, and O. Keysan, “A Simulink Model for the Induction Machine with an Inter-Turn Short Circuit Fault,” *GitHub Repository*, 2020. https://github.com/ilkersahin78/A-Simulink-Model-for-the-Induction-Machine-with-an-Inter-Turn-Short-Circuit-Fault

[138] M. El Hachemi Benbouzid, “A review of induction motors signature analysis as a medium for faults detection,” *IEEE Trans. Ind. Electron.*, vol. 47, no. 5, pp. 984–993, 2000, doi: 10.1109/41.873206.

[139] L. Maraaba, Z. Al-Hamouz, and M. Abido, “An efficient stator inter-turn fault diagnosis tool for induction motors,” *Energies*, vol. 11, no. 3, 2018, doi: 10.3390/en11030653.

[140] J. S. Hsu and S. Member, “Monitoring of Defects in Induction Motors Through Air-Gap Torque Observation,” *IEEE Trans. Ind. Appl.*, vol. 31, no. 5, pp. 1016–1021, 1995.

[141] S. F. Legowski, S. Member, A. H. M. S. Ula, and A. M. Trzynadlowsh, “Instantaneous Power as a Medium for the Signature Analysis of Induction Motors,” *IEEE Trans. Ind. Appl.*, vol. 32, no. 4, pp. 904–909, 1996.

[142] M. Drif and A. J. M. Cardoso, “Stator fault diagnostics in squirrel cage three-phase induction motor drives using the instantaneous active and reactive power signature analyses,” *IEEE Trans. Ind. Informatics*, vol. 10, no. 2, pp. 1348–1360, 2014, doi: 10.1109/TII.2014.2307013.

[143] A. Bellini, F. Filippetti, G. Franceschini, and C. Tassoni, “Closed-Loop Control Impact on the Diagnosis of Induction Motors Faults,” *IEEE Trans. Ind. Appl.*, vol. 36, no. 5, pp. 1318–1329, 2000.

[144] M. Zafarani, E. Bostanci, Y. Qi, T. Goktas, and B. Akin, “Interturn short-circuit faults in permanent magnet synchronous machines: An extended review and comprehensive analysis,” *IEEE J. Emerg. Sel. Top. Power Electron.*, vol. 6, no. 4, pp. 2173–2191, 2018, doi: 10.1109/JESTPE.2018.2811538.

[145] H. H. Eldeeb, A. Berzoy, and O. Mohammed, “Stator Fault Detection on DTC-Driven IM via Magnetic Signatures Aided by 2-D FEA Co-Simulation,” *IEEE Trans. Magn.*, vol. 55, no. 6, pp. 1–5, Jun. 2019, doi: 10.1109/TMAG.2019.2892707.

[146] S. Cheng, P. Zhang, and T. G. Habetler, “An impedance identification approach to sensitive detection and location of stator turn-to-turn faults in a closed-loop multiple-motor drive,” *IEEE Trans. Ind. Electron.*, vol. 58, no. 5, pp. 1545–1554, 2011, doi: 10.1109/TIE.2010.2064276.

[147] M. Wolkiewicz, G. Tarchała, T. Orłowska-Kowalska, and C. T. Kowalski, “Online stator interturn short circuits monitoring in the DFOC induction-motor drive,” *IEEE Trans. Ind. Electron.*, vol. 63, no. 4, pp. 2517–2528, Apr. 2016, doi: 10.1109/TIE.2016.2520902.

[148] T. M. Wolbank, K. A. Loparo, and R. Wohrnschimmel, “Inverter statistics for online detection of stator asymmetries in inverter-fed induction motors,” *IEEE Trans. Ind. Appl.*, vol. 39, no. 4, pp. 1102–1108, Jul. 2003, doi: 10.1109/TIA.2003.814576.

[149] B. Sen and J. Wang, “Stator Interturn Fault Detection in Permanent-Magnet Machines Using PWM Ripple Current Measurement,” *IEEE Trans. Ind. Electron.*, vol. 63, no. 5, pp. 3148–3157, 2016, doi: 10.1109/TIE.2016.2515560.

[150] K. H. Kim, “Simple online fault detecting scheme for short-circuited turn in a PMSM through current harmonic monitoring,” *IEEE Trans. Ind. Electron.*, vol. 58, no. 6, pp. 2565–2568, 2011, doi: 10.1109/TIE.2010.2060463.

[151] J. A. Rosero, L. Romeral, J. A. Ortega, and E. Rosero, “Short-circuit detection by means of empirical mode decomposition and Wigner-Ville distribution for PMSM running under dynamic condition,” *IEEE Trans. Ind. Electron.*, vol. 56, no. 11, pp. 4534–4547, 2009, doi: 10.1109/TIE.2008.2011580.

[152] F. Briz, M. W. Degner, A. Zamarrón, and J. M. Guerrero, “Online Stator Winding Fault Diagnosis in Inverter-Fed AC Machines using High-Frequency Signal Injection,” *IEEE Trans. Ind. Appl.*, vol. 39, no. 4, pp. 1109–1117, 2003, doi: 10.1109/TIA.2003.813746.

[153] S. M. A. Cruz and A. J. M. Cardoso, “Diagnosis of stator inter-turn short circuits in DTC induction motor drives,” *IEEE Trans. Ind. Appl.*, vol. 40, no. 5, pp. 1349–1360, 2004, doi: 10.1109/TIA.2004.834012.

[154] J. Hang, J. Zhang, M. Xia, S. Ding, and W. Hua, “Interturn Fault Diagnosis for Model-Predictive-Controlled-PMSM Based on Cost Function and Wavelet Transform,” *IEEE Trans. Power Electron.*, vol. 35, no. 6, pp. 6405–6418, 2020, doi: 10.1109/TPEL.2019.2953269.

[155] Z. Ullah and J. Hur, “Analysis of Inter-Turn-Short Fault in an FSCW IPM Type Brushless Motor Considering Effect of Control Drive,” *IEEE Trans. Ind. Appl.*, vol. 56, no. 2, pp. 1356–1367, 2020, doi: 10.1109/TIA.2019.2961878.

[156] B. Wang, J. Hu, G. Wang, and W. Hua, “A Novel Stator Turn Fault Detection Technique by Using Equivalent High Frequency Impedance,” *IEEE Access*, vol. 8, pp. 130540–130550, 2020, doi: 10.1109/ACCESS.2020.3009109.

[157] Z. Ullah, S.-T. Lee, and J. Hur, “A Torque Angle-Based Fault Detection and Identification Technique for IPMSM,” *IEEE Trans. Ind. Appl.*, vol. 56, no. 1, pp. 170–182, Jan. 2020, doi: 10.1109/TIA.2019.2947401.

[158] M. A. Mazzoletti, G. R. Bossio, C. H. De Angelo, and D. R. Espinoza-Trejo, "A Model-Based Strategy for Interturn Short-Circuit Fault Diagnosis in PMSM," *IEEE Trans. Ind. Electron.*, vol. 64, no. 9, pp. 7218–7228, Sep. 2017, doi: 10.1109/TIE.2017.2688973.

[159] X. Mao and L. Hao, "Stator winding diagnostic systems and methods," US Patent, 2014/0191697 A1, 2014

[160] A. Berzoy, O. A. Mohammed, and J. Restrepo, "Analysis of the Impact of Stator Interturn Short-Circuit Faults on Induction Machines Driven by Direct Torque Control," *IEEE Trans. Energy Convers.*, vol. 33, no. 3, pp. 1463–1474, 2018, doi: 10.1109/TEC.2018.2827170.

[161] S. Cheng, P. Zhang, and T. G. Habetler, "An Impedance Identification Approach to Sensitive Detection and Location of Stator Turn-to-Turn Faults in a Closed-Loop Multiple-Motor Drive," *IEEE Trans. Ind. Electron.*, vol. 58, no. 5, pp. 1545–1554, May 2011, doi: 10.1109/TIE.2010.2064276.

APPENDICES

A. Publications Originated from the Thesis

Below is a list of publications originated from this thesis:

Ref.	*Title*	*Published at*
[12]	"A new model predictive torque control strategy with reduced set of prediction vectors"	CPE-Powereng 2018, Doha, Qatar
[13]	"A simplified discrete-time implementation of FCS-MPC applied to an IM drive"	EPE-ECCE Europe 2019, Genova, Italy
[14]	"Experimental tuning and design guidelines of a dynamically reconfigured weighting factor for the predictive torque control of an induction motor"	EPE-ECCE Europe 2020, Lyon, France
[15]	"A Simulink model for the induction machine with an inter-turn short circuit fault"	ICEM 2020, Gothenburg, Sweden
[16]	"Model predictive controller utilized as an observer for inter-turn short circuit detection in induction motors"	IEEE Transactions on Energy Conversion, 2021

Additionally, two national (Turkish) patents have been applied as following:

Title	*Application Number*
"Alternatif akım motorların model kestirimci denetiminde tahmin vektörlerini azaltan yöntem"	2018/14498
"Elektrik makinaları için bir arıza erken teşhis yöntemi"	2019/19743

B. Supplementary Material for the Thesis

All of the related material for this thesis are made available as open-source in the Git-Hub repository [61], the web address of which is also provided below:

https://github.com/ilkersahin78/phd_thesis_repo

The following items are included:

- Matlab/Simulink simulation file that contains the motor drive simulation of Chapter 2
- The developed simulation model for the IM with an ITSC fault, as described in Chapter 3
- The switching vectors' record that is summarized in Table 4.2 of Chapter 4
- The source codes for the implemented drive, that have been programmed on TMDXISSK379D, including both the MPC drive and the fault detection algorithm.

CURRICULUM VITAE

PERSONAL INFORMATION

Surname, Name: Şahin, İlker
Nationality: Turkish (TC)
Date and Place of Birth: 1986, Karabük
Marital Status: Married
email: ilkersahin78@gmail.com

EDUCATION

Degree	Institution	Year of Graduation
MS	METU Electrical and Electronics Eng.	2014
BS	METU Electrical and Electronics Eng.	2010
High School	75. Yıl Karabük Anadolu Lisesi	2004

WORK EXPERIENCE

Year	Place	Enrollment
2020-Present	ASELSAN	Design Lead
2011-2020	METU Dept. of Electrical Eng.	Research Assistant
2010	Mercados EMI	Engineer

FOREIGN LANGUAGES

Turkish (Native)

English (Advanced)

PUBLICATIONS

1. İ. Sahin and O. Keysan, “Model Predictive Controller Utilized as an Observer for Inter-Turn Short Circuit Detection in Induction Motors,” IEEE Trans. Energy Convers., vol. 8969, no. c, pp. 1–1, 2020.

2. İ. Sahin, O. Keysan, and E. Monmasson, “Experimental tuning and design guidelines of a dynamically reconfigured weighting factor for the predictive torque control of an induction motor,” in 2020 22nd European Conference on Power Electronics and Applications (EPE’20 ECCE Europe), 2020, p. P.1-P.8.

3. İ. Sahin, G. H. Bayazit, and O. Keysan, “A Simulink Model for the Induction Machine with an Inter-Turn Short Circuit Fault,” in 2020 International Conference on Electrical Machines (ICEM), 2020, pp. 1273–1279.

4. İ. Şahin and O. Keysan, “A simplified discrete-time implementation of FCS-MPC applied to an im drive,” 2019 21st Eur. Conf. Power Electron. Appl. EPE 2019 ECCE Eur., pp. 1–8, Sep. 2019.

5. İ. Sahin and O. Keysan, “A new model predictive torque control strategy with reduced set of prediction vectors,” in 2018 IEEE 12th International Conference on Compatibility, Power Electronics and Power Engineering (CPE-POWERENG 2018), 2018, pp. 1–6.

6. Erencan Duymaz, Siamak Pourkeivannour, Doğa Ceylan, İlker Şahin and Ozan Keysan, “Design of a Power Plant Emulator for the Dynamic Frequency Stability Studies”, ICEM 2018, Alexandroupoli, Greece, 2018.

7. İ. Şahin, A. M. Hava, “Design and Implementation of a 800W Step Down Converter with Optimized F-L-N Parameters,” IEEE-ISIE 2014 Conference, June 2014, İstanbul, Turkey, pp. 2089-2094.

8. İ. Şahin, A. M. Hava, “Volume and Efficiency Optimization of a Step-down DC/DC Converter Based on F-L-N Parameters,” ELECO 2013, 8th International Conference on Electrical and Electronics Engineering, 28-30 November 2013, Bursa, Turkey

9. İ. Şahin, A. M. Hava, (in Turkish), “Güç Elektroniği Dönüştürücülerinde Faz Kaydırmalı Modül Paralelleme Yöntemi” Otomasyon Dergisi, sayı 238, Nisan 2012, sayfa 408-416.

10. İ. Şahin, A.M. Hava, (in Turkish), “Geleneksel Tek Katlı DC-DC Dönüştürücü Yapısı ile Faz Kaydırmalı Modül Paralelleme Yönteminin Genel Karşılaştırılması,” ELECO 2012, Elektrik-Elektronik-Bilgisayar Mühendisliği Sempozyumu, 2-5 Aralık 2012, Bursa, sayfa 470-474.